Reviewed Preprint
v1 • September 10, 2024
Not revised

Reviewed Preprint
v2 • March 6, 2026
Revised by authors

For correspondence:
yohan.davit@imft.fr

Competing interests: No competing interests declared

Funding: See page 42

Reviewing editor: Babak Momeni, Boston College, United States

Should I stay or should I go? Spatiotemporal dynamics of bacterial biofilms in confined flows

Massinissa Benbelkacem[1,2], Gabriel Ramos[1,2], Fatima El Garah[2], Yara Abidine[1], Christine Roques[2], Yohan Davit[1]

[1]Institut de Mécanique des Fluides (IMFT), Université de Toulouse, CNRS, INPT, UPS, Toulouse, France • [2]Laboratoire de Génie Chimique (LGC), Université de Toulouse, CNRS, INPT, UPS, Toulouse, France

eLife Assessment

This **important** study combines microfluidic experiments with mathematical modeling to elucidate the reciprocal interplay between flow dynamics and biofilm growth and detachment. Using Pseudomonas aeruginosa as a model organism, the authors identify several key regimes and stages of biofilm development. Overall, the comparison between experimental observations of biofilm behavior under varying flow conditions and corresponding theoretical predictions forms a **compelling** understanding of the processes involved in biofilm dynamics. The results will be of interest to researchers studying biofilms and their technological and biological applications.

https://doi.org/10.7554/eLife.98292.2.sa2

Abstract

Most bacteria live in sessile biofilms that colonize the confined channels, pores and crevices of natural and engineered structures. In these environments, flow delivers nutrients necessary for growth while simultaneously generating mechanical stresses that cause detachment from surfaces. Bacteria, in turn, colonize flow passages, increasing hydraulic resistance and modifying transport properties. Although the importance of advective transport and hydrodynamic forces on bacterial populations is well established, the complex feedback mechanisms governing biofilm development in confined geometries remain poorly understood. Here, we study how couplings between flow and bacterial development control the spatiotemporal dynamics of *Pseudomonas aeruginosa* in microchannel flows. We demonstrate that nutrient availability primarily drives the longitudinal distribution of biomass along the channel, while competition between growth and flow-induced detachment controls the transverse distribution and temporal dynamics. We find that biofilms undergo successive cycles of sloughing and regrowth, causing persistent fluctuations in the hydraulic resistance and biomass that prevent the system from ever reaching a true steady state. Our results indicate that these self-sustained fluctuations are a signature effect in confined flows, originating from a pressure build-up as growing bacteria obstruct flow paths. We further show that the sloughing dynamics can be described as a jump stochastic process with gamma-distributed interevent times, analogous to other bursting events such as earthquakes or avalanches. This stochastic framework provides a quantitative approach to characterizing the inherent randomness and apparent irreproducibility of biofilm experiments, opening new avenues for predictive modeling of biofilms in confined systems.

Introduction

Fluid flow and transport phenomena control many aspects of the life of bacteria (Krsmanovic et al., 2021), from the motility of cells (Busscher and van der Mei, 2006; Rodesney et al., 2017) to the morphology of biofilm colonies (Wang et al., 2022), and even ecological interactions within

populations (Battin et al., 2016). As a testimony to the importance of flow, bacteria have evolved specific strategies adapted to their mechanical environment and the rheology of fluids around them (Dufrêne and Persat, 2020). Bacteria have also evolved mechanisms to detect gradients of nutrients or toxic substances and adapt their movement accordingly (Sampedro et al., 2014). Recent studies further suggest that bacteria have mechanosensing and rheosensing capabilities (Dufrêne and Persat, 2020). *Pseudomonas aeruginosa* has been found to regulate the fro operon in response to flow-modulated H2O2 concentrations (Sanfilippo et al., 2019; G.C. Padron, 2023). Shear also modifies the intracellular levels of cyclic-di-GMP in cells of *P. aeruginosa* attached to a surface, initiating a sessile phenotype (Rodesney et al., 2017).

Even in dense surface-associated colonies known as biofilms (Costerton et al., 1995; Flemming et al., 2016), where cells are partially isolated from the fluid by a matrix of self-produced extracellular polymeric substances (Flemming and Wingender, 2010), flow still plays a fundamental role (Thomen et al., 2017; Rusconi et al., 2011). The flow of a viscous fluid around the matrix generates forces that can induce detachment or remodel the biofilm (Besemer et al., 2007; Stoodley et al., 1998) – the matrix essentially behaves as a viscoelastic material (Peterson et al., 2015) and thus can flow in response to stress (Gloag et al., 2020). Furthermore, key solutes, such as oxygen or nutrients, are transported in the fluid before they can diffuse in the biofilm and be consumed. This can lead to complex couplings between advective transport by flow, diffusion in the fluid and in the biofilm, and uptake by the cells (Taherzadeh et al., 2012; Picioreanu et al., 2000). It has also been recently demonstrated that flow can generate spatial heterogeneities in the activation of quorum-sensing within populations, as a result of autoinducers being washed away by flow in zones at high Péclet number (Kim et al., 2016; Emge et al., 2016; Mukherjee and Bassler, 2019).

The vast majority of bacteria live in biofilms that colonize confined geometries (Conrad and Poling-Skutvik, 2018). In such systems, biofilms can occupy a large portion of the available space and thus severely restrict flow. This tends to generate a two-way coupling between biofilm growth and transport phenomena whereby flow and transport mediate the development of the biofilm, but in return the development of the biofilm also modifies flow and transport (Rittmann, 1993; Taylor and Jaffé, 1990a; Taylor et al., 1990; Taylor and Jaffé, 1990b, c; Vandevivere and Baveye, 1992b,a; Stewart and Fogler, 2001; Telgmann et al., 2004; Drescher et al., 2013). In porous media, for instance, Kurz et al. (2022) showed that a *Bacillus subtilis* biofilm can clog a large part of the pore space, leaving only few preferential flow channels where a competition between shear-induced detachment and growth drives intermittency and spontaneous pressure fluctuations. Such bioclogging is an important component of systems as diverse as bioreactors in the food industry (Verran, 2002), biofilters for wastewater processing (Aslam et al., 2018), pipe flow for water distribution (Cowle et al., 2014), heat exchangers (García and Trueba, 2020), catheters used in medicine (Bixler and Bhushan, 2012), soil bioremediation (Singh et al., 2006), enhanced oil recovery (Sen, 2008; Kryachko, 2018) or biobarriers (Lennox and Ashe, 2009). Understanding the fundamentals of biofilm growth and feedback mechanisms with flow is therefore a crucial step towards developing better approaches in health and engineering.

Here, we investigate the role of couplings between nutrient transport, growth and detachment on biofilm development in microchannel flows. To do so, we developed a microfluidic setup generating a constant flow rate in a microchannel where a *P. aeruginosa* PAO1 GFP biofilm develops. This microfluidic system is further combined with timelapse microscopy, cellular microbiology and mathematical modeling to study the interactions between biofilm and flow, in particular the dynamics and spatiotemporal fluctuations.

Results

Our experimental approach is summarized in Fig 1. We inoculated cells of *P. aeruginosa* PAO1 GFP in a microchannel and then continuously flowed a culture medium at constant flow rate to observe biofilm development, which is contained in the central part of the channel through the use of UVC irradiation (see Material and Methods). In what follows, we first study the effects of

nutrient limitation on the spatial distribution of biofilm. This allows us to identify flow regimes where nutrients are in excess and biofilm development is primarily driven by the interactions with flow. We then focus on regimes without limitations to detail the role of flow-induced detachment on the temporal dynamics.

Nutrient limitation controls the longitudinal distribution of the biofilm

To assess the impact of nutrient limitation, we performed experiments at flow rates over several orders of magnitude ($Q = 2 \times 10^{-2}$, 2×10^{-1}, 2×10^{0}, and $2 \times 10^{+1} \mu L/min$) and therefore different total fluxes of nutrients. Fig 2a shows the time-integrated distributions of the GFP fluorescence in the longitudinal direction for the different flow rates. We found that the active biomass expressing GFP is relatively uniform for flow rates between 0.2 and $20 \mu L/min$ – the sharp decrease on the left-hand side at the outlet corresponds to the effect of the UVCs. For 0.02 $\mu L/min$, however, we observed a maximum value of the fluorescence intensity at the inlet on the right-hand side and a distinct decrease when moving towards the outlet.

Considering that the growth of *P. aeruginosa* PAO1 GFP is aerobic here – *P. aeruginosa* is a facultative anaerobe and can perform denitrification in specific anaerobic environments by anoxic respiration using nitrogenated compounds as final electron acceptors (Arat et al., 2015) but this produces less energy (Bartberger et al., 2002) – we hypothesized that this heterogeneity in biofilm development along the channel stems from a limitation of solute species required for growth, either oxygen or one of the nutrients in the growth medium. For the largest flow rates, advective transport through the channel should be fast compared to consumption, so that even bacteria at the outlet receive sufficient levels of nutrients and oxygen for biofilm development. For the lowest flow rate, however, one of the components introduced at the inlet is rapidly consumed by bacteria and becomes limiting, so that growth decreases with the distance from the inlet.

To better understand this limitation, we repeated experiments at 0.02 $\mu L/min$ either with BHI diluted 5 times or by supplementing 1×BHI with additional glucose. Results in Fig 2a with the glucose supplementation show a similar longitudinal distribution of biofilm compared to assays without glucose, thus suggesting that this carbon source is not the limiting nutrient – it was confirmed by mass spectrometry that only a small fraction of the glucose was consumed. Results with the five times diluted BHI, however, show a much narrower window of biofilm growth, therefore suggesting that one of the components in the BHI is becoming limiting. Although oxygen probably features gradients within the biofilm (Folsom et al., 2010) and in the longitudinal direction, the inlet concentration of oxygen is identical for the two cases 1×BHI and 0.2×BHI, therefore indicating that oxygen is not the primary component limiting growth. Another factor that may further alleviate oxygen limitations is that PDMS is highly permeable to oxygen, so that there are in fact two sources of oxygen in our system: dissolved oxygen in the culture medium and oxygen coming from/through the PDMS.

To explore these different hypotheses and quantify the characteristic times of reactive transport, we simulated the development of the biofilm inside the channels, taking into account the couplings between biofilm growth and nutrient transport. The limiting nutrient is treated as a solute being transported by advection/diffusion and consumed by bacteria. We considered that mass transport is much faster than bacterial growth and division, so that the problem is quasi-steady for solute transport (Picioreanu et al., 2000). The limiting nutrient was thus modeled as

$$\underbrace{Pe\partial_x C^\star}_{\text{Advection}} = \underbrace{\partial_{xx} C^\star}_{\text{Diffusion}} - \underbrace{Da\phi \frac{C^\star}{C^\star + K^\star}}_{\text{Nutrient uptake}}, \quad (1)$$

where $C^\star = \frac{C}{C_0}$ is the non-dimensionalized solute concentration with C $[kg \times m^{-3}]$ the concentration and C_0 $[kg \times m^{-3}]$ the inlet concentration, x is the longitudinal coordinate system normalized with the length of the channel $L = 10\ mm$, K $[kg \times m^{-3}]$ the half-saturation constant and Φ is the fraction of the cross section occupied by the biofilm ($\Phi = {}^{\Omega}\text{biofilm}/\Omega\text{total}$ with Ω_{biofilm} the area of the cross section occupied by the biofilm and Ω_{total} the total area of the cross section). $P\,e$ is the Péclet

Figure 1. Schematic representation of the system and of the two main experimental steps.

The first step is *P. aeruginosa* PAO1 GFP culture and inoculation in the microchannel (PDMS on glass, 100 *μm* × 100 *μm* cross-section) using a pressure pump. The bacterial suspension is then left for 3 hours without flow to allow cells to adhere. The second step consists in flowing the culture medium at constant flow rate through the microchannel, while recording pressure fluctuations and imaging biofilm development via optical microscopy. UVC radiation is used during the second step of the experiment to constrain the biofilm in a specific part of the channel.

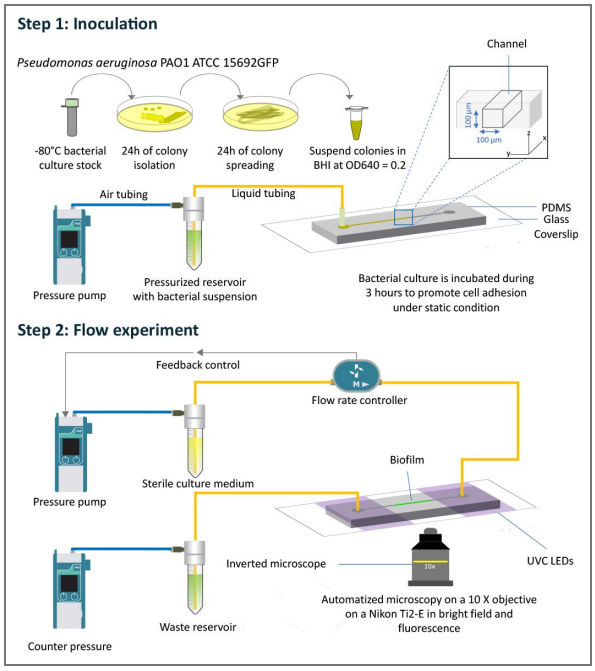

Figure 2. Impact of nutrient limitation on the longitudinal distribution of biofilm.

(a): Time-integrated fluorescence intensity over 72h for the flow rates Q = 0.02 *μL/min*, 0.2 *μL/min*, 2 *μL/min* and 20 *μL/min* with 1× concentrated brain heart infusion (BHI) culture medium, along with Q = 0.02 *μL/min* with either 0.2× BHI or 1× BHI supplemented with 8 *g/L* glucose. Nutrient limitation is observed only for Q = 0.02 *μL/min* and is strongly dependent upon the concentration of BHI components. (b): Simulations for Q = 0.02 *μL/min* for two values of Φ_{max} and the corresponding Damköhler numbers. The Damköhler numbers for the case with 0.2× BHI were simply obtained by multiplying those for the case 1× BHI by a factor 5. Each experimental curve in (a) and (b) is averaged over 3 replicates. In the model, we considered that the fluorescence signal is proportional to the product of biomass and nutrient concentration. We then integrated this signal in time and normalized it with the maximum value as $\overline{F}(x) = \int_0^t \phi(x,\tau)C(x,\tau)d\tau \Big/ \int_0^t \phi(x=0,\tau)C(x=0,\tau)d\tau$.

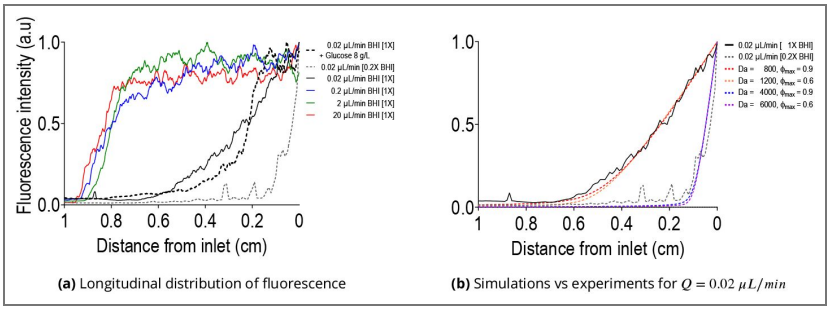

(a) Longitudinal distribution of fluorescence

(b) Simulations vs experiments for $Q = 0.02\ \mu L/min$

number defined as the ratio of longitudinal diffusion to advection times, $Pe = \frac{VL}{D}$ with V [$m \times s^{-1}$] the average velocity in the empty channel and D an estimate diffusion coefficient of the solute – as a reference, for a generic value $D = 10^{-9} m^2 \times s^{-1}$, we have $Pe \simeq 330$ for 0.02 $\mu L/min$. Da is the Damköhler number defined as the ratio of diffusive to reactive times, $Da = \frac{\alpha L^2}{C_0 D}$ with α [$kg \times m^{-3} \times s^{-1}$] the uptake rate. The term Φ in the nutrient uptake indicates that consumption is proportional to the volume fraction of biofilm. Reference values are presented in Table 1.

For the biomass growth, we used a model capturing the coupled effects of growth and flow-induced removal,

$$\partial_t \phi = \underbrace{\frac{C^\star (1+K^\star)}{C^\star + K^\star}\phi}_{\text{Growth}} - \underbrace{\mathcal{M} f(\phi)\phi}_{\text{Removal}}, \qquad (2)$$

where $f(\phi) = \sqrt{\frac{\sigma}{\sigma_0}} = (1-\phi)^{-1}$ with $\sigma = \frac{A}{4}\frac{\mu Q}{h^3}(1-\phi)^{-2}$ the average tangential stress at the biofilm solid interface (see SI) and $\sigma_0 = \frac{A}{4}\frac{\mu Q}{h^3}$ the shear stress in the empty square cross-section channel (see Table 1 for reference values). Here A is a scalar parameter characterizing the geometry of the cross-section colonization – $A = \frac{12}{1-\sum_{n,\text{odd}}^{\infty} \frac{1}{n^5}\frac{192}{\pi^5}\tanh\left(n\frac{\pi}{2}\right)} \simeq \frac{12}{1-0.917\times 0.63}$ (Bruus, 2008) for a uniform layer of biofilm with a square cross-section for flow passage. We also have $\mathcal{M} = \frac{\chi X}{Y\alpha(1+K^\star)}\sqrt{\sigma_0}$, which is the dimensionless number characterizing the competition between growth and detachment, containing the rate of biomass detachment $\chi \left[s^{-1} \times N^{-\frac{1}{2}} \times m\right]$.

A number of works express the detachment rate as proportional to the square root of the fluid shear stress at the biofilm fluid interface (Coyte et al., 2017). Here this could be written as $f(\phi) = \sqrt{\frac{\tau_{\text{shear}}}{\sigma_0}} = (1-\phi)^{-3/4}$ with τ_{shear} the shear stress at the biofilm fluid interface. Such approaches, however, were initially developed for flows in reactor systems, where shear stress is dominant (Duddu et al., 2009; Rittman, 1982), and neglect the contribution of the pressure stress to detachment:Characklis et al. (1982), for instance, measured the rate of biofilm loss considering different shear stresses generated by rotating the inner annulus of reactor at different speeds and found a linear relationship between biofilm loss rate and rotational speed. Upon clogging the microchannel, we expect the pressure difference to generate a significant force on the biofilm and to play an important role on detachment. We therefore consider a contribution of detachment scaling as $(1-\Phi)^{-1}$.

Assuming that $\mathcal{M} \in]0, 1]$, the model for the biomass can be written in a simpler form as

$$\partial_t \phi = \phi\left[\frac{C^\star(1+K^\star)}{C^\star+K^\star} - \frac{1-\phi_{\max}}{1-\phi}\right], \qquad (3)$$

with $\Phi_{\max}$ the maximum volume fraction of biofilm, defined as $\mathcal{M} = 1 - \Phi_{\max}$, $\Phi_{\max} \in [0, 1[$ and $\Phi \in [0, \Phi_{\max}]$. The only non-trivial steady state,

$$\phi_{\text{equ}} = 1 - (1-\phi_{\max})\frac{C^\star + K^\star}{C^\star(1+K^\star)}, \qquad (4)$$

reflects an equilibrium between the amount of biomass created and the amount of biomass detached. The trivial steady state $\Phi_{\text{equ}} = 0$ is stable when detachment exceeds growth, i.e. when $C^\star$ is lower than $\frac{K^\star(1-\phi_{\max})}{K^\star+\phi_{\max}}$. In assuming that $\mathcal{M} \in]0, 1]$ and eliminating cases where $\mathcal{M}, > 1$ we have not considered situations of systematic detachment $\Phi_{\text{equ}} = 0$ for any value of the concentration, since this is not a situation that we encountered experimentally.

Fig 2b compares results of the model with those of the experimental fluorescence for the flow rate 0.02 $\mu L/min$ and $K^\star = 0.1$. To roughly assess the sensitivity of our simulation to uncertainties in the value of $\Phi_{\max}$, we further considered two extreme values, $\Phi_{\max} \simeq 0.6$ and $\Phi_{\max} \simeq 0.9$. The model shows good agreement with experiments for $Da_{\text{BHI}\times 1} \simeq 1200$ in the case $\Phi_{\max} \simeq 0.6$ and $Da_{\text{BHI}\times 1} \simeq 800$ in the case $\Phi_{\max} \simeq 0.9$. The corresponding characteristic reaction time for nutrient uptake, $\tau_{\text{reac}} = {}^{C}{}_0/\alpha$, ranges from $\simeq 83s$ to $\simeq 125s$. We further obtain an excellent correspondence between the model and the experimental data for the 5 times dilution of the BHI without any fitting, simply by multiplying the Damköhler number by a factor 5 – recall that, by definition, $Da = {}^{\alpha L2}/_{C_0 D}$ with C_0 the inlet concentration so that dividing C_0 by 5 implies multiplying the Damköhler

Table 1. Summary of various quantities in the experiments and models.

σ_0 is the shear stress in empty channel. $\frac{R_{max}}{R_0}$ is the corresponding shear rate. D is an estimate diffusion coefficient for the limiting component. Pe is the Péclet number. Φ_{max} is the maximum volumic fraction of biofilm. Da is the Damköhler number. τ_{reac} is the reaction time. Pe/Da is the ratio of Péclet to Damköhler numbers. To calculate dimensionless numbers, we used $D = 10^{-9}\ m^2 s^{-1}$ and $L = 10\ mm$.

Conditions	Variables						
	$\sigma_0\ (Pa)$	$\dot{\gamma}_0\ (s^{-1})$	Pe	ϕ_{max}	Da	$\tau_{reac}\ (s)$	Pe/Da
$Q = 0.02\ \mu L/min$ [BHI] = 0.2X	2.4×10^{-3}	2.4×10^{0}	3.3×10^{2}	0.6	6.0×10^{3}	17	8.3×10^{-2}
				0.9	4.0×10^{3}	25	5.5×10^{-2}
$Q = 0.02\ \mu L/min$ [BHI] = 1X				0.6	1.2×10^{3}	83	4.2×10^{-1}
				0.9	8.0×10^{2}	125	2.8×10^{-1}
$Q = 0.2\ \mu L/min$ [BHI] = 1X	2.4×10^{-2}	2.4×10^{1}	3.3×10^{3}	0.989	10^3	~ 100	3.3×10^{0}
$Q = 2\ \mu L/min$ [BHI] = 1X	2.4×10^{-1}	2.4×10^{2}	3.3×10^{4}	0.968			3.3×10^{1}
$Q = 20\ \mu L/min$ [BHI] = 1X	2.4×10^{0}	2.4×10^{3}	3.3×10^{5}	0.907			3.3×10^{2}
$Q = 200\ \mu L/min$ [BHI] = 1X	2.4×10^{1}	2.4×10^{4}	3.3×10^{6}	0.786			3.3×10^{3}

Table 2. Values obtained from direct fitting of the experimental data

Q	a	b	μ	σ
$0.2\ \mu L/min$	3.71	7.28×10^{-2}	−5.19	1.28
$2\ \mu L/min$	3.51	8.90×10^{-2}	−5.07	1.29
$20\ \mu L/min$	1.53	2.50×10^{-1}	−3.90	1.34

number by a factor 5. The fact that the behavior of the system with 5 times dilution of the BHI can be obtained without any fitting confirms that the primary limitation is indeed one of the components of the BHI, not oxygen.

With these estimations of characteristic times for uptake, we can also evaluate whether any form of transverse limitation of nutrient is expected by comparing times for transverse diffusion and uptake. The characteristic time for diffusion in the transverse direction is $\tau_{\text{diff}} = \frac{h^2}{D} \simeq 50\ \mu m$ with h a characteristic length for the distance between the flow channel and the wall. Considering again a diffusion coefficient in the biofilm $D = 10^{-9} m^2/s$ for the limiting nutrient, we have $\tau^h_{\text{diff}} \simeq 2.5\ s$. Diffusive transport across the channel is therefore significantly faster than uptake, implying that there is no form of limitation in the transverse direction.

The complete picture for nutrient transport is therefore as follows. In the longitudinal direction, the distribution of biomass is driven by a competition between advective transport and nutrient uptake. This can be quantified using the ratio of the Péclet and Damköhler numbers, $^{P\,e}/Da$. When advective transport is faster than uptake, $^{P\,e}/Da > 1$, the distribution of the biofilm is uniform. On the other hand, when $^{P\,e}/Da < 1$, uptake is faster than advective transport so that growth is nutrient limited. Table 1 summarizes the values of $^{P\,e}/Da$ for the different cases and shows that the regime $^{P\,e}/Da < 1$ is reached only for the flow rate 0.02 $\mu L/min$. In the transverse direction, there is no nutrient limitation and the amount of biomass is determined by an equilibrium between growth and flow-induced detachment. The details of this mechanisms, and its impact on the temporal dynamics, is the core of the following sections.

Hydrodynamic stresses affect all stages of development

We focus on flow rates Q = 0.2, 2 and 20 $\mu L/min$ where nutrient limitation is negligible, allowing us to decouple the effects of molecular transport from hydrodynamic stresses. We describe the temporal dynamics through two classes of measurements: the time evolution of the pressure and timelapse microscopy imaging. The evolution of the pressure was monitored in the inlet reservoir, while imposing a constant flow rate. From this measurement, we reconstructed the evolution in time of the hydraulic resistance of the zone of interest in the channel, R (t), where biofilm developed (see Material and Methods). This allowed us to determine the dynamics of the ratio $\frac{R}{R_0}$, with the hydraulic resistance of the empty channel, as shown in Fig 3 (see also supplementary information figures S5, S8 and S11) and to analyze the different stages in the colonization of the channel.

Combined with a model for the distribution of biofilm in the cross-section of the channel – in which the biofilm was treated as as a uniform layer – it was used to indirectly evaluate a mean volume fraction of biofilm, Φ. We further visualized directly the channel using timelapse microscopy with differential interference contrast, bright field and fluorescence imaging. We validated our approach by comparing Φ calculated from hydraulic resistance with Φ estimated from fluorescence measurements. Strong correlation between these independent methods (mean r = 0.68 - 0.77 per condition, Fig. S21) confirms that pressure-based measurements accurately capture biofilm dynamics and that the uniform layer assumption is reasonable.

We found that biofilm development occurs in different phases, in a way that is consistent across flow rates. We propose to decompose the dynamics in two main components: Stage I that corresponds to the initial adhesion, growth and saturation; and stage II that features large fluctuations in the amount of biomass in the channel. Fig 3a illustrates our decomposition in two stages on the temporal evolution of $\frac{R}{R_0}$ in the case Q = 0.2 $\mu L/min$. The following sections detail the dynamics of Stages I and II.

Early stage I is driven by surface adhesion, motility, division and colony formation

Our inoculation process results in the sparse attachment of individual bacterial cells on the boundaries of the channel. On the glass slide, we evaluated the initial density to be about 38800 cells per mm^2. Growth of adhered cells started straight away upon flowing the culture medium,

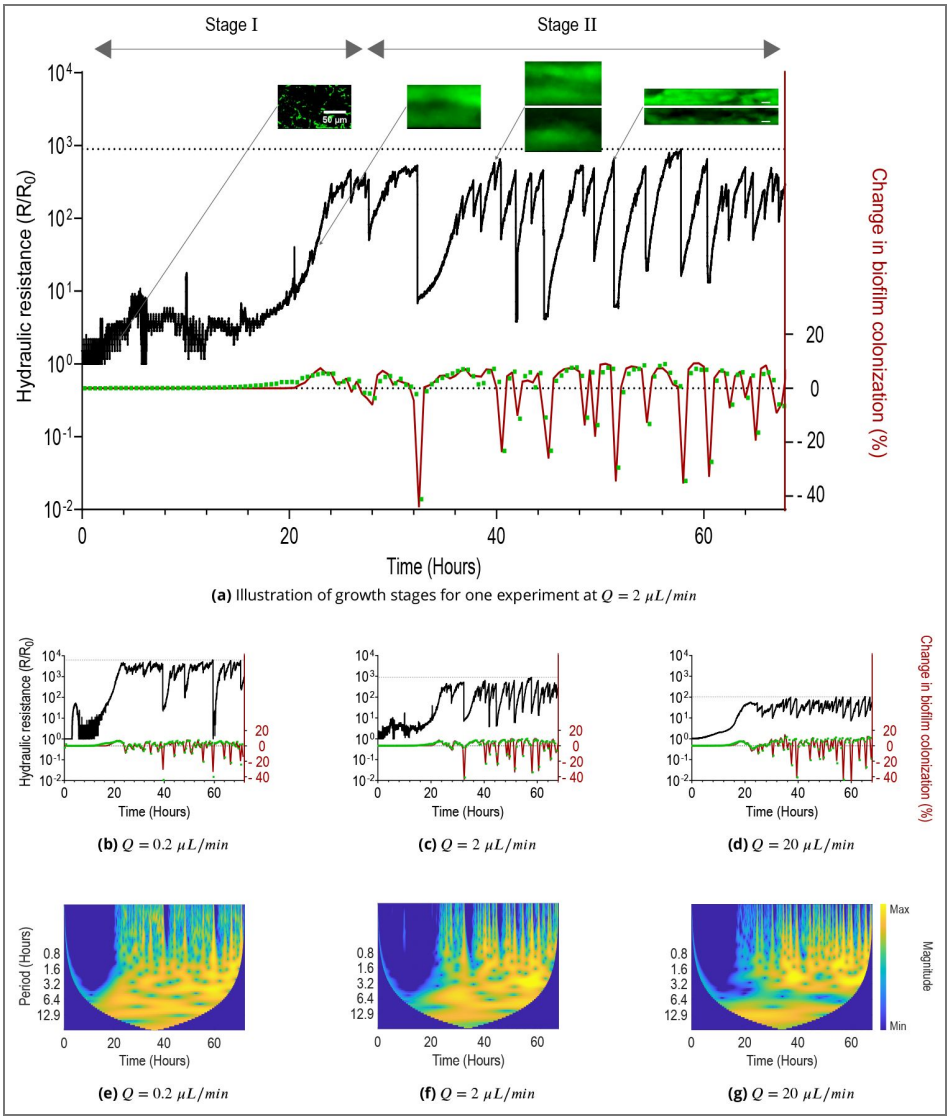

Figure 3. Temporal dynamics of growth and detachment for Q = 0.2 $\mu L/min$, 2 $\mu L/min$ and 20 $\mu L/min$.

(a): Summary of the two main stages of biofilm development. The figure shows the evolution of the hydraulic resistance (black solid line) in time, calculated from pressure measurements, and microscopy images corresponding to the different phases. It also shows changes in biofilm colonization extracted from either integrated fluorescence intensity (green squares) or from image segmentation (red solid line). (b), (c) and (d): Temporal dynamics of growth and detachment for the different flow rates. (e), (f) and (g): Wavelet scalograms of hydraulic resistance time series, corresponding to (b), (c) and (d). Blue stripes at short periods (near 0 hours) indicate sharp, rapid changes corresponding to sloughing events. The curved envelope at the bottom represents the cone of influence where edge effects occur.

with little to no lag time. The apparent macroscopic lag, as visible in Fig 3, does not stem from a lag at the cellular level, but rather from the sensitivity of the pressure measurements. The relative hydraulic resistance, $\frac{R}{R_0} = \frac{1}{(1-\phi)^2}$, can be linearized as $\frac{R}{R_0} \sim 1 + 2\phi$ when $\Phi \ll 1$. The evolution of $\frac{R}{R_0}$ with Φ is thus affine at the beginning of the experiment, with small changes in the hydraulic conductivity that could not be detected in our experimental system. This generates some amount of noise in the early signal, that tends to decrease when increasing flow rate.

To characterize the growth time at the cellular level, we calculated an apparent doubling time at the cellular level from microscopy images of cells attached to the glass slide in the very early stage (from 0 to 3.5 hours, see Fig 4e). We first segmented images from differential interference contrast microscopy to identify individual bacteria on the surface and then fitted linearly the log of the number of cells as a function of time. Calculated doubling times were measured as, on average, about 198 minutes (standard deviation ~ 14 minutes), 96 minutes (standard deviation ~ 8 minutes) and 117 minutes (standard deviation ~ 8 minutes) for, respectively, Q = 0.2 $\mu L/min$, 2 $\mu L/min$ and 20 $\mu L/min$. As a reference, the doubling time in liquid culture was measured as about 110 minutes (standard deviation of ~ 10 minutes). Although understanding exactly what generates this dependence of the doubling time upon the flow rate is beyond the scope of this paper, it is worth noting that nutrient limitation is not likely to play a role, as we have previously validated the fact that there is no limitation for $Q \geq 0.2$ $\mu L/min$, even when biofilm has formed. Mechanisms directly related to flow could mediate these phenomena (Sanfilippo et al., 2019; G.C. Padron, 2023; Rodesney et al., 2017), as well as heterogeneities in the rate of division – for instance between motile and adhered cells (Rossy et al., 2019) – or in the attachment/detachment dynamics. After this initial phase, colonies expand into mature biofilms, yielding a much sharper increase in hydraulic resistance. This increase stems from the combination of bacterial growth and the nonlinear relationship between between ${}^{R}/R_0$ and Φ, ${}^{R}/R_0 = (1 - \Phi)^{-2}$.

Late Stage I reflects an equilibrium between growth and detachment

We observe an inflection of the signal in late Stage I in Fig 3a, 3b, 3c, 3d. This inflection corresponds to the end of the rapid growth phase, with flow-induced detachment progressively increasing, until detachment equilibrates with growth. To further understand this effect, let us consider the mass balance of biofilm in the zone of interest – the zone where biofilm grows in between the two UVC irradiation zones – in the channel. The inlet flux of bacteria is zero, since our UVC system prevents growth outside the zone of interest. The source of biomass therefore only results from the uptake of nutrients, which yields division of bacterial cells and EPS production. The sink of biomass is due to flow-induced removal, which includes parts of the biofilm that are displaced out of the zone of interest through the flow/remodelling of the biofilm at the outlet, and parts that are washed away by erosion and seeding dispersal (Kaplan, 2010; Krsmanovic et al., 2021). This model captures a competition between growth and different types of smooth detachment – continuous, non-catastrophic biomass loss (as opposed to sudden sloughing events) – which occurs through three mechanisms: (1) biofilm flow, where viscoelastic deformation causes biofilm to move out of the observation zone; (2) erosion, the continuous release of single cells or small clusters from the biofilm surface; and (3) seeding, the release of cells from within the biofilm. In the absence of nutrient limitation, we can estimate the evolution of the biovolume in the channel from the ordinary differential equation

$$\dot{\phi} = \phi\left(1 - \frac{1-\phi_{\max}}{1-\phi}\right), \qquad (5)$$

which is a direct simplification of Eq 3 with Φ describing an average volume fraction in the entire channel, and thus being only a function of time. This model captures a competition between growth and different types of smooth detachment (flow, seeding, erosion).

Stage II features sloughing-induced jump events followed by re-growth

After growth and detachment start to equilibrate at the end of Stage I, sloughing events become particularly important. These are visible in Fig 3a, 3b, 3c, 3d as jumps in the hydraulic resistance. Wavelet scalogram analysis of the hydraulic resistance time series (Fig 3e, 3f, 3g)

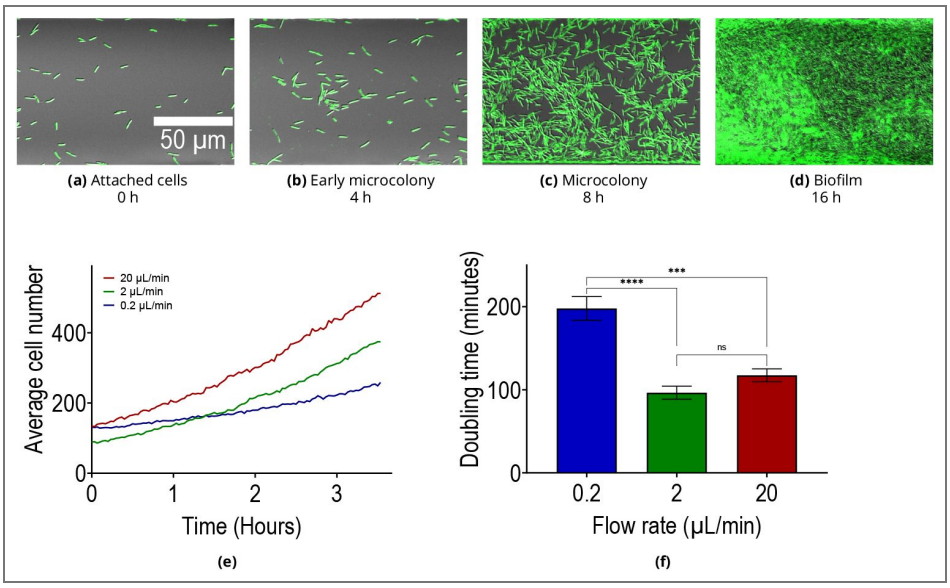

Figure 4. Flow modifies the apparent doubling time of bacteria on surfaces.

(a), (b), (c) and (d): Composite brightfield and GFP images of development stages, starting from single cells that form microcolonies and then evolve towards a biofilm. (e) and (f) show, respectively, the average number of cells on the surface as a function of time and the corresponding doubling time for flow rates (Q = 0.2 $\mu L/min$, 2 $\mu L/min$ and 20 $\mu L/min$). For (f), statistical differences were examined by unpaired Student's t-test with Gaussian distribution of data and equal standard deviations. Error bars indicate standard error of mean (SEM) and symbols denote statistical significance (****: p<0.0001, ***: p<0.001, ns: p > 0.05). The doubling time was calculated by a linear fitting of the logarithm of the number of cells. The slope was used to estimate growth rate and doubling time. Cell count was calculated from image segmentation of four positions in two channels to generate 8 measurements by condition (n= 8) for (Q = 0.2 $\mu L/min$, 2 $\mu L/min$ and 20 $\mu L/min$).

reveals the temporal dynamics of biofilm detachment throughout the growth cycle. The blue stripes at short periods (near 0 hours) indicate sharp, rapid changes in hydraulic resistance corresponding to sloughing events. Unlike time-averaged or Fourier methods, wavelet analysis uniquely identifies when these abrupt detachment events occur, showing that sloughing is an intermittent rather than continuous process. The jumps correspond to a range of different events, from minor detachment – where a relatively small portion of the biomass is detached – to major sloughing – where a large portion of the biomass is detached. Fig 5b shows example microscopy images of such events.

To better visualize the spatiotemporal dynamics and connect the different observations for the pressure and microscopy, we plotted kymographs in Fig 5c, 5d (see also SI figures S7, S10 and S13), showing both variations in time and in space, along with the corresponding hydraulic resistance signal. These graphics show clearly the correlation between the pressure signal on the right-hand side and the detachment events on the kymographs. We can readily identify that large drops in pressure correspond to large events with detachment over almost the entire length of the micro-channel. We also visualize a range of detachment events corresponding to various sizes of biofilm being detached, along the rapid increase of resistance and biomass following each sloughing event.

Each sloughing event is followed by a rapid growth phase resembling late Stage I, leading to a cycle of successive sloughing and re-growth. In each re-growth phase, we observe a sigmoid-like shape of the hydraulic resistance signal that is similar to Stage I. As in Stage I, the maximum stems from an equilibrium between growth and detachment. Φ_{max} thus corresponds to a critical value of the stress, σ_{crit}, that generates enough detachment to compensate growth. From Eqs 2-3, this reads

$$\sigma_{crit} = \sigma_0 \frac{R_{max}}{R_0}, \tag{6}$$

with R_{max} the maximum value of the hydraulic resistance. The maximum value of the hydraulic resistance over all stages of development decreases by orders of magnitudes from $20\ \mu L/min - \frac{R_{max}}{R_0} \simeq 8.2 \times 10^3$ for 0.2, $\simeq 8.4 \times 10^2$ for 2 and $\simeq 1.0 \times 10^2$ for 20. We can thus estimate the critical stress at about $\sigma_{crit} \simeq 100 - 200\ Pa$.

Pressure stress becomes prominent in late Stage I and Stage II

We now ask the question of whether the hydrodynamic stress is dominated by shear or pressure. We are particularly interested in understanding the nature of σ_{crit}. Fig 6 shows simple 2D flow simulations illustrating the types of stress induced by the flow of a viscous fluid upon the biofilm. We see that the shear stress becomes particularly strong in the bottlenecks and that the pressure difference also builds up, therefore generating both shear and pressure stresses. In the initial stages of bacterial development, when only individual cells and microcolonies are adhered to surfaces, we expect the dominant stress to be shear. However, what happens in later stages for large fractions of biofilm?

A simple approach to quantifying the relative importance of stresses in our system is to consider the case of uniform film growth between the UVC zones (see details in supplementary information). The tangential stress at the solid/biofilm surface is $\frac{\sigma}{\sigma_0} = (1-\phi)^{-2}$, with a contribution from shear $\frac{\sigma_{shear}}{\sigma_0} = (1-\phi)^{-1}$ and from pressure $\frac{\sigma_{pressure}}{\sigma_0} = \phi(1-\phi)^{-2}$. In the case of a fixed flow rate, we therefore have $\frac{\sigma_{shear}}{\sigma_0} \to 1$ and $\frac{\sigma_{pressure}}{\sigma_0} \to 0$ in the limit $\Phi \to 0$; $\sigma_{shear} = \sigma_{pressure}$ for $\Phi = 0.5$; and $\sigma_{pressure} > \sigma_{shear}$ for $\Phi > 0.5$. This simple conceptualization confirms that pressure stress tends to become dominant when a large portion of the channel is colonized, so that σ_{crit} is primarily a pressure stress. Furthermore, sloughing events mainly develop when the volume fraction is large suggesting that these events are also driven by pressure stress.

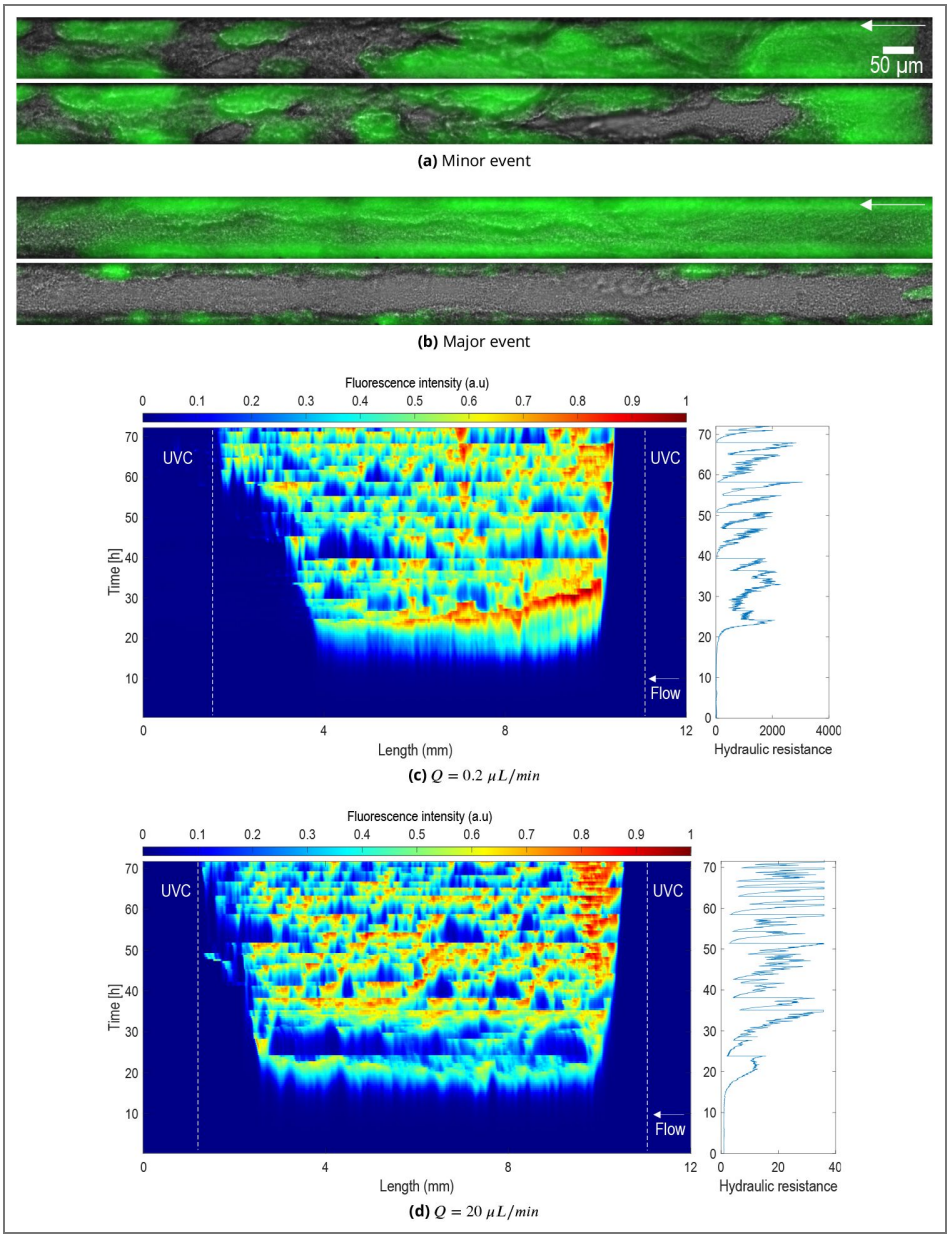

Figure 5. Spatiotemporal dynamics of sloughing in Stage II.

(a) and (b): composite bright field and GFP image of a ≃40 hour biofilm during Stage II. Image before (top, time t) and after (bottom, time t + 30 minutes) for (a) a minor sloughing event and (b) a major sloughing event. (c) and (d): kymographs showing the fluorescence intensity (averaged in the transverse direction y) as a function of both the longitudinal direction (x) and time. Fluorescence intensity values were normalized by the maximum value. Plots on the right-hand side show the corresponding normalized hydraulic resistance R_{max}/R_0 as a function of time.

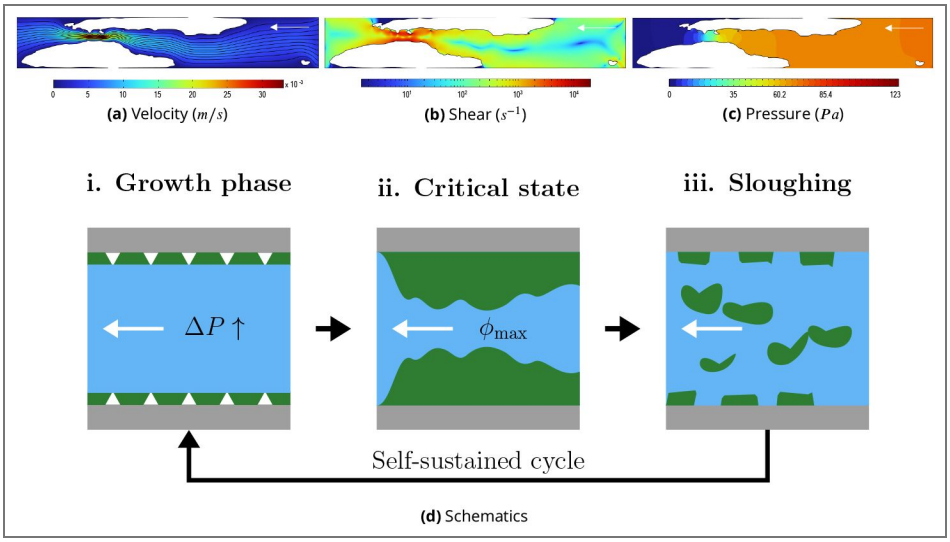

Figure 6. **Mechanisms of pressure increase.**

(a), (b) and (c): 2D simulations of flow around a biofilm (white) in a channel of 100 μm width and 500 μm length using COMSOL multiphysics. (a): Streamlines and magnitude of the velocity (m/s). (b): Shear rate in (s^{-1}). (c): Pressure field in ($P\,a$). (d) Schematics of growth and sloughing. The white arrows indicate the flow direction.

Maximum clogging depends on the flow rate

In our experiments, the maximum values of the volume fraction, estimated from hydraulic resistance, are Φ_{max} (Q = 0.2) = 0.989 for 0.2, Φ_{max} (Q = 2) = 0.966 for 2 and Φ_{max} (Q = 20) = 0.901 for 20 (see Fig 7a, 7b, 7c. and Table 1) – remarkably, this maximum is very reproducible across replicates, with standard deviations for volume fractions in the range of 10^{-3} in our experiments (Fig 7).

The model Eq 5 for Stage I is consistent with this dependence upon the flow rate. By definition of Φ_{max} in Eqs 2-3 and in Eq 5, we have

$$\phi_{max} = 1 - \frac{\chi X (1+K^\star)}{Y\alpha}\left(\frac{A}{4}\frac{\mu Q}{h^3}\right)^{\frac{1}{2}}. \quad (7)$$

We can express this relatively to a reference flow rate as

$$\frac{1-\phi_{max}(Q)}{1-\phi_{max}(Q_{ref})} \propto \left(\frac{Q}{Q_{ref}}\right)^{\frac{1}{2}}. \quad (8)$$

Upon considering $Q_{ref} \equiv 0.2$ with Φ_{max} Q_{ref} = 0.989, we obtain $\phi_{max}^{theoretical}(Q=2) \simeq 0.966$ and $\phi_{max}^{theoretical}(Q=20) \simeq 0.901$ from Eq 8. These values are in excellent agreement with the experiments (see Table 1).

To further validate this idea that Φ_{max} decreases with the square root of the flow rate (Eq 8), we performed a single experiment at 200 $\mu L/min$. Results in Fig 7d indicate that the behavior is similar to that of other flow rates, but with a significantly lower value of $\Phi_{max} \simeq 0.786$. We also see that the scaling remains remarkably similar with $1-\phi_{max} \sim Q^{\frac{1}{2}}$ in the range [0.2, 200] – equivalently, the scaling for the hydraulic resistance is $R_{max} \sim Q^{-1}$ (see Fig S19). The fact that the model can recover the correct scalings is an important validation of our modeling hypotheses, in particular that the detachment rate depends on square root of the hydrodynamic stress.

Maximum clogging depends on the composition of the biofilm

Modifications of the composition and mechanical properties of the biofilm should have a significant impact on the value of Φ_{max}. Among *P. aeruginosa* PAO1 polysaccharides – Pel, Psl and alginate – Pel and Psl are considered the two primary components of the EPS matrix structure (Ryder et al., 2007), controlling the cohesive and adhesive strength of the biofilm. We therefore performed experiments with mutants that cannot produce either Pel or Psl, with the idea that this should modify the value of χ. The Psl mutant is a *pslD* deficient Δ*pslD* obtained from *P. aeruginosa* PAO1 by non-polar allelic exchange (Colvin et al., 2012). The Pel mutant is a pelF deficient strain Δ*pelF* also obtained by allelic exchange (Colvin et al., 2011). Liquid culture showed that the lag and doubling times were, respectively, 233.36 and 105.5 minutes. Fig 8 (see also S15, S16, S17 and S18) shows the behavior of mutants compared to the wild type. We found that the volume fraction of biofilm was significantly lower for both mutants and that the Psl mutant was more strongly affected than the Pel mutant. The Psl mutant only weakly attached to the surface and was more prone to detachment – an observation that is consistent with the prominent role of Psl in the mechanics of PAO1 biofilms (Colvin et al., 2011). For the case 2 $\mu L/min$, we even observed an almost complete detachment of the biofilm with only few cells remaining attached and making re-growth possible after a sloughing event. At 20 $\mu L/min$, no effect was visible on the pressure measurements.

Biofilm development is stochastic

The model presented so far can describe Stage I and the signal in between two sloughing events, but not the catastrophic jumps associated with sloughing. To characterize the latter, we first performed a frequency analysis of the signal, as shown in Fig 9a. This approach did not prove very informative as it essentially shows a power spectrum typical of noise, with a slope roughly smaller than −2. This result, however, motivated the construction of a more physical representation of the process. The basis of this representation is the observation that fluctuations have a very specific signature on the hydraulic resistance: they first feature a sharp decrease due

Figure 7. Evolution of the distribution and maximum of the volume fraction for the different flow rates.

(a), (b), (c) and (d): Volume fraction in the microchannel, calculated from hydraulic resistance (black solid line) or estimated from integrated GFP intensity (green dotted line), for the different flow rates. These independent measurements are strongly correlated (Fig. S21). (e): Distribution of biofilm fraction calculated from hydraulic resistance between 24 and 72 h for all flow rates, represented as whisker boxes. (f): Log-log plot of $1 - \Phi_{max}$, with volume fraction calculated from hydraulic resistance, as a function of the flow rate (Q = 0.2 $\mu L/min$, 2 $\mu L/min$, 20 $\mu L/min$ and 200 $\mu L/min$). The red dotted line simply shows the slope for an evolution with the square root of the flow rate.

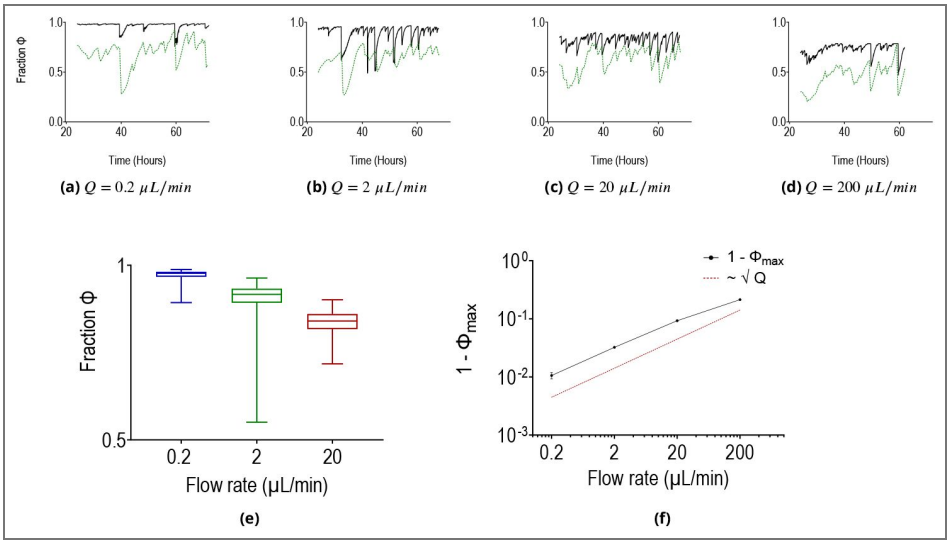

Figure 8. Fraction of biofilm obtained from image segmentation for the Δ*psl* (red line) and Δ*pel* strains (green line) compared to the wild-type strain (blue line), for (*Q* = 0.2 *μL/min*, 2 *μL/min*).

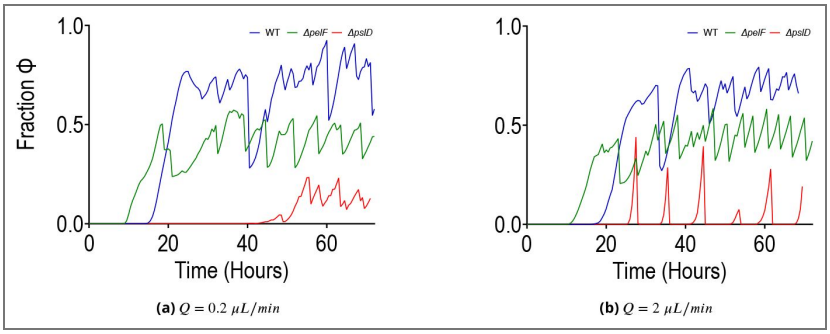

to sudden sloughing, followed by a slower increase due to growth. Since growth and smooth biofilm detachment are already described in the model, this observation suggests that we only need to capture the sudden sloughing to improve the description. The model takes the form of the following stochastic differential equation,

$$d\phi_t = \phi_t \left(1 - \frac{1-\phi_{\max}}{1-\phi_t}\right) dt - \phi_{t^-} dN_t, \qquad (9)$$

with Φ_t describing the average fraction of biofilm in the microchannel, N the jumps and ϕ_{t^-} the value of Φ at time t^- just before the jump.

The challenging part of this representation is to accurately describe the randomness of the process N – which is likely strongly dependent upon spatial heterogeneities, for instance in the initial attachment of bacteria. We characterized N in our experiments via the distributions of both the times between two successive jumps and the relative amplitudes of the jumps – i.e. the amplitude of each jump divided by the value of the volume fraction just before the jump ϕ_{t^-}. Fig 9b, 9c shows histograms of these distributions extracted from signal processing of the experimental data (see Material and Methods). We see that the distribution of times between successive jumps, δt, can be well approximated by a Gamma distribution – solid lines in Fig 9b for a fit of the experimental data (see Supplementary figure S20 for quantile-quantile plots). The relative amplitude of each jump $\xi = {}^{\Delta\phi}/_{\phi_{t^-}}$ was better represented by log-normal distributions – solid lines in Fig 9c for a fit of the experimental data. Example realizations of the simulations are presented in Fig 9d, 9e, 9f for the flow rates used in the experiments. Simulations are strikingly similar to experimental data, thus suggesting that sloughing can indeed be accurately modeled as a stochastic jump process.

Discussion

Regimes of nutrients and oxygen transport

Our experimental setup, which implements a novel UVC strategy to confine biofilm development within a specific zone in the channels, allowed us to finely control boundary conditions and study the role of molecular transport on biofilm development. Our results suggest that, in confined channels, the longitudinal distribution of biofilm ensues from a competition between advective transport of solutes along the channel and uptake by the cells. Modeling molecular transport as an advection-diffusion-reaction equation, this effect can be quantified using the ratio of longitudinal Péclet and Damköhler numbers, ${}^{Pe}/{Da}$, which compares advection to reaction. When ${}^{Pe}/{Da} < 1$, biofilm growth is nutrient-limited and localized close to the inlet. When ${}^{Pe}/{Da} > 1$, biofilm development is close to homogeneous. In the transverse direction, the limitation can be characterized in a similar way via a transverse Damköhler number, $Da_{\text{transverse}}$, defined as the ratio of reaction and transverse diffusion. In our experiments, we always had $Da_{\text{transverse}} < 1$ with only weak gradients and no transverse limitation.

Although the competition between advective/diffusive transport and uptake is a universal feature of biofilm development in flow, the solute that becomes limiting depends on the details of the setup. In our experiments, we found that nutrients were restricting growth, while other works in microchannel flows, such as (Thomen et al., 2017), found that the effect of oxygen was dominant. Several factors play an important role here, including the composition of the growth medium, the catabolism of the microorganisms, the kinetics or even the resilience of bacteria to low oxygen concentration. For instance, Thomen et al. (2017) focused on an *E. coli* K12 derivative. *E. coli* can respond strongly to micro-aerobiosis (Colón-González et al., 2004), whereas *P. aeruginosa* is known to be more resilient (Sabra et al., 2002; Alvarez-Ortega and Harwood, 2007). Factors that affect transport characteristic times, such as the flow velocity or the dimensions of the channels, also modify the competition with uptake. The length of the channel modulates the time for advective transport along the channel and therefore the ratio

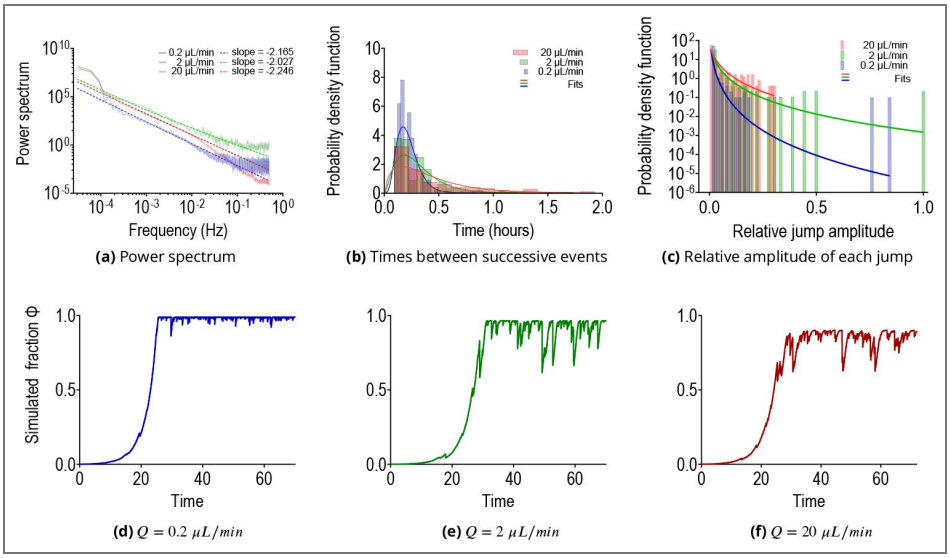

Figure 9. Stage II detachment events can be described as a jump process.

(a) Power spectrum for the different flow rates (Q = 0.2 $\mu L/min$, 2 $\mu L/min$ and 20 $\mu L/min$, 3 replicates for each). Slopes are indicative and were calculated in the interval between 0 and 0.25 Hz. (b) Probability density function of the time between two successive jump events, δt, for (Q = 0.2 $\mu L/min$, 2 $\mu L/min$ and 20 $\mu L/min$). The histograms are calculated from data from all experiments/replicates, while the solid lines are fitted Gamma distributions $(\delta t)^{a-1}/(b^a\Gamma(a))\exp(-\delta t/b)$. (c) Probability density function of the relative amplitude of jump events, $\xi = \Delta\phi/\phi_{t^-}$ for (Q = 0.2 $\mu L/min$, 2 $\mu L/min$ and 20 $\mu L/min$). The histograms are calculated from all experiments/replicates, while the solid lines are fitted log-normal distributions $1/\left(\xi\sigma\sqrt{2\pi}\right)\exp\left(-(\ln\xi-\mu)^2/(2\sigma^2)\right)$.(d), (e) and (f): Stochastic simulations of the volume fraction as a function of time for (Q = 0.2 $\mu L/min$, 2 $\mu L/min$ and 20 $\mu L/min$), which can be compared to experimental results in Fig 7.

$^{Pe}/Da$. The width and height control the characteristic time for transverse diffusion. In Thomen et al. (2017), for instance, the width of the channel is 1000 μm so that diffusion takes about 100 times longer and $Da_{\text{transverse}}$ is 100 times larger than for 100 μm channels.

Temporal dynamics and hydrodynamic stresses

With these regimes clearly identified for molecular transport, we could then study the effect of hydrodynamic stresses on biofilm development and, in particular, the role of flow-induced detachment on the spatiotemporal dynamics. We suppressed any form of nutrient limitation, either transverse or longitudinal, by focusing on flow rates ≥ 0.2 $\mu L/min$ with $^{Pe}/Da > 1$ and $Da_{\text{transverse}} < 1$. In so doing, we found that the time response featured two distinct stages: the hydraulic resistance first followed a relatively standard sigmoid-like pattern (Stage I), but then switched to a different regime with large self-sustained fluctuations (Stage II). As discussed in what follows, we argue that this Stage II is a signature effect of biofilm development in confined flow.

Stage I began just after initial inoculation, as soon as the culture medium started flowing in the microchannel. Early Stage I was dominated by cell adhesion, division, surface motility and microcolony formation. The average velocity in the channel at 0.2 $\mu L/min$ is above 300 $\mu m/s$ so bulk motility is likely not playing an important role when $Q \geq 0.2$ $\mu L/min$ (Rossy et al., 2019). Contrary to Thomen et al. (2017) – where no direct initiation of the biofilm of *E. coli* biofilm was possible above a shear stress of 10 $mP\,a$ – our results show that *P. aeruginosa* PAO1 strongly adhered to the surface and could initiate biofilm formation for all shear stresses. We even observed that the apparent doubling time within the first few hours of growth was the smallest in the case at 2 *Pa*. Stage I then evolved towards the standard steps of biofilm formation for *P. aeruginosa* (Rasamiravaka et al., 2015; Krsmanovic et al., 2021), with clonal microcolonies that extended, joined together and grew into mature biofilms. The exponential growth and EPS production yielded a sharp increase of the hydraulic resistance by several orders of magnitude, which is consistent with previous works (Cunningham et al., 1991; Desmond et al., 2022).

Stage II was characterized by large fluctuations in the hydraulic resistance and in the quantity of biomass in the channel. We showed that these fluctuations are the result of successive cycles of growth and sloughing events: parts of the biofilm get detached by the flow upon reaching a critical stress, generating sharp discrete-like events of detachment, followed by a fast re-growth of the biofilm. In both late Stage I and in Stage II, pressure-induced stresses play a crucial role. Most works have focused on shear stress (Krsmanovic et al., 2021; Kurz et al., 2022; Telgmann et al., 2004; Wagner et al., 2010; Paul et al., 2012) because, in many situations, such as biofilm development in large reactors, the effect of pressure can be neglected. However, this is not the case in confined systems, where biofilm can clog a large proportion of the flow channels and the pressure build-up induced by clogging can generate an important force on the biofilm.

Maximum clogging

One aspect that stands out in our experiments, because of its physical meaning and reproducibility across replicates, is the concept of maximum clogging. In Stage I and after each sloughing in Stage II, curves for the hydraulic resistance had a sigmoid-like shape, with an inflection that was a signature of a competition between growth and smooth detachment due to erosion, seeding and biofilm flow outside the zone of interest. We found that the maximum value of the hydraulic resistance across the entire experiment scales with the inverse of the flow rate, which is consistent with our modeling hypothesis that smooth detachment scales with the square root of the tangential stress at the solid/biofilm interface (which includes pressure contributions), rather than with shear stress at the biofilm/fluid interface as in previous reactor studies. This concept of maximum clogging can also be expressed as a critical value of the hydrodynamic stress generating enough detachment to compensate growth. In our framework, this equilibrium stress was in the order of 100-200 Pascals for the wild type and did not vary significantly with the flow rate.

To further understand the role of the EPS matrix composition on maximum clogging, we studied the behavior of Δpsl and Δpel mutants. Pel and Psl are the two main exopolysacharides produced by nonmucoid strains of *P. aeruginosa*. For both mutants, the maximum amount of biofilm in the microchannel was lower than for the wild type, thus indicating that these mutants are more easily detached by the flow. We also found that Psl had a stronger impact than Pel on the spatiotemporal dynamics and, in particular, on maximum clogging. The Δpsl mutant even featured major sloughing events for 2 $\mu L/min$ that led to a near-complete removal of the biofilm. On the other hand, Pel featured a dynamics similar to that of the wild type, but with a reduced maximum clogging.

Although critical stresses are widely used in characterizing flow-induced detachment of biofilms, they have a broad range of different meanings and values. Critical stresses have been used to characterize a form of complete detachment from the solid surface (Jiang et al., 2021). Ohashi and Harada (1996) described an adhesion strength as the stress required to remove the biofilm – upon conceptualizing the problem as a surface to surface bonding, the adhesive strength has also been defined as the work required to detach the biofilm from the surface per surface area (in Joule per m^2) (Chen et al., 1998). Ohashi and Harada (1996) found values for the shear strength in the hundreds of Pascals. Lau et al. (2009) measured an adhesive pressure – adhesive force measured by microbead force spectroscopy divided by contact area – for *P. aeruginosa* PAO1 that was in the tens of Pascals. Körstgens et al. (2001) studied the yield strength of a mucoid *P. aeruginosa* strain, discussing its role in the mechanical failure of the biofilm. Considering the biofilm as a viscoelastic gel with plastic flow properties, they found a stress at failure close to 1000 *Pa*. Lee et al. (2023) show that bio-aggregates of *E. coli* at pore throats become fluidized above a critical value of the shear stress with a yield point at roughly 1.8 *Pa*. To establish a clear link between these values, our critical stress at 100-200 Pascals and the observed dynamics of sloughing in Stage II, future works will need to further refine our understanding of the role of the different variables on flow-induced detachment, including distributions of stresses within biofilms, adhesive strength to surfaces, mechanical properties of the biofilm, or bacterial regulation through quorum sensing (Emerenini et al., 21 juil. 2015) and/or rhamnolipids production (Boles et al., 2005).

Self-sustained fluctuations

Fluctuations of the hydraulic resistance were previously reported in porous media flows. Howell and Atkinson (1976) showed that, in trickling filters, constant influent concentration and operating conditions can yield large fluctuations induced by sloughing events. (Stewart and Scott Fogler, 2002) found very large oscillations in the pressure signal due to the formation of successive stable or unstable dextran plugs of *Leuconostoc mesenteroides* biofilm, behaving in a way similar to a yield stress fluid, and allowing flow only through breakthrough channels – see also discussions on the flow of yield stress fluids through porous media in (Talon, 2022). Sharp et al. (2005) showed that “the pore channels are dynamic, changing in sized, number and location with time” in a flat plate reactor colonized by *Vibrio fischeri* biofilm. Kurz et al. (2022) found successive cycles of growth and shear-induced detachment in the preferential flow paths for *Bacillus subtilis* biofilm development in a microfluidic system with cylindrical obstacles. Bottero et al. (2013) modeled the coupled effects of flow, clogging and detachment to study the mechanisms that control these self-sustained fluctuations, in particular what leads to the clogging of a preferential flow path and the unclogging of another one – contrary to the development of stable flow paths.

Porous media have an inherent degree of complexity in the geometry that, combined with the nonlinear response of biofilms, can lead to a range of complex mechanisms. For instance, some of the works above-mentioned identified changes in the flow paths associated with the fluctuations. Our work shows that, even in a single channel with continuous flow, these fluctuations occur and prevent the system from reaching a true steady state. We therefore argue that the self-sustained fluctuations observed in Stage II are a signature of biofilm development in confined flows, even in the simplest geometries. The idea is that the strong bioclogging in confined geometries generates a

pressure build-up that ultimately leads to sloughing, followed by re-growth. Our work therefore highlights the ubiquity of these fluctuations, which are likely playing an important role in the development and spreading of biofilms in a range of different systems, such as clogging in pipes, catheters (Stickler, 2014) or stents (Guaglianone et al., 2010), with applications ranging from infections, to environmental processes and engineering systems.

Stochastic modeling

Our approach to modeling was constructed in two main parts. We first proposed differential equations to describe nutrient transport coupled with the dynamics of biofilm development in the channel, including growth and smooth detachment. The sharp jumps corresponding to sloughing were then added to this first layer of the model as a jump stochastic process. Although it seems quite natural to characterize the statistics of detachment (Wilson et al., 2004), there are actually very few attempts to treat such problems in the framework of stochastic processes. Howell and Atkinson (1976) modeled sloughing in trickling filters through a conceptualization as connected filter units describing the discrete pieces of packing material in the filter. They introduced randomness by permitting sloughing at multiples of a fixed time interval. Bohn et al. (2007) used an approach combining a logistic growth with random sloughing events through a stochastic differential equation. They described sloughing via a discrete expression of the amplitude of jumps occurring independently at each time step, which allowed them do describe daily fluctuations in light absorbance data for phototrophic biofilms development in a flow-lane incubator. In our approach, the jump process was characterized by two random variables: the interevent time between two successive jumps and the relative amplitudes of the jumps. Through the analysis of experimental data, we reconstructed the probability density functions for these random variables, with respectively Gamma and log-normal distributions.

There have been previous discussions (Lewandowski et al., 2004) on the determinism of biofilm formation, suggesting that sloughing events are intrinsically random events that generate large fluctuations, prevent the system from reaching a steady state and hinder the reproducibility of longterm experiments. Our work confirms that sloughing is integral to biofilm development (Telgmann et al., 2004) but shows that, although a true steady state is never reached, the fluctuations can be precisely characterized using stochastic modeling. This approach paves a way forward in terms of reproducibility: even though the state of the biofilm at any given time may not be reproducible, the randomness of the process may very well be.

Our approach to characterizing bursting events in terms of the distribution of the amplitude and interevent time is reminiscent of the description of other physical systems, such as avalanches (Maaß et al., 2015). For earthquakes, for example, a Gamma distribution for interevent times has been found in many different geographic regions (Corral, 2004). The fact that interevent times for biofilm sloughing also seem to follow a Gamma distribution may point towards specific physical mechanisms (Kumar et al., 2020), which could be used to better understand the physics of sloughing. One interesting perspective of this work is also to assess the universality of these distributions across microorganisms and whether we could define classes of bacteria with specific signatures on the stochastic process. With the same idea, we could further evaluate the impact of ecological interactions in multispecies biofilm or the effect of various molecules, such as biocides, on the sloughing dynamics.

Material and Methods

Bacteria and cultures

Experiments were performed using *Pseudomonas aeruginosa* PAO1 GFP (ATCC 15692GFP) strain, along with PAO1 GFP Δ*pslD* and Δ*pelF* mutants obtained from Colvin et al. (2011, 2012) and built by non-polar deletion through allelic replacement of *pslD* and *pelF* operon and harbor pMRP9-1 plasmid expressing GFP. Bacteria were subcultured and grown in brain heart infusion (Sigma Aldrich, Saint-Quentin-Fallavier, France). Cultures were prepared from −80°C frozen aliquots spread on tryptic soy agar plate (Sigma Aldrich, Saint-Quentin-Fallavier, France) supplemented

with 300 µg/mL of ampicillin (Sigma Aldrich) then incubated at 30°C during 24 h. Liquid cultures were prepared from the second subcluture on tryptic soy agar by spreading a 24 hours single colony diluted in brain heart infusion media supplemented with 300 µg/mL of ampicillin. 1*X* concentrated BHI media was prepared by dissolving 37 *g* of commercial powder in demineralized water and autoclaved with a liquid cycle (121°C for 15 minutes). 0.2*X*concentrated BHI media was obtained by dissolving 7.4 *g* while a third 1*X* solution was supplemented by 8 *g*/*L* of D-Glucose (Sigma Aldrich).

Growth rate measurements in liquid culture

We determined growth curves for the first 35 hours of incubation using a microplate reader. All strains were refreshed from –80°C freezer stocks: 2 µL of frozen culture was diluted in 1 mL BHI supplemented with 300 µg/mL ampicillin. Initial optical density (OD_{640}) was below the detection limit of the spectrophotometer. 100 µL of each suspension was transferred to a 96-well plate in an automatic microplate reader (TECAN-PC2017, 640 nm, 26°C). Note that microfluidic experiments were performed at room temperature. Each strain was measured in triplicate wells (technical replicates from the same biological sample) under static conditions, with 10 seconds of shaking at 90 rpm before each reading. Growth dynamics were measured every 10 minutes for 35 hours. For each well, 9 measurement points at different spatial positions were acquired and averaged at each time point. Doubling time was estimated during the exponential growth phase using the slope of the linear fit of the ln-transformed growth curve (doubling time = ln(2)/slope). The exponential phase was identified by excluding the lag phase, which was estimated using the DMfit tool (linear biphasic model).

Microfabrication

Microchannels were fabricated using standard soft lithography techniques. Microchannel molds were prepared by depositing 100 µm SUEX sheets on a silicium wafer via photolithography. The negative mold was cleaned by isopropanol and silanized with trichloromethylsilane (Sigma Aldrich). Square cross-section channels had dimensions of 100 µm height by 100 µm width and 20 mm length. The chips were prepared with a 10% wt/wt cross-linking agent in the polydimethylsiloxane solution (Sylgard 184 Silicone Elastomer Kit, Dow Corning). PDMS was cleaned with isopropanol at 80 °C for 30 minutes and plasma-bonded to a clean glass coverslide.

Inoculation and flow experiments

BHI suspensions were adjusted at optical density at $OD_{640\ nm}$= 0.2 (10^8 *CF U*/*mL*) and inoculated inside the microchannels from the outlet, up to approximately ^{3}/4 of the channel length in order to keep a clean inlet. The system was let at room temperature (25°C) for 3h under static conditions. Flow experiments were then performed at 0.02, 0.2, 2, 20 and 200 *µL*/*min* constant flow rates for 72h in the microchannels at room temperature. For the experiments at 0.2, 2, 20 and 200 *µL*/*min*, the fluidic system was based on a sterile culture medium reservoir pressurized by a pressure controller (Fluigent FlowEZ) and connected with a flow rate controller (Fluigent Flow unit). The flow rate was maintained constant by using a controller with a feedback loop adjusting the pressure in the liquid reservoir. The reservoir was connected to the chip using Tygon tubing (Saint Gobain Life Sciences Tygon™ ND 100-80) of 0.52 mm internal diameter and 1.52 mm external diameter, along with PEEK tubing (Cytiva Akta pure) with 0.25 mm inner diameter adapters for flow rate controller. The waste container was also pressurized by another independent pressure controller to reduce air bubble formation in the inlet part. For the experiments at 0.02 *µL*/*min*, we used an Harvard Phd2000 syringe pump for the flow.

UVC irradiation

The biofilm is constrained in a part of the microchannel using UVC irradiation directly through the PDMS of the microfluidic chips, thus reducing contamination risk and avoiding unwanted progression/growth of *P. aeruginosa* in the inlet and tubing for several days of experiment (Ramos

et al., 2023). This eliminates parasitic consumption of nutrients in various parts of the fluidic system and maintain a controlled boundary condition with a fixed concentration of nutrients at the inlet of our zone of interest.

To this end, the inlet and outlet of the microchannels were exposed to UVC light by a system of UVC LEDs (Ramos et al., 2023). The system consists of a 3D printed part called the guide carrying in its backside a PCB with a LED light source that delivers UV-C light of 1W power. The light beam follows a straight trajectory until a 45° mirror positioned in the front side of the guide, which reflects the light parallel to the PDMS chip and irradiate it. UVC guides were positioned in both sides of the PDMS microchannel and separated by a 1.2 cm distance to keep a central area unexposed. UVC power is measured by a radiometer after mirror reflection and delivers a power of 200 mW/m^2equivalent to 2 mJ/cm^2. The guide is elevated to fit with the PDMS chip dimensions and contains a barrier located in the front side that blocks the diffusion of light through the PDMS polymer in the horizontal direction.

Mass spectrometry analysis

Mass spectrometry analysis was performed on a Thermo Scientific Q Exactive Focus Orbitrap LCMS/MS system connected to a LC device Thermo Scientific Vanquish UPLC system with PDA detection. Analytical separations were performed on a 150 x 2.1 mm Thermo Hypersyl Gold C18 column (1.9 µm) using an MeCN/H2O 1% formic acid gradient. Data were captured in full MS scan mode and processed using Chromeleon 7 software.

Imaging for the biofilm experiment

Bacterial development was imaged for a period of 72 hours with a timestep of 30 minutes at 25°C on an inverted microscope (Ti-2E, Nikon) using a digital camera (back-illuminated PCO edge). Time-lapse images were acquired using brightfield and fluorescence microscopy (Sola light source 10% intensity with 30 ms exposure with 500 *nm* excitation and 513 *nm* emission combined with (FITC filter). Images were obtained with a focal plan at the glass/liquid interface. These images had dimensions of 30086 x 154 pixels obtained after multi position scanning using automatic Nikon platform and assembled by Nikon NIS software of single images with 0.65 µm/pixel using a 10X magnification Nikon objective (NA = 0.3).

Image analysis for the biofilm distribution in the longitudinal direction

Fluorescence images were loaded as a matrix (30086 x 154) in MATLAB (MathWorks). For each time acquisition, the signal was first integrated in the transverse direction to obtain a mean distribution in the longitudinal direction. In plotting curves to analyze the effect of nutrients, all timepoints were then averaged to obtain one dimensional curves of the mean longitudinal profile. For kymographs, one dimensional curves for each time point were stacked together to describe the spatiotemporal dynamics. The intensity values were normalized to the maximum values of each replicate over all times. For each flow and nutrient condition, three biological replicates were performed.

Image analysis for the biofilm segmentation

To estimate changes in channel colonization, GFP images were binarized using a machine learning software (Ilastik) (Berg et al., 2019). Images were pre-treated with imageJ (Schneider et al., 2012) by normalizing all pixel values between 0 and 65535 grayscale levels. In Ilastik, biofilm structures were first differentiated from the empty flow path using pixel-level manual labeling during pixel classification where visible patches of biofilm and empty channel were annotated manually by mouse cursor. Pixel classification workflow employs a Random Forest classifier, known for its generalization properties. Several samples of biofilm and background images were used to train the classifier by annotating pixels with corresponding labels, allowing the algorithm to learn and make predictions in real-time. The chosen features were color, intensity, edges, and texture. The generated probability maps indicating the likelihood of each class at every pixel were

used for the object classification and were thresholded at a value of 0.6 with no size filter. Thresholding is a process involved in converting continuous probability maps generated from pixel classification into binary segmentation images by setting a threshold, where pixels above the threshold are classified as belonging to an object. The size, intensity, position and convexity of the biofilm objects was exported in .cvs format and further analysed in matlab. Volumic fraction of biofilm in microchannel was calculated from the sum of the size of segmented objects divided by the interest growth area (non UVC irradiated central part of microchannel).

Initial adhesion

Separate experiments were performed to study the behavior of cells in the initial phases of attachment in order to increase spatial and temporal resolution. Liquid cultures were prepared following the same protocol as described previously (see Bacteria and cultures). Sterile 1× concentrated BHI culture medium supplemented by 300 $\mu g/mL$ of ampicillin was flowed under constant flow rate (Q = 0.2 $\mu L/min$, 2 $\mu L/min$ and 20 $\mu L/min$) after 3 hours under static conditions at 26° C.

Images were obtained with a 40× Nikon objective (NA = 0.95) using a differential interference contrast (DIC) brightfield with 2 minutes per frame during 3.5 Hours. Replicates were obtained by imaging four positions per channel and each condition was performed in two distinct channels forming two distinct biological replicates to obtain n = 8 replicates by condition (Q = 0.2 $\mu L/min$, 2 $\mu L/min$ and 20 $\mu L/min$). The images were further segmented using Ilastik with the same parameters as described before (see Image analysis for the biofilm segmentation) and single cells were selected as objects with an area higher than 20 μm^2 to avoid counting dust particles and artefacts that could be considered as distinct objects by Ilastik. The doubling time was calculated in the window between 0 and 3.5 hours by a a linear fitting of the logarithm of the number of cells. The slope was used to estimate growth rate and doubling time. Cell count was calculated from image segmentation of four positions in two channels to generate 8 replicates by condition (n= 8) for (Q = 0.2 $\mu L/min$, 2 $\mu L/min$ and 20 $\mu L/min$).

Wavelet analysis

Time series of the pressure data were investigated with a wavelet analysis to identify temporal variations of spectral power (Torrence and Compo, 1998). Wavelet analysis was carried out using a Morlet wavelet, the product of a sinusoidal wave and a Gaussian envelope, with a frequency parameter of 6 and scale width of 300. We then applied a continuous wavelet transform (CWT) results which gives wave power coefficients dependent on the scale or period and the time, as well as a cone of influence (COI), where edge effects become important. The time series were zeropadded to reduce the edge errors. The curved envelope at the bottom of the scalogram in Fig 3 represents the cone of influence, where edge effects limit the reliability of wavelet coefficients at longer periods near the beginning and end of the time series.

Data analysis for the calculation of the hydraulic resistance and volume fraction

Our approach to quantifying biofilm volume fraction relies on pressure drop measurements, which inherently capture the three-dimensional architecture of the biofilm. The uniform layer assumption is supported by: (i) the excellent quantitative agreement between predicted and measured scaling laws ($\Phi_{max} \propto Q^{1/2}$, Fig 7f), (ii) the consistency of Φ_{max} values across different flow rates and replicates, and (iii) the strong correlation between model-derived $\Phi(t)$ and integrated fluorescence intensity (Figs 3 and 7). While fluorescence microscopy provides information on a limited depth in the channel, its agreement with the pressure-based $\Phi(t)$ suggests it captures the overall colonization dynamics.

Recorded pressure fluctuations in the reservoir were converted to hydraulic resistance in the 10 mm zone between UVC LEDs where biofilm develops. We write the difference between the two pressure reservoirs (one at the inlet and one at the outlet) as ΔP_{res} and express it as

$$\Delta P_{res}(t) = \left(\sum_i R_i + R(t)\right) Q$$

with Q the imposed flow rate, $\sum_i R_i$ the sum of the hydraulic resistance of the different part of the hydraulic network and $R(t)$ the hydraulic resistance of the the 10 mm zone between UVC LEDs. To estimate $R(t)$, we evaluated $\sum_i R_i$ from the mean value of ΔP_{res}, which we write $\overline{\Delta P}_{res}$, over a few hours of the experiment where biofilm growth is not yet observable. We then use

$$\sum_i R_i = \frac{\overline{\Delta P}_{res}}{Q} - R(t=0),$$

which yields

$$\frac{R(t)}{R(t=0)} = 1 + \frac{\Delta P_{res}(t) - \overline{\Delta P}_{res}}{Q\, R(t=0)},$$

with $R(t = 0)$ in the square cross-section of size $h_0 = 100\ \mu m$ that can be estimated as

$$R(t=0) \simeq \frac{12\eta L}{1 - 0.917 \times 0.63}\frac{1}{h^4}$$

with η the viscosity of the culture medium at 25°C, $L = 10\ mm$ the length of the channel and h the width/height of the channel. Since we considered $\overline{\Delta P}_{res}$ for the normalization, and because the low pressure signal is relatively noisy at the beginning, we also only use the part of the signal for which $\frac{R(t)}{R(t=0)} \geq 1$ – it is a important, for instance, to obtain non-negative volume fractions of biofilm that are only the result of the initial noise. Upon assuming that the biofilm forms a uniform layer on the sides of the channel (see schematics in Supplementary Section I), we also have

$$\frac{R(t)}{R(t=0)} = \left(\frac{h}{h-2b}\right)^4,$$

with b the thickness of the biofilm layer. The volume fraction of biofilm is $\phi = 1 - \left(\frac{h-2b}{h}\right)^2$ so that

$$\phi = 1 - \sqrt{\frac{R(t=0)}{R(t)}}.$$

To validate this approach, we performed correlation analysis between Φ calculated from hydraulic resistance and Φ estimated from integrated fluorescence intensity. Strong positive correlations (r = 0.68–0.77, p < 0.0001) were observed across all flow rates, confirming that pressure-based measurements accurately capture biofilm dynamics (Supplementary Figure S21).

Frequency analysis

Welch power spectral analysis Welch (1967) of the pressure signal was carried out by dividing the time signal into smaller segments, calculating their periodogram and finally averaging accross the frequencies, resulting in a power spectral density (PSD) estimate. This method allows for PSD estimate that is less noisy than usual periodograms. Here, we used the Matlab tool pwelch to estimate the PSD using hanning window with an overlap of 50%. A linear fit was then applied on the interval in the low frequency range.

Construction of the probability density functions for jumps and fits

Volume fraction data were processed using a homemade Matlab code. Each dataset was first subsampled by keeping only 1 in 150 points. The subsampled signal was then differentiated and only negative values corresponding to detachment events were conserved. Jumps were then identified through the selection of local minima. For each flow rate, all the values for the times between two successive jumps and the relative amplitude of the jumps – amplitude of the jump relative to the value of the volume fraction just before the jump – for the different replicates were aggregated to construct the distributions.

Gamma distributions were then fitted to the experimental data for the times between successive jumps and lognormal distributions were used for the amplitude of the jumps. Values for the different parameters are summarized in Table.2.

Numerical simulation of the stochastic process

Here we describe how we simulated the evolution of the volume fraction Φ, solving

$$d\phi_t = \phi_t \left(1 - \frac{1-\phi_{\max}}{1-\phi_t}\right) dt - \phi_{t^-} dN_t. \quad (10)$$

The simulation was done using a homemade Matlab code. For each case, based on the previously calculated distributions, we first generated two sets of random numbers corresponding to the times between successive jumps and to the relative amplitude of the jumps – therefore allowing us to completely determine the jump process, N. We then simply solved the ordinary differential equation

$$\dot{\phi} = \phi \left(1 - \frac{1-\phi_{\max}}{1-\phi}\right), \quad (11)$$

between jumps using the Matlab solve ode45. Upon reaching a jump, the simulation was stopped and the jump implemented, before proceeding to treating the next interval.

Comsol flow simulations

Flow simulation was performed using a finite element approach in Comsol v6.1. The channel was treated as a rectangle of 850 μm length by 100 μm width. Biofilm, as shown in white in Fig 6, was added from a segmentation of real experimental images. We then solved incompressible Stokes flow with no-slip/no-penetration boundary conditions on the solid and on the biofilm surface. The inlet condition was an imposed velocity, while the outlet was an imposed pressure.

Supplementary information

I. Models

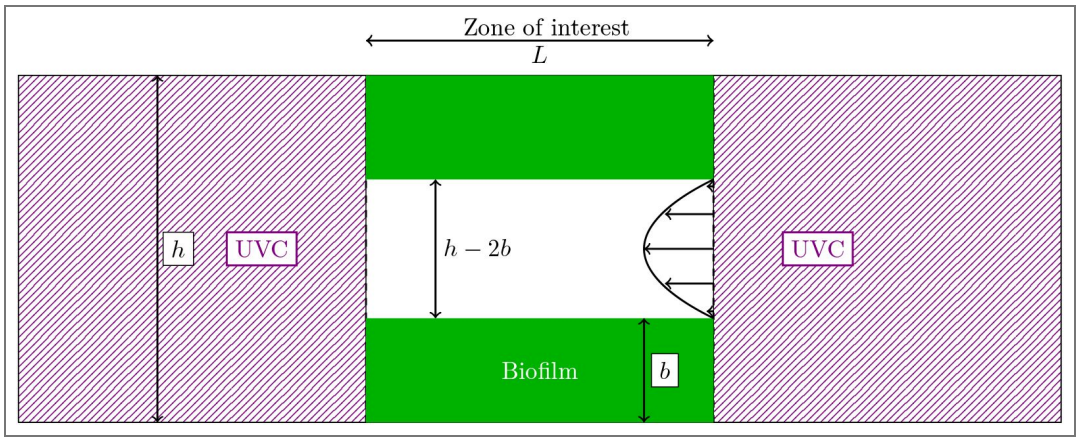

1. Nutrient transport

The limiting nutrient is treated as a solute being transported by advection/diffusion and consumed by bacteria. We consider a cross-section average concentration of the form $C = \int_{A(x)} c\,(x, y, z)\,dydz$ with A the section at any given x – x being the longitudinal direction. The transport reads

$$\partial_t C + \underbrace{V\partial_x C}_{\text{Advection}} = \underbrace{D\partial_{xx} C}_{\text{Diffusion}} - \underbrace{\phi\alpha \frac{C}{C+K}}_{\text{Nutrient uptake}}, \quad (1)$$

where C [$kg \times m^{-3}$] is the concentration, x is the longitudinal coordinate system, Φ is the cross-section volume fraction of biofilm, V [$m \times s^{-1}$] the average velocity in the empty channel, $D = 10^{-9} m^2 \times s^{-1}$ an estimate diffusion coefficient of the solute, α [$kg \times m^{-3} \times s^{-1}$] the uptake rate and K [$kg \times m^{-3}$] the half-saturation constant. As we impose a constant flow rate for each experiment, the

velocity averaged over the entire cross-section remains constant, even for different values of Φ. The term Φ in the nutrient uptake indicates that consumption is proportional to the volume fraction of biofilm.

We considered that nutrient transport is quasi-steady, since solute transport is much faster than growth. We further nondimensionalized this equation as

$$Pe\partial_x C^\star = \partial_{xx} C^\star - Da\phi \frac{C^\star}{C^\star + K^\star} \quad (2)$$

with $C^\star = \frac{C}{C_0}$ with the inlet concentration C_0 [$kg \times m^{-3}$] the length of the channel L = 10 mm, the Péclet number $Pe = \frac{VL}{D}$ and Da the Damköhler number defined as the ratio of diffusive to reactive times, $Da = \frac{\alpha L^2}{C_0 D}$.

2. Flow

We treat the biofilm as a uniform layer on the solid surface, so that the flow channel always has a square cross-section. We also neglect biofilm porosity at this scale and consider a no-slip boundary condition at the boundary with the fluid. Porosity is a component of biofilm structures, resulting from the polymeric nature of the EPS matrix, mechanical forces, and biological processes such as cell death or predation. When considering flow-biofilm interactions, this porosity may allow fluid flow through the biofilm, with reported permeability values spanning an extremely broad range from 10^{-15} to 10^{-7} (Kurz et al., 2023). However, we argue that biofilm permeability is not the primary driver in our system:

- In microscopy visualization, our biofilms form dense structures where flow around the biofilm through narrow channels dominates over flow through the porous biofilm matrix.
- We performed microrheology experiments (data not shown) in these biofilms by imaging the Brownian motion of nanoparticles in the biofilm. Their trajectories indicate that, in our conditions, the viscoelastic flow of the biofilm itself largely dominates over the flow of culture medium through the biofilm matrix.
- We argue that the extreme variability in reported permeability values (spanning several orders of magnitude, Kurz et al., 2023) reflects not only differences in experimental systems, but also fundamental challenges in defining and measuring permeability for viscoelastoplastic biofilms (the biofilm itself is actually flowing). Given this uncertainty, incorporating permeability into our model would introduce parameters that cannot be reliably constrained from literature or independently measured in our setup. Our approach (i.e. treating the biofilm as impermeable and focusing on flow obstruction) avoids this parametrization complexity while successfully capturing the observed dynamics.
- Our model successfully predicts the observed scaling laws (main text Fig. 7f) and hydraulic resistance dynamics (main text Fig. 3) without invoking permeability, suggesting that flow obstruction rather than flow penetration is the dominant mechanism.

With these hypotheses, we write the pressure drop across the channel as

$$\Delta P = R(\phi)\, Q, \quad (3)$$

with ΔP the pressure difference, Q the flowrate and R the hydraulic resistance (which is a function of the volume fraction of biofilm). The hydraulic resistance in the empty channel is

$$R_0 = A\frac{\mu L}{h^4} \quad (4)$$

With $A = \frac{12}{1-\sum_{n,\text{odd}}^{\infty} \frac{1}{n^5} \frac{192}{\pi^5} \tanh\left(n\frac{\pi}{2}\right)}$ – which can be approximated as $R_0 = \frac{12\mu L}{h^4[1-0.917\times 0.63]}$ with $A \simeq \frac{12}{1-0.917\times 0.63}$. When the biofilm grows as a uniform layer, we also have

$$R = A\frac{\mu L}{(h-2b)^4} \quad (5)$$

To obtain an expression in terms of the volume fraction of biofilm, we use $\phi = 1-\left(1-2\frac{b}{h}\right)^2$ and $b = h\frac{1-\sqrt{1-\phi}}{2}$ – and also $h - 2b = h\,(1-\Phi)^{1/2}$. We thus have

$$\boxed{\frac{R}{R_0} = \frac{1}{(1-\phi)^2}.} \tag{6}$$

3. Hydrodynamic stresses

We first write σ_0 the shear stress on the liquid/solid surface of the channel when $\Phi = 0$. To obtain an explicit expression for this stress, the easiest way to proceed is to notice that, in the x direction, tangential to the surface of the channel, the force exerted by the pressure difference between the inlet and outlet is equal to the viscous force exerted by the fluid on the solid. This can be easily shown by integrating $\nabla \cdot \boldsymbol{\sigma} = 0$, with $\boldsymbol{\sigma} = -p\mathbf{I} + \mu\,\nabla\mathbf{v} +^{\mathrm{T}} \nabla\mathbf{v}$ and p the pressure and μ the viscosity, over a control volume that is the the zone of interest between UVCs in the channel. With $4hL$ the solid surface in the zone of interest, we have $\sigma_0 4hL = h^2\Delta P$ where L is the length of the control volume, h is the width of the square channel and ΔP is the pressure difference between inlet and outlet. We therefore have

$$\sigma_0 = \frac{h\Delta P}{4L}. \tag{7}$$

We can also write $\Delta P = R_0 Q$ with the hydraulic resistance in the square cross-section channel, $R_0 = A\frac{\mu L}{h^4}$. Therefore, we have

$$\sigma_0 = \frac{A}{4}\frac{\mu Q}{h^3}. \tag{8}$$

With the same type of reasoning, the total force along x applied by the fluid on the biofilm, including both shear and pressure is $h^2\Delta P = A\frac{\mu LQ}{h^2(1-\phi)^2}$. Therefore, the total stress on the biofilm solid surface is

$$\frac{\sigma}{\sigma_0} = \frac{1}{(1-\phi)^2}, \tag{9}$$

with a contribution from pressure

$$\frac{\sigma_{\text{pressure}}}{\sigma_0} = \frac{\phi}{(1-\phi)^2}, \tag{10}$$

and from shear

$$\frac{\sigma_{\text{shear}}}{\sigma_0} = \frac{1-\phi}{(1-\phi)^2}. \tag{11}$$

Also note that the shear stress at the biofilm fluid interface is

$$\frac{\tau_{\text{shear}}}{\sigma_0} = \frac{1}{(1-\phi)^{3/2}}, \tag{12}$$

with the difference being simply the ratio of biofilm/solid and biofilm/fluid surfaces.

4. Biofilm growth

We model biofilm development as

$$\partial_t\phi = \phi\left(\frac{Y\alpha}{X}\frac{C}{C+K} - \chi\sqrt{\sigma}\right) \tag{13}$$

with Y a yield coefficient (mass of biofilm produced by mass of limiting nutrient consumed), X the density of the biofilm X [$kg \times m^{-3}$] and χ the sensitivity to biofilm detachment $\chi\ \left[\sqrt{kg^{-1}\times m}\right]$. We non-dimensionalize with time $\tau = \frac{X}{Y\alpha}(1+K^\star)$ in order to obtain

$$\partial_t\phi = \phi\left[\frac{C^\star(1+K^\star)}{C^\star+K^\star} - \frac{X}{Y\alpha}(1+K^\star)\chi\sqrt{\sigma_0}\sqrt{\frac{\sigma}{\sigma_0}}\right]. \tag{14}$$

Recalling that $\sqrt{\frac{\sigma}{\sigma_0}} = (1-\phi)^{-1}$ and writing the dimensionless number $\mathcal{M} = \frac{X}{Y\alpha}(1+K^\star)\chi\sqrt{\sigma_0}$, we obtain

$$\partial_t\phi = \phi\left[\frac{C^\star(1+K^\star)}{C^\star+K^\star} - \frac{\mathcal{M}}{1-\phi}\right]. \tag{15}$$

Assuming that $\mathcal{M} \leq 1$, which is consistent with the observation that biofilm is never completely removed from the channels, we can also write this as

$$\partial_t \phi = \phi \left[\frac{C^\star (1 + K^\star)}{C^\star + K^\star} - \frac{1 - \phi_{\max}}{1 - \phi} \right] \tag{16}$$

with $\Phi_{\max}$ the maximum value of Φ.

In the case with no nutrient limitation, we assume $C^\star = 1$ everywhere in the channel, so that we have

$$\dot{\phi} = \phi \left(1 - \frac{1 - \phi_{\max}}{1 - \phi} \right), \tag{17}$$

with Φ describing an average volume fraction in the entire channel, and thus being only a function of time. We can also describe sloughing by modifying this equation as

$$d\phi_t = \phi_t \left(1 - \frac{1 - \phi_{\max}}{1 - \phi_t} \right) dt - \phi_{t^-} dN_t, \tag{18}$$

with Φ_t describing the average fraction of biofilm in the microchannel, N the jumps and ϕ_{t^-} the value of Φ at time t^- just before the jump.

II. Supplementary figures

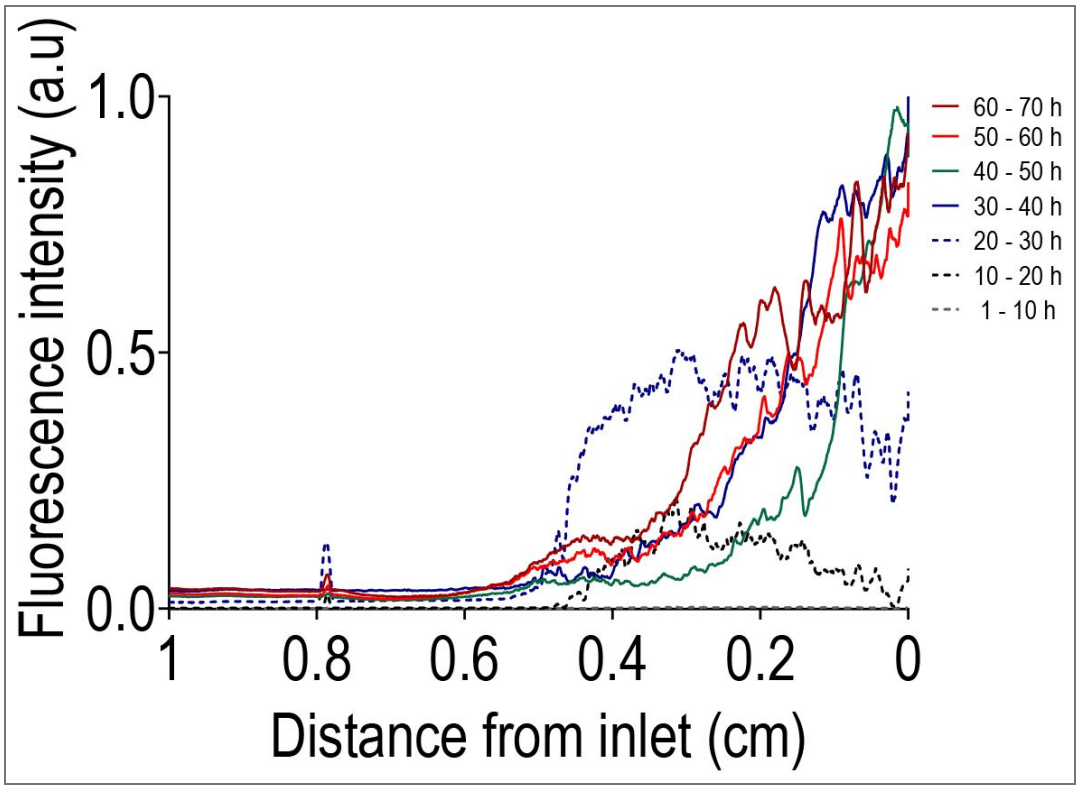

Figure S1. **Time evolution (10 hours by curve) for Q = 0.02 *μL/min* of the averaged (n = 3) longitudinal distribution of the biofilm and the impact of nutrient limitation.**

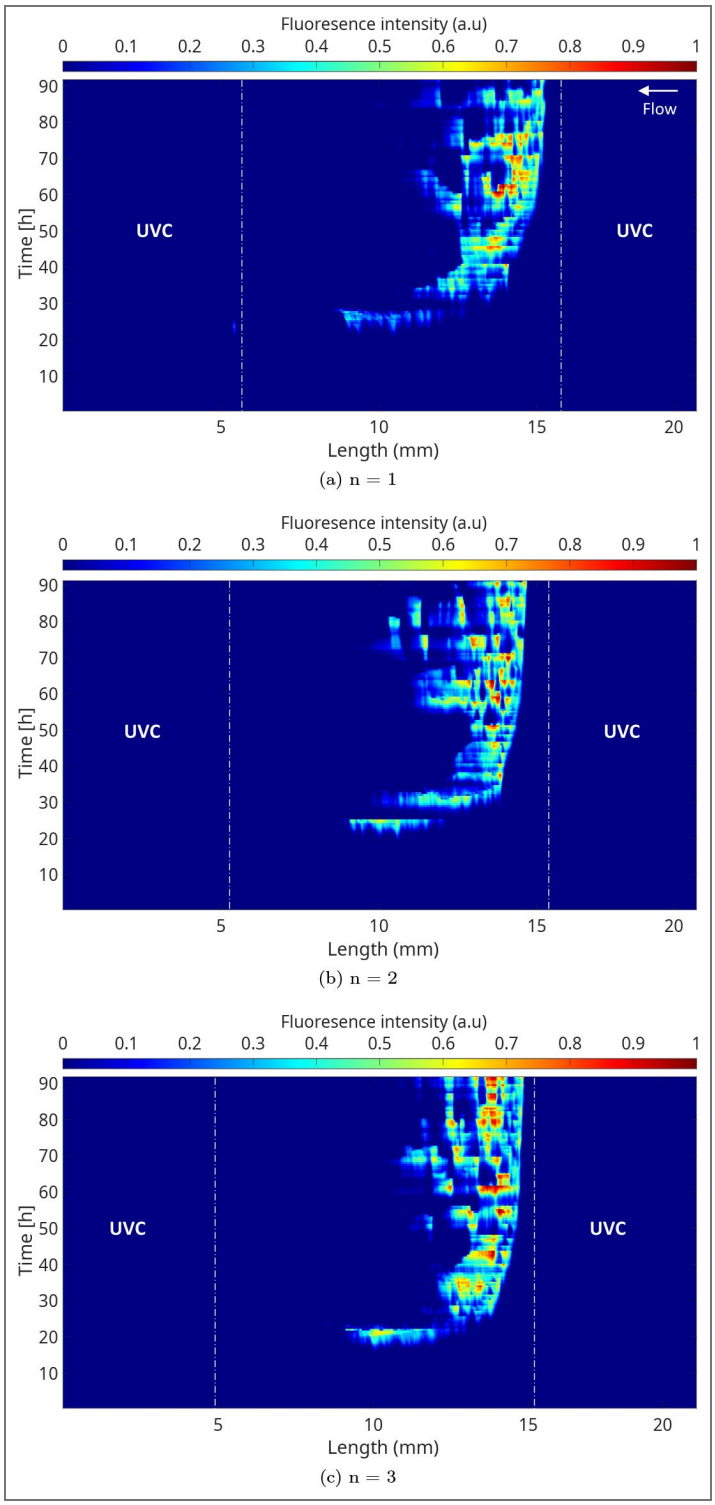

Figure S2. Kymograph representations based on the GFP signal for *Q* = 0.02 *µL/min* with [1X] BHI showing the spatio-temporal dynamics of the biofilm longitudinal distribution.

Fluorescence intensity signal was normalized to the maximum signal intensity value.

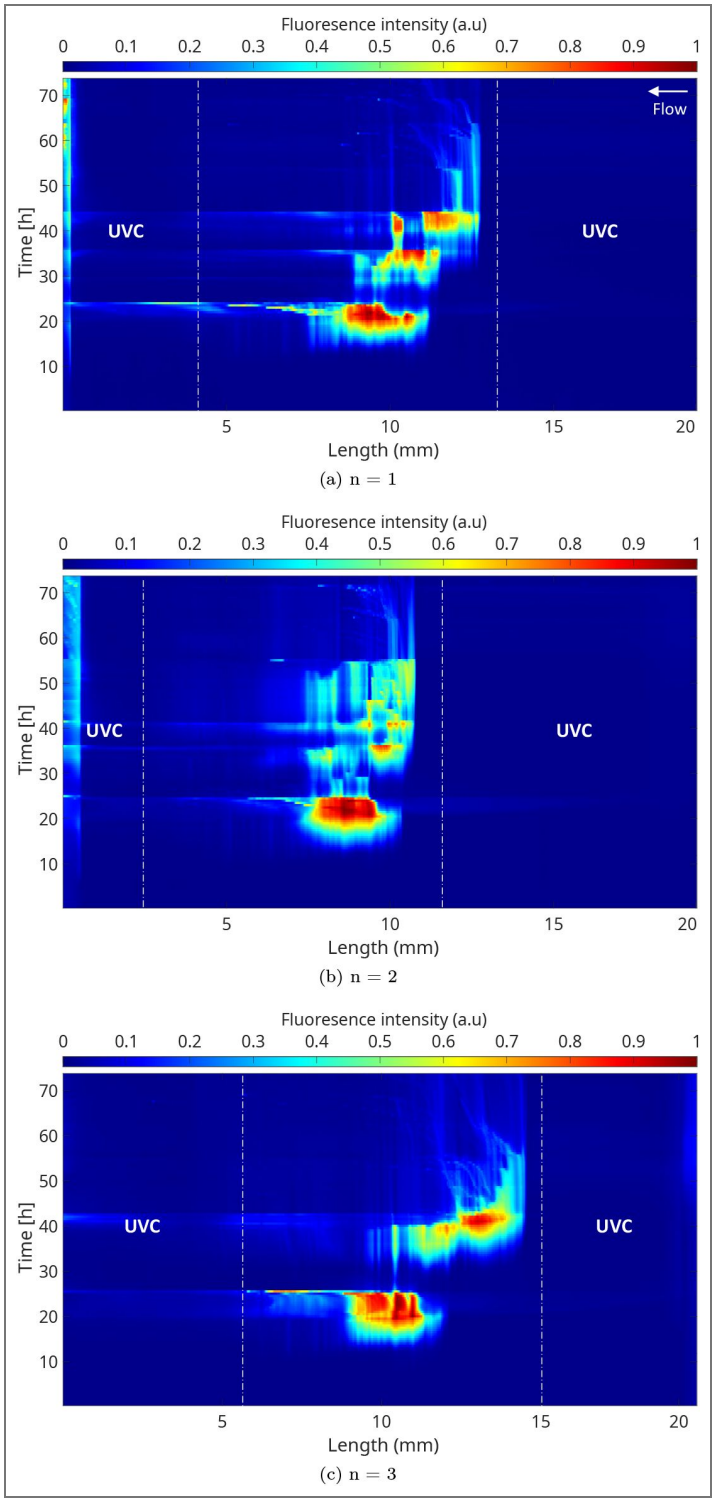

Figure S3. Kymograph representation for *Q* = 0.02 *µL/min* with [1X] BHI supplemented by 8 *g/L* glucose.

Fluorescence intensity signal was normalized to the maximum signal intensity value.

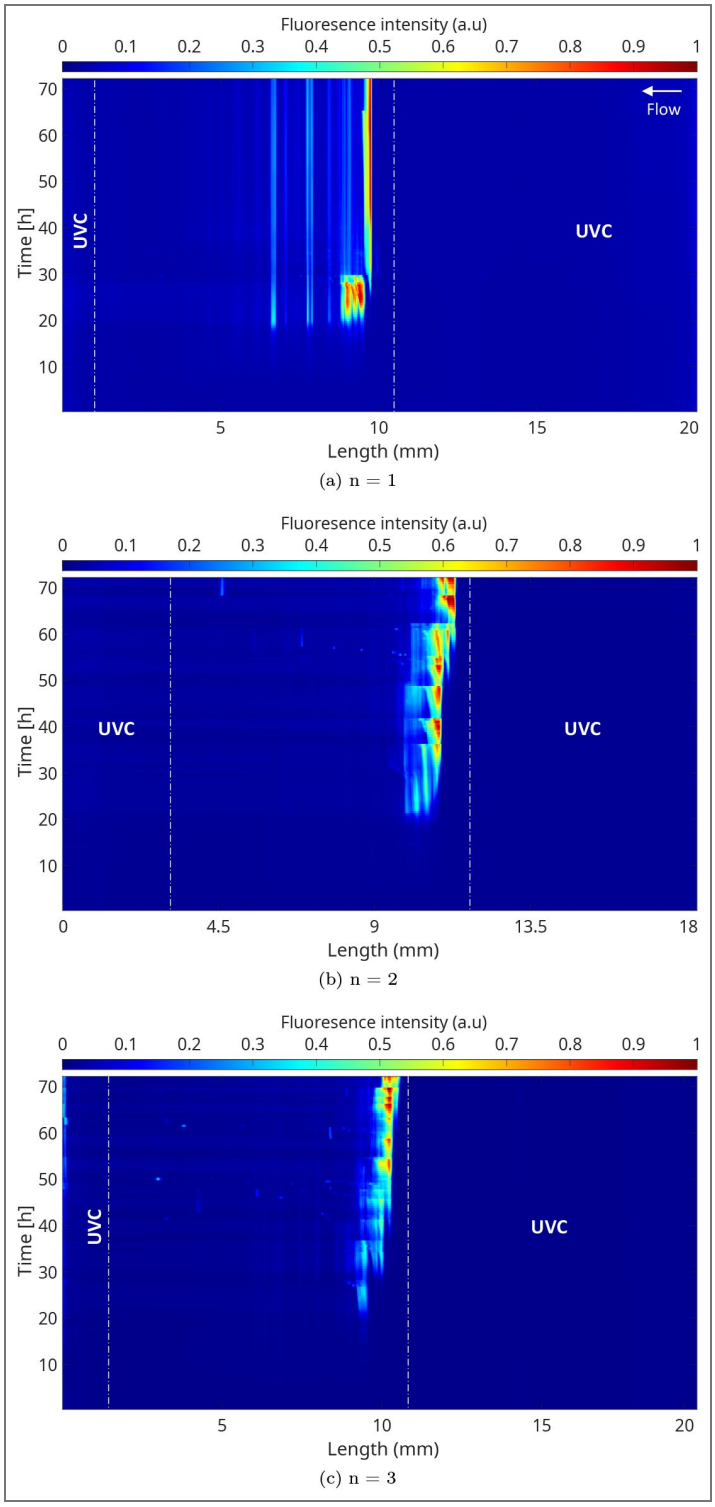

Figure S4. Kymograph representation for *Q* = 0.02 *µL/min* with [0.2X] BHI.

Fluorescence intensity signal was normalized to the maximum signal intensity value.

Figure S5. Temporal dynamics of growth and detachment for *Q* = 0.2 *μL/min*.

(a), (b) and (c) show the variation of hydraulic resistance (black line) for three replicates, along with the percentage of colonization extracted from image segmentation (red line) and the integrated fluorescence intensity signal (green). Thin dotted lines on the top of y axis indicate the maximum value reached by hydraulic resistance. (d), (e) and (f): corresponding wavelet scalograms for the pressure signal.

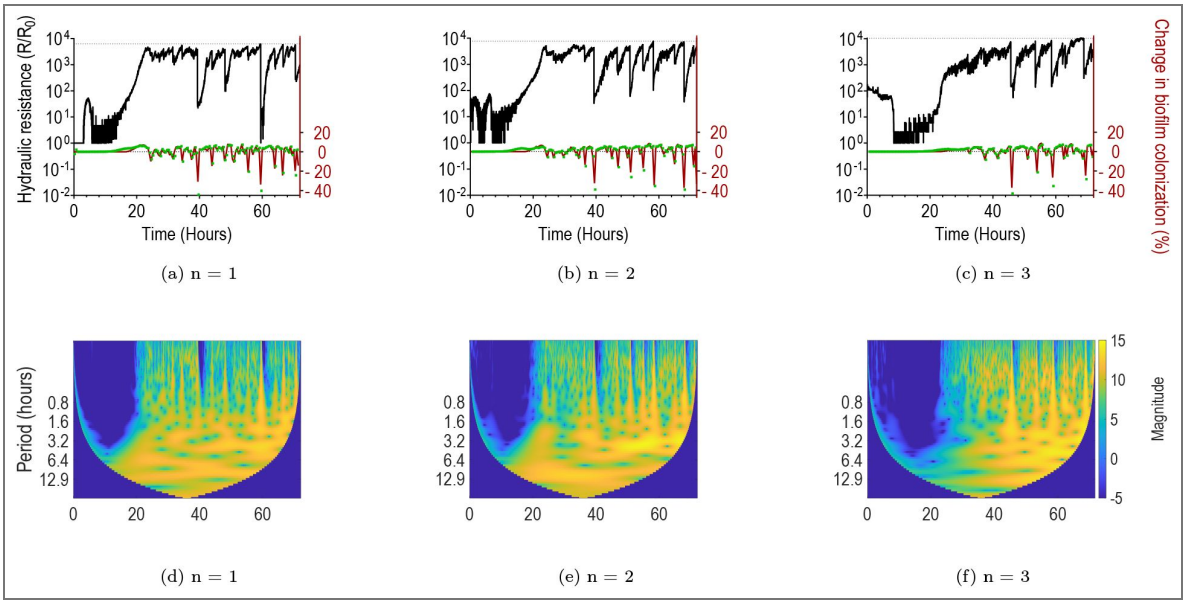

Figure S6. Temporal dynamics of growth and detachment for *Q* = 0.2 *μL/min*.

(a), (b) and (c) show the evolution of the volume fraction as a function of time, with that calculated from hydraulic resistance (black line) and from segmentation (green dotted line). (d), (e) and (f): normalized integrated fluorescence intensity signal as a function of time.

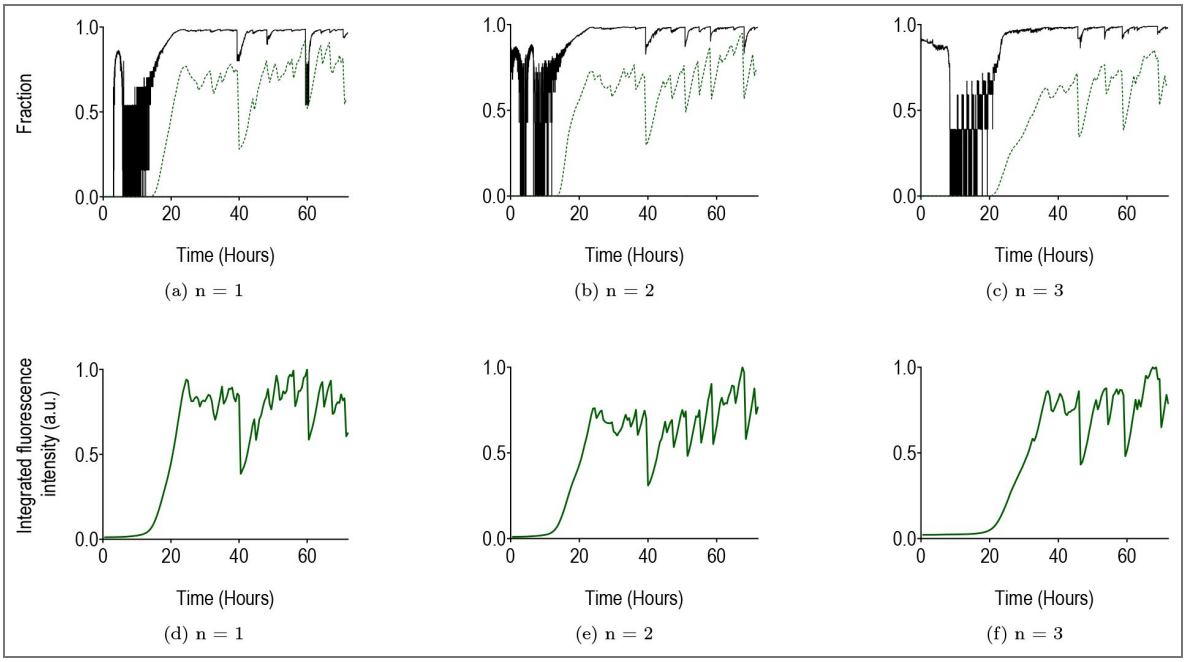

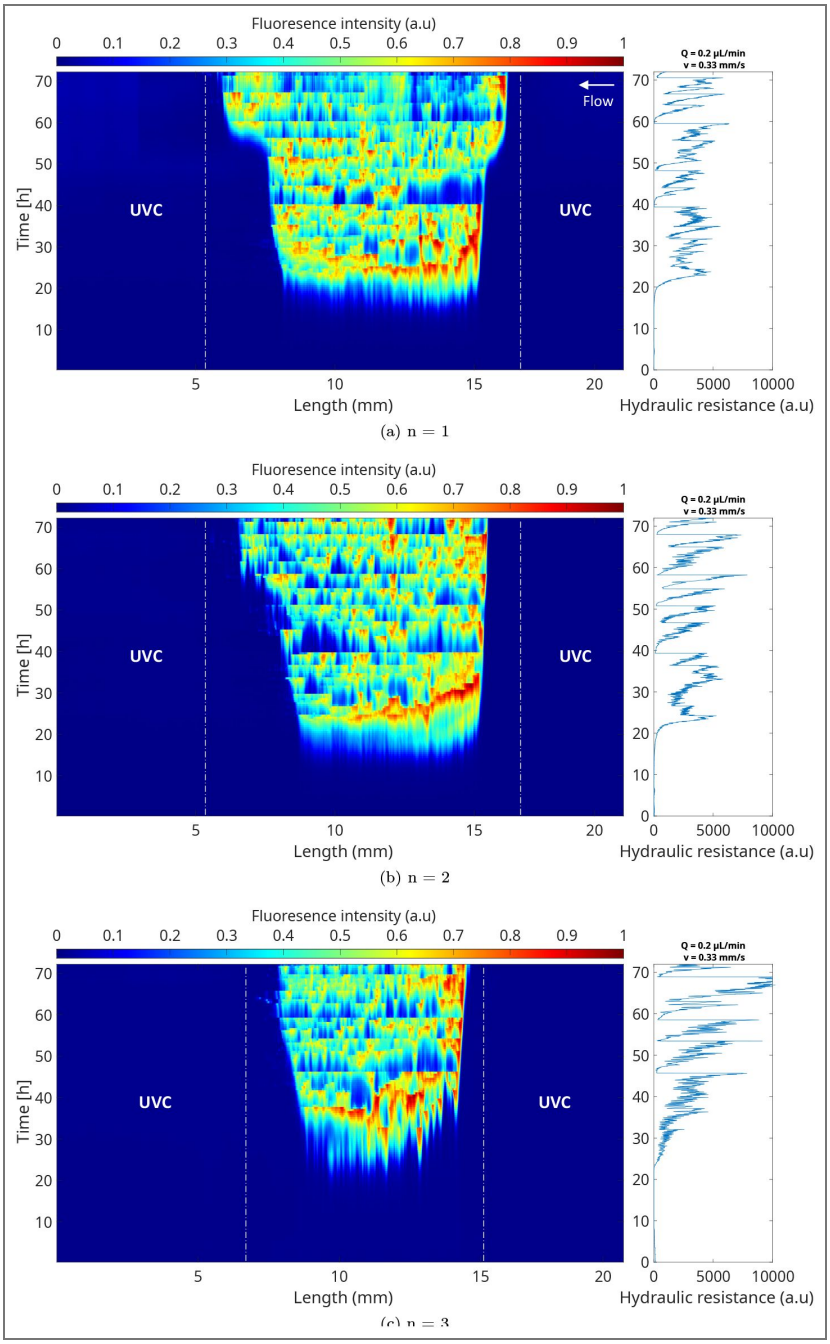

Figure S7. Kymograph representation for *Q* = 0.2 *µL/min* with [1X] BHI.

Fluorescence intensity signal was normalized to the maximum signal intensity value. Plots on the right show the corresponding evolution of the hydraulic resistance.

Figure S8. Temporal dynamics of growth and detachment for Q = 2 $\mu L/min$.

(a), (b) and (c) show the variation of hydraulic resistance (black line) for three replicates, along with the percentage of colonization extracted from image segmentation (red line) and the integrated fluorescence intensity signal (green). Thin dotted lines on the top of y axis indicate the maximum value reached by hydraulic resistance. (d), (e) and (f): corresponding wavelet scalograms for the pressure signal.

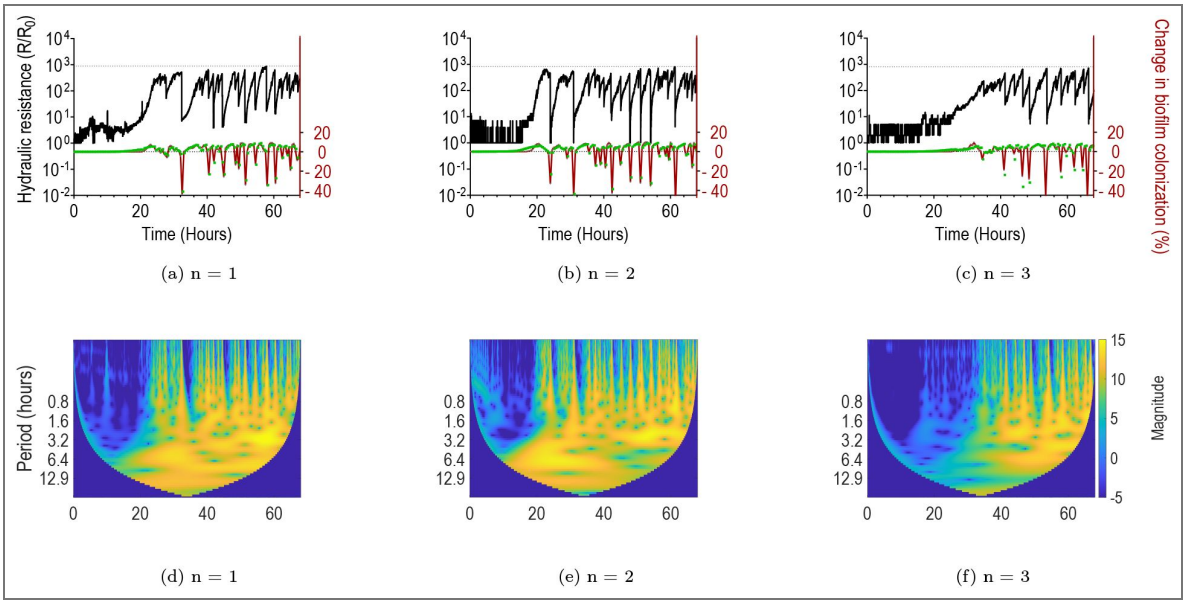

Figure S9. Temporal dynamics of growth and detachment for Q = 2 $\mu L/min$.

(a), (b) and (c) show the evolution of the volume fraction as a function of time, with that calculated from hydraulic resistance (black line) and from segmentation (green dotted line). (d), (e) and (f): normalized integrated fluorescence intensity signal as a function of time.

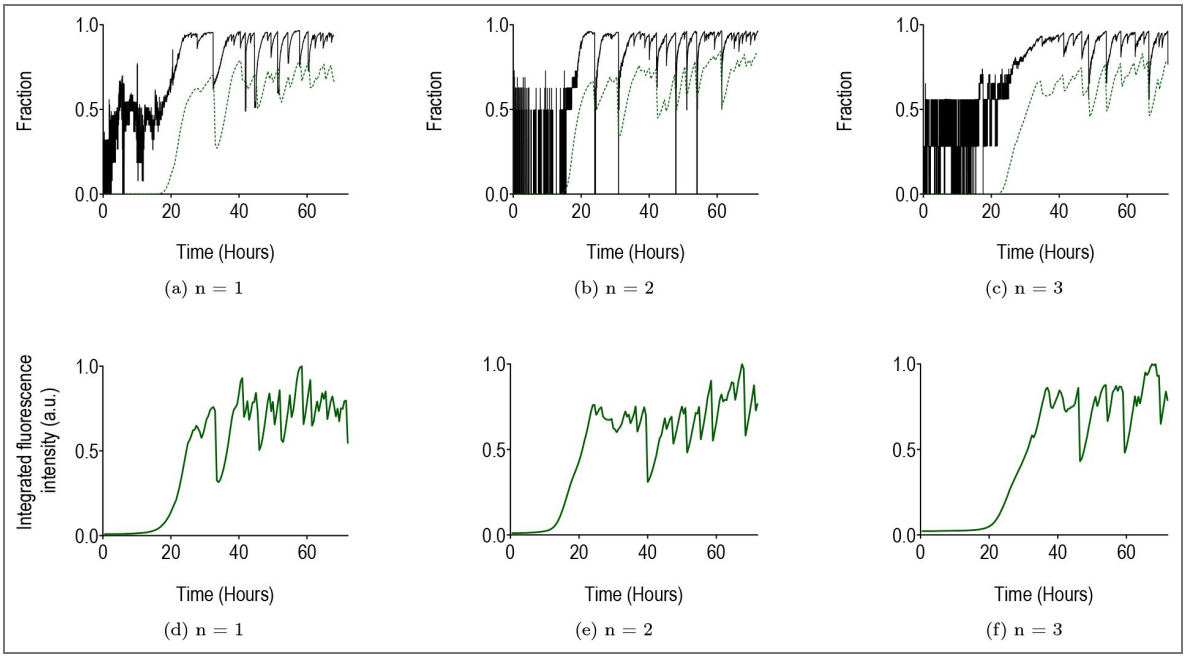

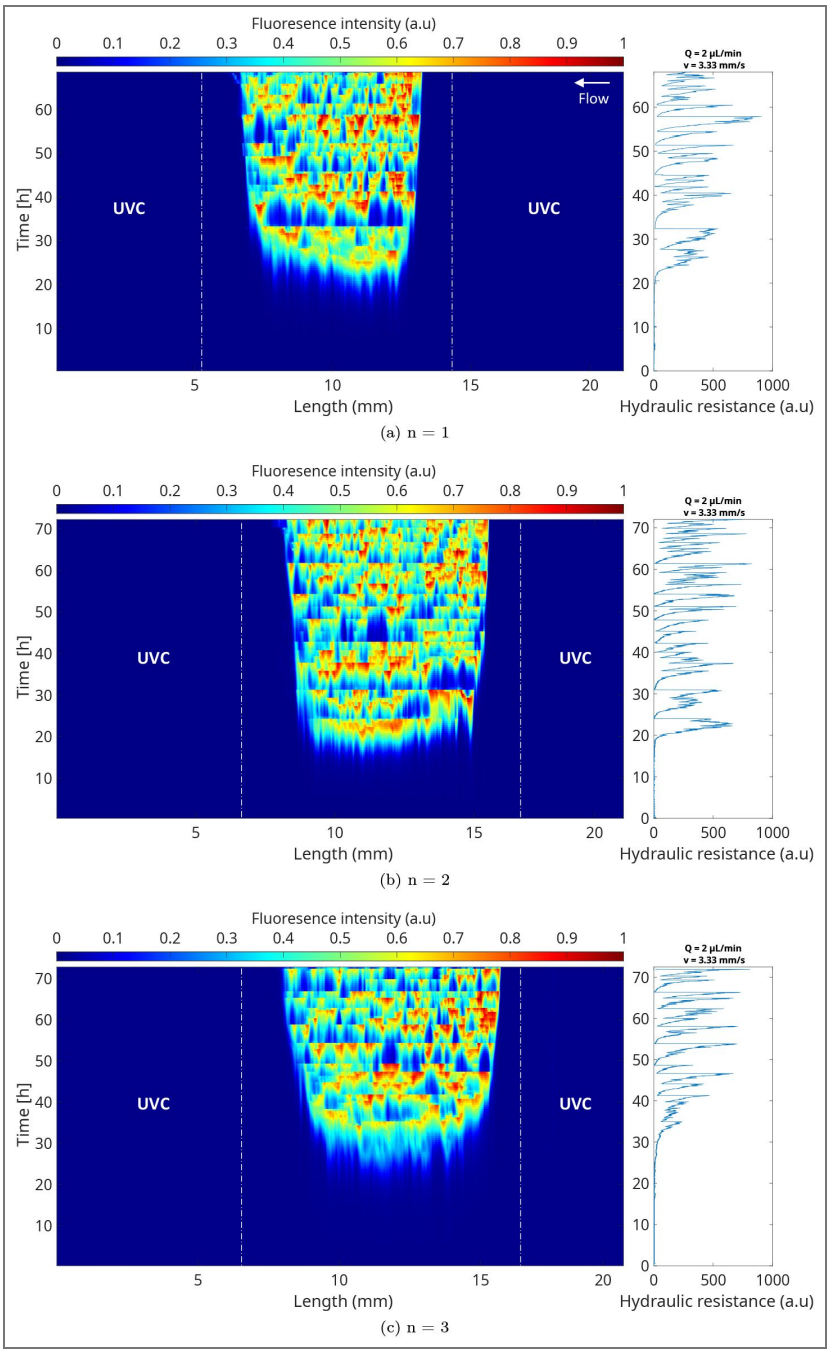

Figure S10. Kymograph representation for *Q* = 2 *µL/min* with [1X] BHI.

Fluorescence intensity signal was normalized to the maximum signal intensity value. Plots on the right show the corresponding evolution of the hydraulic resistance.

Figure S11. Temporal dynamics of growth and detachment for Q = 20 $\mu L/min$.

(a), (b) and (c) show the variation of hydraulic resistance (black line) for three replicates, along with the percentage of colonization extracted from image segmentation (red line) and the integrated fluorescence intensity signal (green). Thin dotted lines on the top of y axis indicate the maximum value reached by hydraulic resistance. (d), (e) and (f): corresponding wavelet scalograms for the pressure signal.

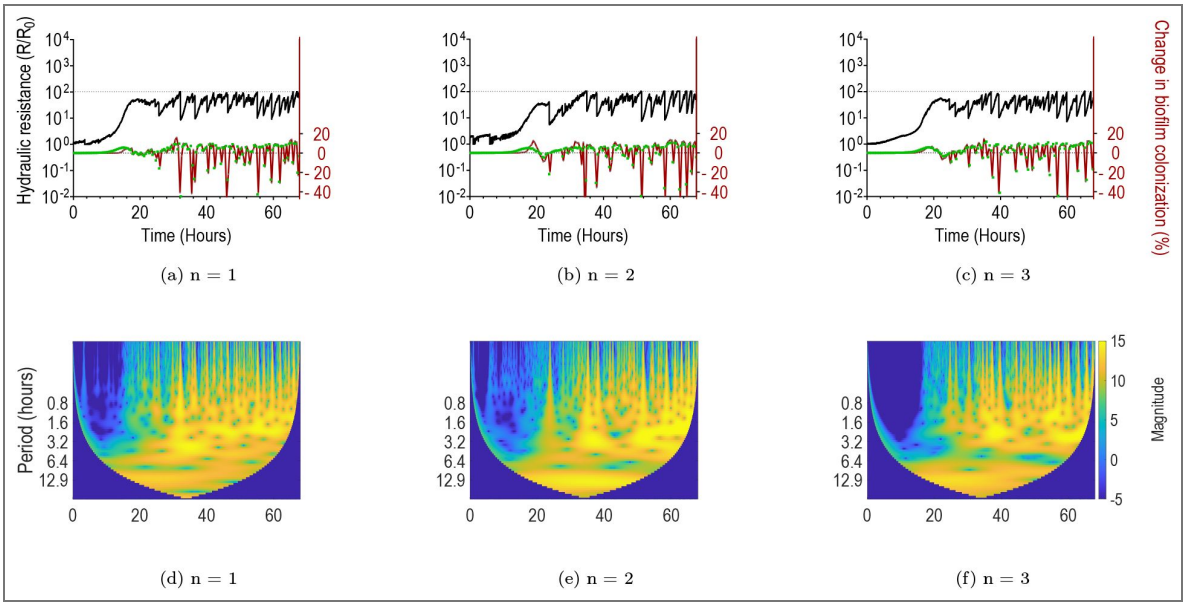

Figure S12. Temporal dynamics of growth and detachment for Q = 20 $\mu L/min$.

(a), (b) and (c) show the evolution of the volume fraction as a function of time, with that calculated from hydraulic resistance (black line) and from segmentation (green dotted line). (d), (e) and (f): normalized integrated fluorescence intensity signal as a function of time.

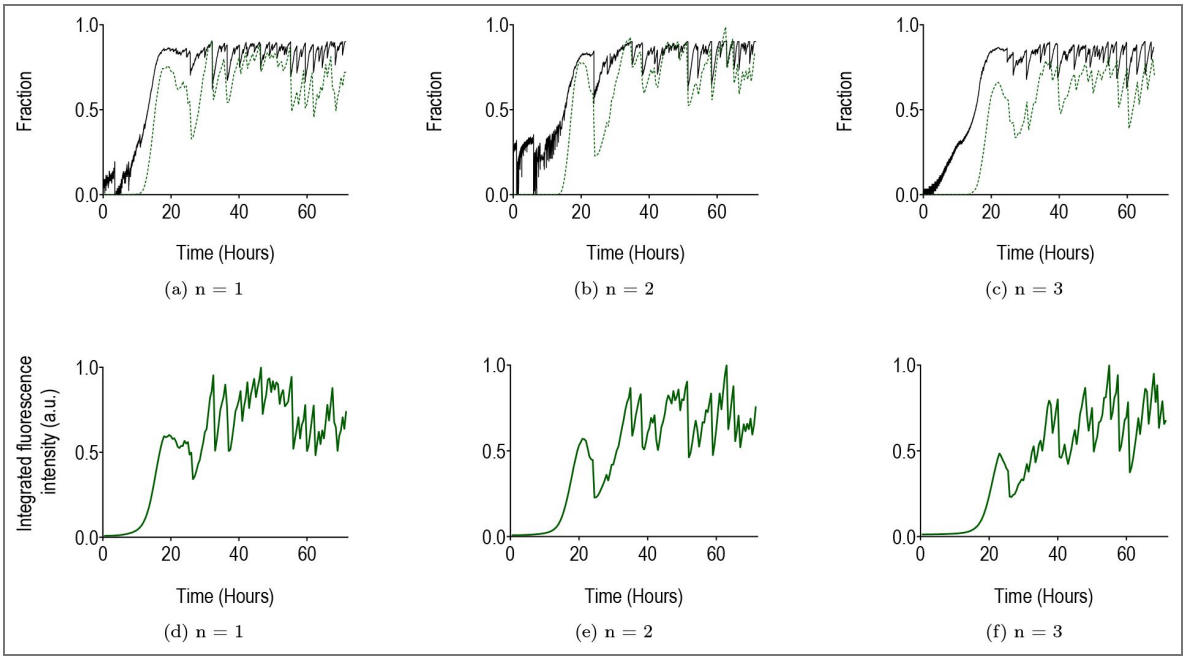

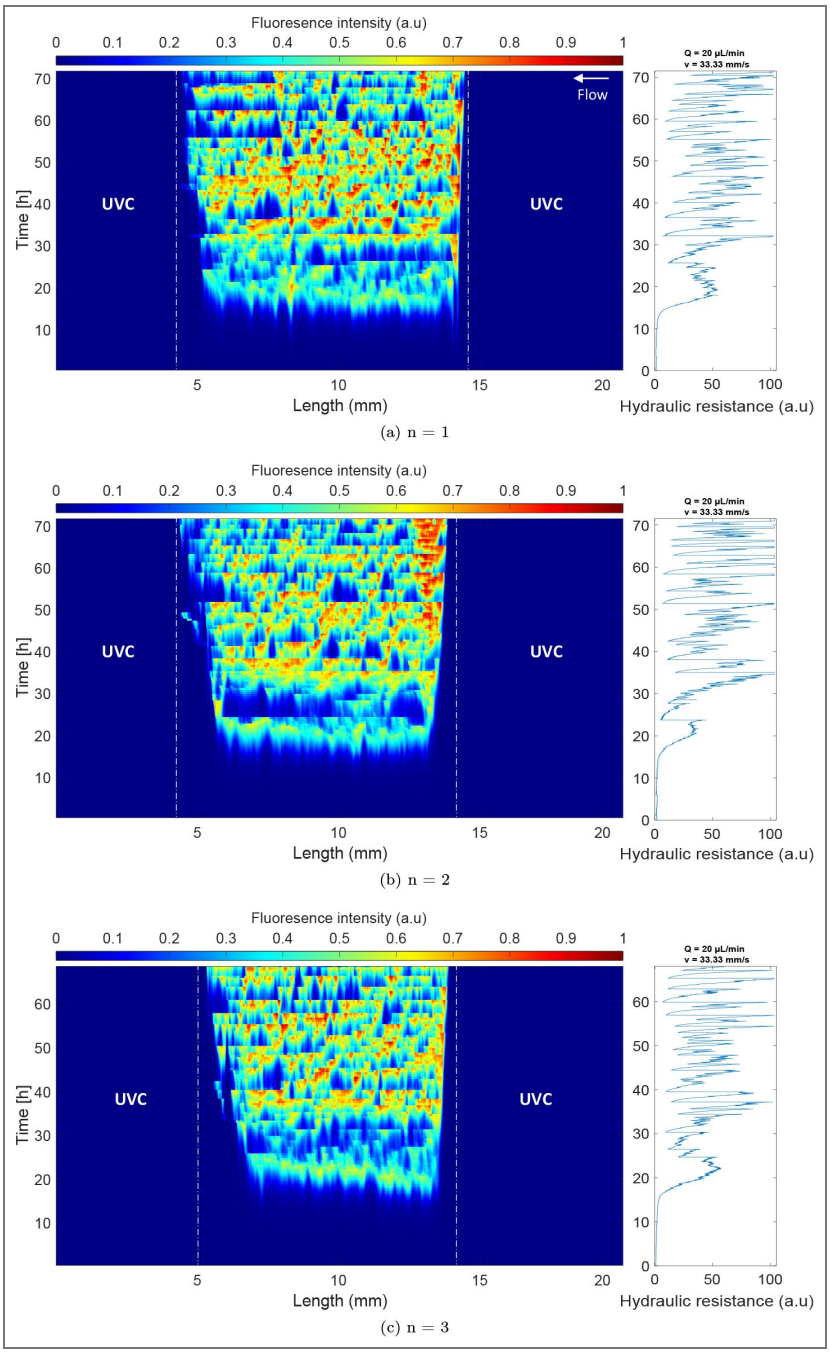

Figure S13. Kymograph representation for *Q* = 20 *µL/min* with [1X] BHI.

Fluorescence intensity signal was normalized to the maximum signal intensity value. Plots on the right show the corresponding evolution of the hydraulic resistance.

Figure S14. Temporal dynamics for *Q* = 200 *μL/min*.

(a) evolution of the hydraulic resistance (black solid line) in time, calculated from pressure fluctuations. It also shows changes in biofilm colonization extracted from either integrated fluorescence intensity (green squares) or image segmentation (red solid line). (b): Fraction of biofilm in the microchannel, either calculated from hydraulic resistance (black solid line) or estimated from integrated GFP intensity (green dotted line), for the different flow rates.

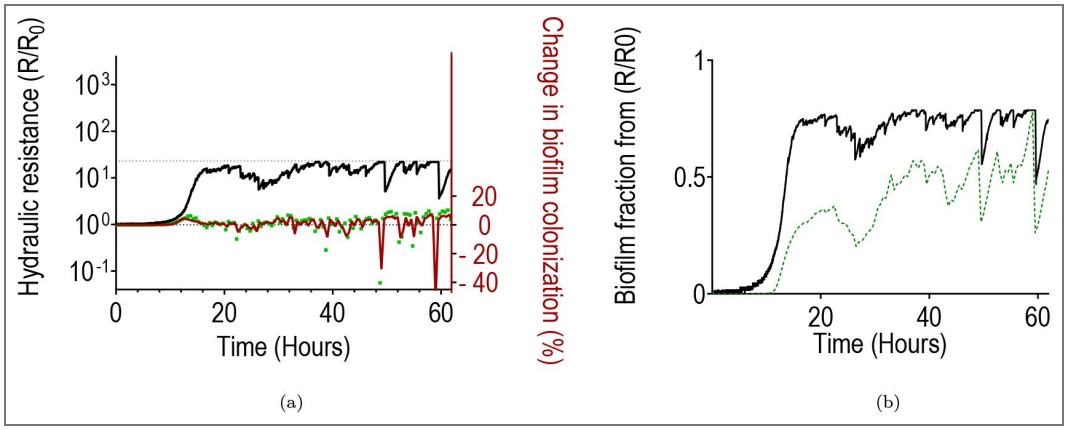

Figure S15. Temporal dynamics of growth and detachment for Δ*pslD* strain with *Q* = 0.2 *μL/min*.

(a), (b) and (c): volume fraction calculated from image segmentation for three replicates.

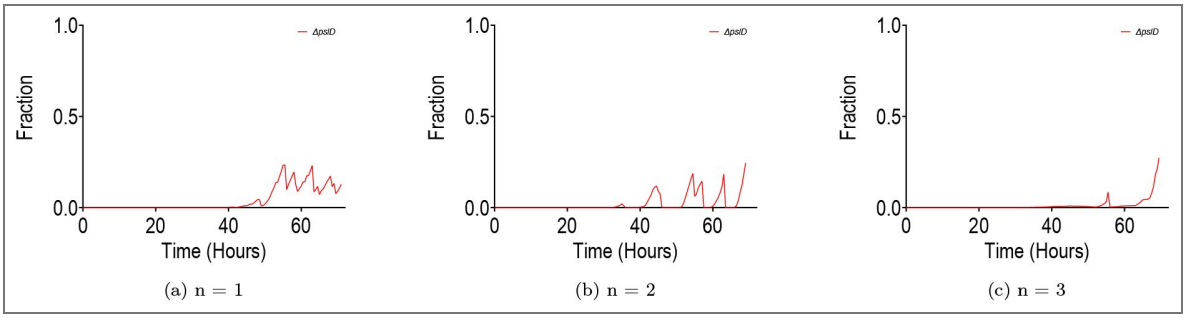

Figure S16. Temporal dynamics of growth and detachment for Δ*pslD* strain with *Q* = 2 *μL/min*.

(a), (b) and (c): volume fraction calculated from image segmentation for three replicates.

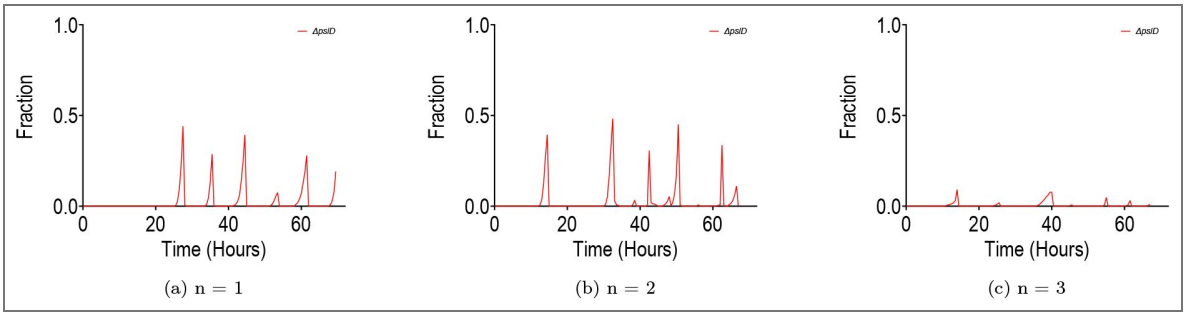

Figure S17. Temporal dynamics of growth and detachment for Δ*pelF* strain with *Q* = 0.2 *μL/min*.

(a), (b) and (c): volume fraction calculated from image segmentation for three replicates.

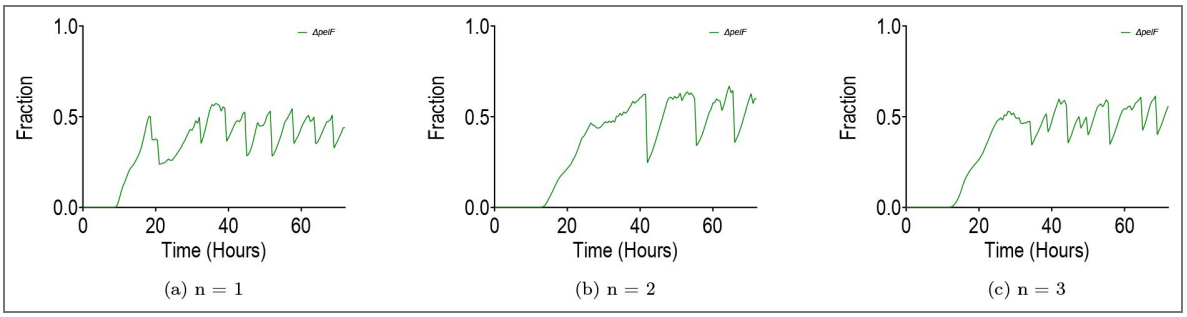

Figure S18. Temporal dynamics of growth and detachment for Δ*pelF* strain with *Q* = 2 *μL/min*.

(a), (b) and (c): volume fraction calculated from image segmentation for two replicates.

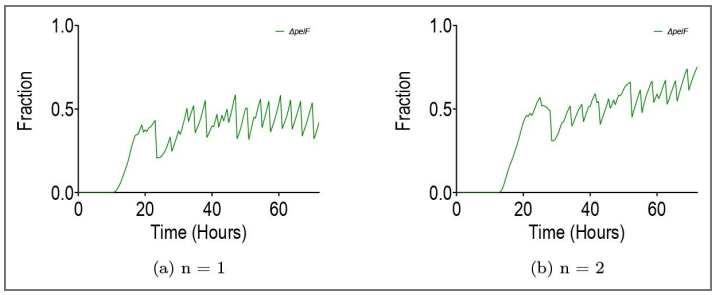

Figure S19. Log-log plot of $\dot{\gamma}_0$ as a function of the flow rate (*Q* = 0.2 *μL/min*, 2 *μL/min*, 20 *μL/min* and 200 *μL/min*).

The red dotted line simply shows the slope for an evolution with the inverse of the flow rate Q^{-1}. Error bars represent standard deviation for n = 3 replicates, except for *Q* = 200 *μL/min*, for which n = 1.

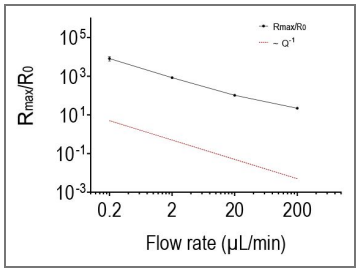

Figure S20. Quantile-quantile (Q-Q) plots of inter-event times fitted with Gamma distributions at three flow rates: *Q* = 0.2 *µL/min*, 2 *µL/min*, 20 *µL/min*.

Sample quantiles (y-axis) are plotted against theoretical Gamma quantiles (x-axis). Close alignment with the diagonal reference line (red) indicates that the Gamma distribution provides a reasonable approximation of the overall distributional behavior.

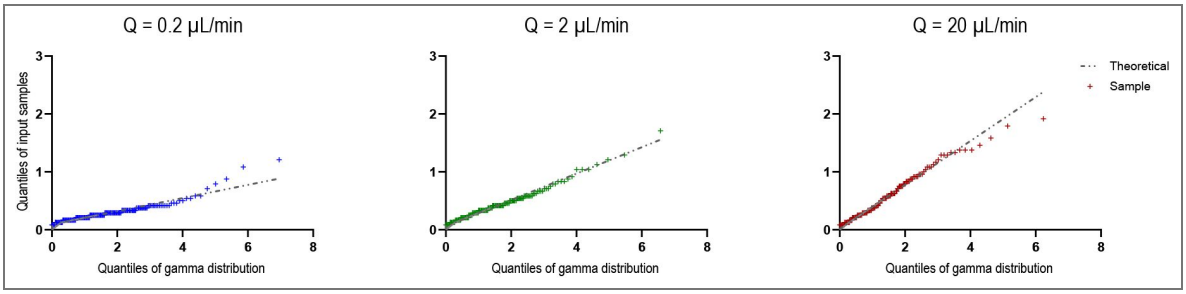

Figure S21. Pearson's correlation between volume fractions obtained from image segmentation and calculated from hydraulic resistance for flow rates *Q* = 0.2 *µL/min*, 2 *µL/min*, 20 *µL/min* and 200 *µL/min*.

To account for acquisition frequency mismatch, hydraulic resistance data were downsampled from 1 Hz to 1 point per 30 minutes. Each point represents one paired measurement. Data from all replicates were pooled for each condition (sample size n indicated on each plot). Red lines show linear regression fits: r = 0.68, 0.76, 0.72, 0.77 (mean across the 3 replicates) for *Q* = 0.2 *µL/min*, 2 *µL/min*, 20 *µL/min*, 200 *µL/min* respectively; p < 0.0001 for all conditions.

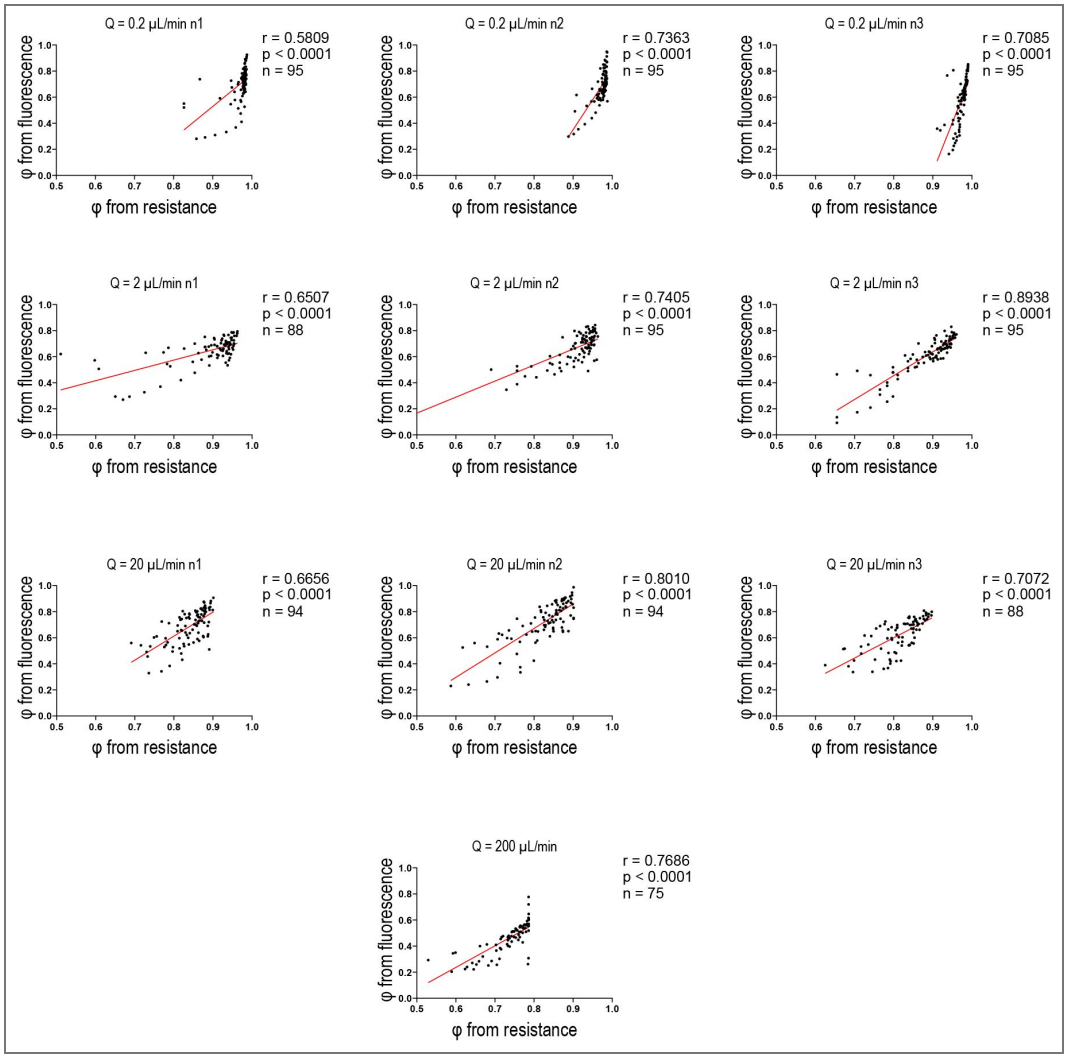

Strain	WT PAO1 ATCC 15692:GFP	WT PAO1 pMRP9-1:GFP	Δ*pel* PAO1 pMRP9-1 :GFP	Δ*psl* PAO1 pMRP9-1 :GFP
Lag phase duration (minutes)	233 +/- 3,00	275 +/- 8,33	424 +/- 16,30	377 +/- 40,17
Doubling time (minutes)	105 +/- 3,81	108 +/- 8,45	134 +/- 17,11	135 +/- 9,83

Table S1. Lag phase and doubling time in minutes for *P. aeruginosa* WT PAO1 and EPS defective strains.

Mean values were obtained from 3 replicates for each strain and +/− indicates the standard deviation.

Data availability

Data generated or analyzed during this study are in the manuscript and supporting files. Source data is available upon request.

Acknowledgements

This work is part of a project that has received funding from the European Research Council (ERC) under the European Union's Horizon 2020 research and innovation programme (grant agreement no 803074). This work was partially supported by the LAAS-CNRS micro and nanotechnologies platform, a member of the French Renatech network. We thank the entire BEBOP team for daily interactions and assistance; Julien Lefort and Emmanuel Libert for their technical support; Terence Desclaux for the introduction to wavelet analysis; Matthew R. Parsek and Maria Zori for providing the Pel and Psl mutants; and Laure Latapie for her support with mass spectrometry.

Additional files

Video 1 DIC timelapse of the initial development at 0.2 *μL/min*.

Video 2 DIC timelapse of the initial development at 2 *μL/min*.

Video 3 DIC timelapse of the initial development at 20 *μL/min*.

Video 4 composite (GFP and brightfield) timelapse of biofilm development at 20 *μL/min*.

Additional information

Funding

Funder	Grant reference number	Author
EC | European Research Council (ERC)	https://doi.org/10.3030/803074	Massinissa Benbelkacem Yara Abidine Yohan Davit Fatima El Garah Gabriel Ramos Christine Roques

Author ORCID iDs

Yohan Davit: https://orcid.org/0000-0002-2234-9567

References

Alvarez-Ortega C, Harwood CS (2007) Responses of Pseudomonas Aeruginosa to Low Oxygen Indicate That Growth in the Cystic Fibrosis Lung Is by Aerobic Respiration. *Molecular microbiology* **65**:153-165 https://doi.org/10.1111/j.1365-2958.2007.05772.x

Arat S, Bullerjahn GS, Laubenbacher R. (2015) A Network Biology Approach to Denitrification in Pseudomonas Aeruginosa. *PLoS ONE* **10**:e0118235 https://doi.org/10.1371/journal.pone.0118235

Aslam M, Ahmad R, Kim J. (2018) Recent Developments in Biofouling Control in Membrane Bioreactors for Domestic Wastewater Treatment. *Separation and Purification Technology* **206**:297-315 https://doi.org/10.1016/j.seppur.2018.06.004

Bartberger MD, Liu W, Ford E, Miranda KM, Switzer C, Fukuto JM, Farmer PJ, Wink DA, Houk KN (2002) The Reduction Potential of Nitric Oxide (NO) and Its Importance to NO Biochemistry. *Proceedings of the National Academy of Sciences* **99**:10958-10963 https://doi.org/10.1073/pnas.162095599

Battin TJ, Besemer K, Bengtsson MM, Romani AM, Packmann AI (2016) The Ecology and Biogeochemistry of Stream Biofilms. *Nature Reviews Microbiology* **14**:251-263 https://doi.org/10.1038/nrmicro.2016.15

Berg S, Kutra D, Kroeger T, Straehle CN, Kausler BX, Haubold C, Schiegg M, Ales J, Beier T, Rudy M, *et al.* (2019) Ilastik: Interactive Machine Learning for (Bio)Image Analysis. *Nature Methods* **16**:1226-1232 https://doi.org/10.1038/s41592-019-0582-9

Besemer K, Singer G, Limberger R, Chlup AK, Hochedlinger G, Hödl I, Baranyi C, Battin TJ (2007) Biophysical Controls on Community Succession in Stream Biofilms. *Applied and Environmental Microbiology* **73**:4966-4974 https://doi.org/10.1128/AEM.00588-07

Bixler G, Bhushan B. (2012) Review Article: Biofouling: Lessons from Nature. *Philosophical transactions Series A, Mathematical, physical, and engineering sciences* **370**:2381-417 https://doi.org/10.1098/rsta.2011.0502

Bohn A, Zippel B, Almeida JS, Xavier JB (2007) Stochastic modeling for characterisation of biofilm development with discrete detachment events (sloughing). *Water Science and Technology: A Journal of the International Association on Water Pollution Research* **55**:257-264 https://doi.org/10.2166/wst.2007.266

Boles BR, Thoendel M, Singh PK (2005) Rhamnolipids mediate detachment of Pseudomonas aeruginosa from biofilms. *Molecular Microbiology* **57**:1210-1223 https://doi.org/10.1111/j.1365-2958.2005.04743.x

Bottero S, Storck T, Heimovaara TJ, Van Loosdrecht MCM, Enzien MV, Picioreanu C. (2013) Biofilm Development and the Dynamics of Preferential Flow Paths in Porous Media. *Biofouling* **29**:1069-1086 https://doi.org/10.1080/08927014.2013.828284

Bruus H. (2008) *Theoretical Microfluidics* OUP Oxford.

Busscher HJ, van der Mei HC (2006) Microbial Adhesion in Flow Displacement Systems. *Clinical Microbiology Reviews* **19**:127-141 https://doi.org/10.1128/CMR.19.1.127-141.2006

Characklis WG, Trulear MG, Bryers JD, Zelver N. (1982) Dynamics of Biofilm Processes: Methods. *Water Research* **16**:1207-1216 https://doi.org/10.1016/0043-1354(82)90139-7

Chen MJ, Zhang Z, Bott TR (1998) Direct measurement of the adhesive strength of biofilms in pipes by micromanipulation. *Biotechnology Techniques* **12**:875-880 https://doi.org/10.1023/A:1008805326385

Colón-González M, Méndez-Ortiz MM, Membrillo-Hernández J. (2004) Anaerobic Growth Does Not Support Biofilm Formation in Escherichia Coli K-12. *Research in Microbiology* **155**:514-521 https://doi.org/10.1016/j.resmic.2004.03.004

Colvin KM, Gordon VD, Murakami K, Borlee BR, Wozniak DJ, Wong GCL, Parsek MR (2011) The Pel Polysaccharide Can Serve a Structural and Protective Role in the Biofilm Matrix of Pseudomonas Aeruginosa. *PLoS Pathogens* **7**:e1001264 https://doi.org/10.1371/journal.ppat.1001264

Colvin KM, Irie Y, Tart CS, Urbano R, Whitney JC, Ryder C, Howell PL, Wozniak DJ, Parsek MR (2012) The Pel and Psl Polysaccharides Provide Pseudomonas Aeruginosa Structural Redundancy within the Biofilm Matrix. *Environmental microbiology* **14** https://doi.org/10.1111/j.1462-2920.2011.02657.x

Conrad JC, Poling-Skutvik R. (2018) Confined Flow: Consequences and Implications for Bacteria and Biofilms. *Annual Review of Chemical and Biomolecular Engineering* **9**:175-200 https://doi.org/10.1146/annurev-chembioeng-060817-084006

Corral Á. (2004) Long-Term Clustering, Scaling, and Universality in the Temporal Occurrence of Earthquakes. *Physical Review Letters* **92**:108501 https://doi.org/10.1103/PhysRevLett.92.108501

Costerton JW, Lewandowski Z, Caldwell DE, Korber DR, Lappin-Scott HM (1995) Microbial Biofilms. *Annual Review of Microbiology* **49**:711-745 https://doi.org/10.1146/annurev.mi.49.100195.003431

Cowle MW, Babatunde AO, Rauen WB, Bockelmann-Evans BN, Barton AF (2014) Biofilm Development in Water Distribution and Drainage Systems: Dynamics and Implications for Hydraulic Efficiency. *Environmental Technology Reviews* **3**:31-47 https://doi.org/10.1080/09593330.2014.923517

Coyte KZ, Tabuteau H, Gaffney EA, Foster KR, Durham WM (2017) Microbial Competition in Porous Environments Can Select against Rapid Biofilm Growth. *Proceedings of the National Academy of Sciences* **114**:E161-E170 https://doi.org/10.1073/pnas.1525228113

Cunningham AB, Characklis WG, Abedeen F, Crawford D. (1991) Influence of biofilm accumulation on porous media hydrodynamics. *Environmental Science & Technology* **25**:1305-1311 https://doi.org/10.1021/es00019a013 | https://doi.org/10.1021/es00019a013

Desmond P, Huisman KT, Sanawar H, Farhat NM, Traber J, Fridjonsson EO, Johns ML, Flemming HC, Picioreanu C, Vrouwenvelder JS (2022) Controlling the hydraulic resistance of membrane biofilms by engineering biofilm physical structure. *Water Research* **210**:118031 https://doi.org/10.1016/j.watres.2021.118031

Drescher K, Shen Y, Bassler BL, Stone HA (2013) Biofilm Streamers Cause Catastrophic Disruption of Flow with Consequences for Environmental and Medical Systems. *Proceedings of the National Academy of Sciences* **110**:4345-4350 https://doi.org/10.1073/pnas.1300321110

Duddu R, Chopp DL, Moran B. (2009) A Two-dimensional Continuum Model of Biofilm Growth Incorporating Fluid Flow and Shear Stress Based Detachment. *Biotechnology and Bioengineering* **103**:92-104 https://doi.org/10.1002/bit.22233

Dufrêne YF, Persat A. (2020) Mechanomicrobiology: How Bacteria Sense and Respond to Forces. *Nature Reviews Microbiology* **18**:227-240 https://doi.org/10.1038/s41579-019-0314-2

Emerenini BO, Hense BA, Kuttler C, Eberl HJ (2015) A Mathematical Model of Quorum Sensing Induced Biofilm Detachment. *PLOS One* **10**:e0132385 https://doi.org/10.1371/journal.pone.0132385

Emge P, Moeller J, Jang H, Rusconi R, Yawata Y, Stocker R, Vogel V. (2016) Resilience of Bacterial Quorum Sensing against Fluid Flow. *Scientific Reports* **6**:33115 https://doi.org/10.1038/srep33115

Flemming HC, Wingender J. (2010) The Biofilm Matrix. *Nature Reviews Microbiology* **8**:623-633 https://doi.org/10.1038/nrmicro2415

Flemming HC, Wingender J, Szewzyk U, Steinberg P, Rice SA, Kjelleberg S. (2016) Biofilms: An Emergent Form of Bacterial Life. *Nature Reviews Microbiology* **14**:563-575 https://doi.org/10.1038/nrmicro.2016.94

Folsom JP, Richards L, Pitts B, Roe F, Ehrlich GD, Parker A, Mazurie A, Stewart PS (2010) Physiology of Pseudomonas Aeruginosa in Biofilms as Revealed by Transcriptome Analysis. *BMC Microbiology* **10**:294 https://doi.org/10.1186/1471-2180-10-294

García S, Trueba A. (2020) Fouling in Heat Exchangers. In: Bhattacharya S, Moghimi Ardekani M, Biswas R, C Mehta R (Eds). *Inverse Heat Conduction and Heat Exchangers IntechOpen* https://doi.org/10.5772/intechopen.88079

Padron GC, Shuppara AM, Sharma A, Koch MD, Palalay JS, Radin JN, Kehl-Fie TE, Imlay JA, Sanfilippo JE (2023) Shear rate sensitizes bacterial pathogens to H2O2 stress. *Proceedings of the National Academy of Sciences* **120**:e2216774120

Gloag ES, Fabbri S, Wozniak DJ, Stoodley P. (2020) Biofilm Mechanics: Implications in Infection and Survival. *Biofilm* **2**:100017 https://doi.org/10.1016/j.bioflm.2019.100017

Guaglianone E, Cardines R, Vuotto C, Di Rosa R, Babini V, Mastrantonio P, Donelli G. (2010) Microbial Biofilms Associated with Biliary Stent Clogging. *FEMS Immunology & Medical Microbiology* **59**:410-420 https://doi.org/10.1111/j.1574-695X.2010.00686.x

Howell JA, Atkinson B. (1976) Sloughing of microbial film in trickling filters. *Water Research* **10**:307-315 https://doi.org/10.1016/0043-1354(76)90172-X

Jiang Z, Nero T, Mukherjee S, Olson R, Yan J. (2021) Searching for the Secret of Stickiness: How Biofilms Adhere to Surfaces. *Frontiers in Microbiology* **12** https://doi.org/10.3389/fmicb.2021.686793

Kaplan JB (2010) Biofilm Dispersal: Mechanisms, Clinical Implications, and Potential Therapeutic Uses. *Journal of Dental Research* **89**:205-218 https://doi.org/10.1177/0022034509359403

Kim MK, Ingremeau F, Zhao A, Bassler BL, Stone HA (2016) Local and Global Consequences of Flow on Bacterial Quorum Sensing. *Nature Microbiology* **1**:15005 https://doi.org/10.1038/nmicrobiol.2015.5

Körstgens V, Flemming HC, Wingender J, Borchard W. (2001) Uniaxial compression measurement device for investigation of the mechanical stability of biofilms. *Journal of Microbiological Methods* **46**:9-17 https://doi.org/10.1016/s0167-7012(01)00248-2

Krsmanovic M, Biswas D, Ali H, Kumar A, Ghosh R, Dickerson AK (2021) Hydrodynamics and Surface Properties Influence Biofilm Proliferation. *Advances in Colloid and Interface Science* **288**:102336 https://doi.org/10.1016/j.cis.2020.102336

Kryachko Y. (2018) Novel Approaches to Microbial Enhancement of Oil Recovery. *Journal of Biotechnology* **266**:118-123 https://doi.org/10.1016/j.jbiotec.2017.12.019

Kumar P, Korkolis E, Benzi R, Denisov D, Niemeijer A, Schall P, Toschi F, Trampert J. (2020) On Interevent Time Distributions of Avalanche Dynamics. *Scientific Reports* **10**:626 https://doi.org/10.1038/s41598-019-56764-6

Kurz DL, Secchi E, Carrillo FJ, Bourg IC, Stocker R, Jimenez-Martinez J. (2022) Competition between Growth and Shear Stress Drives Intermittency in Preferential Flow Paths in Porous Medium Biofilms. *Proceedings of the National Academy of Sciences* **119**:e2122202119 https://doi.org/10.1073/pnas.2122202119

Lau PCY, Dutcher JR, Beveridge TJ, Lam JS (2009) Absolute Quantitation of Bacterial Biofilm Adhesion and Viscoelasticity by Microbead Force Spectroscopy. *Biophysical Journal* **96**:2935-2948 https://doi.org/10.1016/j.bpj.2008.12.3943

Lee SH, Secchi E, Kang PK (2023) Rapid Formation of Bioaggregates and Morphology Transition to Biofilm Streamers Induced by Pore-Throat Flows. *Proceedings of the National Academy of Sciences* **120**:e2204466120 https://doi.org/10.1073/pnas.2204466120

Lennox J, Ashe J. (2009) Biofilms as Biobarriers. *The American Biology Teacher* **71**:20-26 https://doi.org/10.2307/27669358

Lewandowski Z, Beyenal H, Stookey D. (2004) Reproducibility of biofilm processes and the meaning of steady state in biofilm reactors. *Water Science and Technology: A Journal of the International Association on Water Pollution Research* **49**:359-364

Maaß R, Wraith M, Uhl JT, Greer JR, Dahmen KA (2015) Slip Statistics of Dislocation Avalanches under Different Loading Modes. *Physical Review E* **91**:042403 https://doi.org/10.1103/PhysRevE.91.042403

Mukherjee S, Bassler BL (2019) Bacterial Quorum Sensing in Complex and Dynamically Changing Environments. *Nature Reviews Microbiology* **17**:371-382 https://doi.org/10.1038/s41579-019-0186-5

Ohashi A, Harada H. (1996) A novel concept for evaluation of biofilm adhesion strength by applying tensile force and shear force. *Water Science and Technology* **34**:201-211 https://doi.org/10.1016/0273-1223(96)00647-6

Paul E, Ochoa JC, Pechaud Y, Liu Y, Liné A. (2012) Effect of Shear Stress and Growth Conditions on Detachment and Physical Properties of Biofilms. *Water Research* **46**:5499-5508 https://doi.org/10.1016/j.watres.2012.07.029

Peterson BW, He Y, Ren Y, Zerdoum A, Libera Matthew R, Sharma PK, van Winkelhoff AJ, Neut D, Stoodley P, van der Mei HC, *et al.* (2015) Viscoelasticity of Biofilms and Their Recalcitrance to Mechanical and Chemical Challenges. *FEMS microbiology reviews* **39**:234-245 https://doi.org/10.1093/femsre/fuu008

Picioreanu C, Van Loosdrecht MC, Heijnen JJ (2000) Effect of Diffusive and Convective Substrate Transport on Biofilm Structure Formation: A Two-Dimensional Modeling Study. *Biotechnology and Bioengineering* **69**:504-515 https://doi.org/10.1002/1097-0290(20000905)69:5<504::aid-bit5>3.0.co;2-s

Ramos G, Toulouze C, Rima M, Liot O, Duru P, Davit Y. (2023) Ultraviolet Control of Bacterial Biofilms in Microfluidic Chips. *Biomicrofluidics* **17**:024107 https://doi.org/10.1063/5.0135722

Rasamiravaka T, Labtani Q, Duez P, El Jaziri M. (2015) The Formation of Biofilms by Pseudomonas Aeruginosa : A Review of the Natural and Synthetic Compounds Interfering with Control Mechanisms. *BioMed Research International* **2015**:1-17 https://doi.org/10.1155/2015/759348

Rittman BE (1982) The Effect of Shear Stress on Biofilm Loss Rate. *Biotechnology and Bioengineering* **24**:501-506 https://doi.org/10.1002/bit.260240219

Rittmann BE (1993) The significance of biofilms in porous media. *Water Resources Research* **29**:2195-2202 https://doi.org/10.1029/93WR00611

Rodesney CA, Roman B, Dhamani N, Cooley BJ, Katira P, Touhami A, Gordon VD (2017) Mechanosensing of Shear by Pseudomonas Aeruginosa Leads to Increased Levels of the Cyclic-Di-GMP Signal Initiating Biofilm Development. *Proceedings of the National Academy of Sciences* **114**:5906-5911 https://doi.org/10.1073/pnas.1703255114

Rossy T, Nadell CD, Persat A. (2019) Cellular Advective-Diffusion Drives the Emergence of Bacterial Surface Colonization Patterns and Heterogeneity. *Nature Communications* **10**:2471 https://doi.org/10.1038/s41467-019-10469-6

Rusconi R, Lecuyer S, Autrusson N, Guglielmini L, Stone HA (2011) Secondary Flow as a Mechanism for the Formation of Biofilm Streamers. *Biophysical Journal* **100**:1392-1399 https://doi.org/10.1016/j.bpj.2011.01.065

Ryder C, Byrd M, Wozniak DJ (2007) Role of Polysaccharides in Pseudomonas Aeruginosa Biofilm Development. *Current Opinion in Microbiology* **10**:644-648 https://doi.org/10.1016/j.mib.2007.09.010

Sabra W, Kim EJ, Zeng AP (2002) Physiological Responses of Pseudomonas Aeruginosa PAO1 to Oxidative Stress in Controlled Microaerobic and Aerobic Cultures. *Microbiology (Reading, England)* **148**:3195-3202 https://doi.org/10.1099/00221287-148-10-3195

Sampedro I, Parales RE, Krell T, Hill JE (2014) Pseudomonas Chemotaxis. *FEMS Microbiology Reviews* https://doi.org/10.1111/1574-6976.12081

Sanfilippo JE, Lorestani A, Koch MD, Bratton BP, Siryaporn A, Stone HA, Gitai Z. (2019) Microfluidic-Based Transcriptomics Reveal Force-Independent Bacterial Rheosensing. *Nature Microbiology* **4**:1274-1281 https://doi.org/10.1038/s41564-019-0455-0

Schneider CA, Rasband WS, Eliceiri KW (2012) NIH Image to ImageJ: 25 Years of Image Analysis. *Nature methods* **9**:671-675

Sen R. (2008) Biotechnology in Petroleum Recovery: The Microbial EOR. *Progress in Energy and Combustion Science* **34**:714-724 https://doi.org/10.1016/j.pecs.2008.05.001

Sharp RR, Stoodley P, Adgie M, Gerlach R, Cunningham A. (2005) Visualization and Characterization of Dynamic Patterns of Flow, Growth and Activity of Biofilms Growing in Porous Media. *Water Science and Technology* **52**:85-90 https://doi.org/10.2166/wst.2005.0185

Singh R, Paul D, Jain RK (2006) Biofilms: Implications in Bioremediation. *Trends in Microbiology* **14**:389-397 https://doi.org/10.1016/j.tim.2006.07.001

Stewart TL, Fogler HS (2001) Biomass Plug Development and Propagation in Porous Media. *Biotechnology and Bioengineering* **72**:353-363 https://doi.org/10.1002/1097-0290(20010205)72:3<353::AID-BIT13>3.0.CO;2-U

Stewart TL, Scott Fogler H. (2002) Pore-scale Investigation of Biomass Plug Development and Propagation in Porous Media. *Biotechnology and Bioengineering* **77**:577-588 https://doi.org/10.1002/bit.10044

Stickler DJ (2014) Clinical Complications of Urinary Catheters Caused by Crystalline Biofilms: Something Needs to Be Done. *Journal of Internal Medicine* **276**:120-129 https://doi.org/10.1111/joim.12220

Stoodley P, Dodds I, Jd Boyle, Hm Lappin-Scott (1998) Influence of Hydrodynamics and Nutrients on Biofilm Structure. *Journal of Applied Microbiology* **85**:19S-28S https://doi.org/10.1111/j.1365-2672.1998.tb05279.x

Taherzadeh D, Picioreanu C, Horn H. (2012) Mass Transfer Enhancement in Moving Biofilm Structures. *Biophysical Journal* **102**:1483-1492 https://doi.org/10.1016/j.bpj.2012.02.033

Talon L. (2022) On the Determination of a Generalized Darcy Equation for Yield Stress Fluid in Porous Media. *Science Talks* **3**:100042 https://doi.org/10.1016/j.sctalk.2022.100042

Taylor SW, Jaffé PR. (1990) Biofilm growth and the related changes in the physical properties of a porous medium: 1. Experimental investigation. *Water Resources Research* **26**:2153-2159 https://doi.org/10.1029/WR026i009p02153

Taylor SW, Jaffé PR. (1990) Biofilm growth and the related changes in the physical properties of a porous medium: 3. Dispersivity and model verification. *Water Resources Research* **26**:2171-2180 https://doi.org/10.1029/WR026i009p02171

Taylor SW, Jaffé PR. (1990) Substrate and biomass transport in a porous medium. *Water Resources Research* **26**:2181-2194 https://doi.org/10.1029/WR026i009p02181

Taylor SW, Milly PCD, Jaffé PR. (1990) Biofilm growth and the related changes in the physical properties of a porous medium: 2. Permeability. *Water Resources Research* **26**:2161-2169 https://doi.org/10.1029/WR026i009p02161

Telgmann U, Horn H, Morgenroth E. (2004) Influence of Growth History on Sloughing and Erosion from Biofilms. *Water Research* **38**:3671-3684 https://doi.org/10.1016/j.watres.2004.05.020

Thomen P, Robert J, Monmeyran A, Bitbol AF, Douarche C, Henry N. (2017) Bacterial Biofilm under Flow: First a Physical Struggle to Stay, Then a Matter of Breathing. *PLoS ONE* **12**:e0175197 https://doi.org/10.1371/jour-nal.pone.0175197

Torrence C, Compo GP (1998) A Practical Guide to Wavelet Analysis. *Bulletin of the American Meteorological Society* **79**:61-78 https://doi.org/10.1175/1520-0477(1998)079<0061:APGTWA>2.0.CO;2

Vandevivere P, Baveye P. (1992) Effect of bacterial extracellular polymers on the saturated hydraulic conductivity of sand columns. *Applied and Environmental Microbiology* **58**:1690-1698 https://doi.org/10.1128/aem.58.5.1690-1698.1992

Vandevivere P, Baveye P. (1992) Saturated Hydraulic Conductivity Reduction Caused by Aerobic Bacteria in Sand Columns. *Soil Science Society of America Journal* **56**:1-13 https://doi.org/10.2136/ss-saj1992.03615995005600010001x

Verran J. (2002) Biofouling in Food Processing: Biofilm or Biotransfer Potential. *Food and Bioproducts Processing* **80**:292-298 https://doi.org/10.1205/096030802321154808

Wagner M, Manz B, Volke F, Neu TR, Horn H. (2010) Online Assessment of Biofilm Development, Sloughing and Forced Detachment in Tube Reactor by Means of Magnetic Resonance Microscopy. *Biotechnology and Bioengineering* **107**:172-181 https://doi.org/10.1002/bit.22784

Wang S, Zhu H, Zheng G, Dong F, Liu C. (2022) Dynamic Changes in Biofilm Structures under Dynamic Flow Conditions. *Applied and Environmental Microbiology* **88**:e01072-22 https://doi.org/10.1128/aem.01072-22

Welch P. (1967) The Use of Fast Fourier Transform for the Estimation of Power Spectra: A Method Based on Time Averaging over Short, Modified Periodograms. *IEEE Transactions on Audio and Electroacoustics* **15**:70-73 https://doi.org/10.1109/TAU.1967.1161901

Wilson S, Hamilton MA, Hamilton GC, Schumann MR, Stoodley P. (2004) Statistical Quantification of Detachment Rates and Size Distributions of Cell Clumps from Wild-Type (PAO1) and Cell Signaling Mutant (JP1) Pseudomonas Aeruginosa Biofilms. *Applied and Environmental Microbiology* **70**:5847-5852 https://doi.org/10.1128/AEM.70.10.5847-5852.2004

Kurz D. L., Secchi E., Stocker R., Jimenez-Martinez J. (2023) Morphogenesis of biofilms in porous media and control on hydrodynamics. *Environ Sci Technol* **57**:5666-5677

Peer reviews

Reviewer #1 (Public review):

Summary:

The paper investigates the interplay between fluid flow and biofilm development using Pseudomonas aeruginosa PAO1 in microfluidic channels. By combining experimental

observations with mathematical modeling, the study identifies the significant impact of nutrient limitation and hydrodynamic forces on biofilm growth and detachment. The authors demonstrate that nutrient limitation drives the longitudinal distribution of biomass, while flow-induced detachment influences the maximum clogging and temporal dynamics. The study highlights that pressure buildup plays a critical role in biofilm detachment, leading to cyclic episodes of sloughing and regrowth. A stochastic model is used to describe the detachment process, capturing the apparent randomness of sloughing events. The findings offer insights into biofilm behavior during clogging and fouling, potentially relevant to infections, environmental processes, and engineering applications.

Strengths:

This paper demonstrates a strong integration of experimental work and mathematical modeling, providing a comprehensive understanding of biofilm dynamics in a straight microfluidic channel. The simplicity of the microchannel geometry allows for accurate modeling, and the findings have the potential to be applied to more complex geometries. The detailed analysis of nutrient limitation and its impact on biofilm growth offers valuable insights into the conditions that drive biofilm formation. The model effectively describes biofilm development across different stages, capturing both initial growth and cyclic detachment processes. While cyclic pressure buildup has been studied previously, the incorporation of a stochastic model to describe detachment events is a novel and significant contribution, capturing the complexity and randomness of biofilm behavior. Finally, the investigation of pressure buildup and its role in cyclic detachment and regrowth enhances our understanding of the mechanical forces at play, making the findings applicable to a wide range of technological and clinical contexts.

Weaknesses:

The study achieves its primary objective of combining experiments and modeling to elucidate the coupling between flow, biofilm growth, and detachment in a confined microfluidic channel. In the revised manuscript, the authors have clarified several methodological choices and underlying assumptions. The points below are best viewed not as weaknesses, but as aspects that define the scope of the approach.

• Biofilm porosity and permeability. The authors now discuss biofilm porosity and provide a clear rationale for neglecting permeability effects in their system, arguing that flow around dense biofilm structures dominates over flow through the matrix. While this assumption appears reasonable for the conditions explored, permeability effects are not explicitly modeled and could become relevant in less compact or more heterogeneous biofilms.

• Characterization of the EPS matrix. The role of the extracellular matrix is convincingly addressed using polysaccharide-deficient mutants, which provides a strong and causal link between EPS composition and mechanical stability. At the same time, the absence of complementary biochemical or imaging-based characterization means that spatial or temporal variations in EPS distribution are not directly resolved, limiting the level of structural details.

• Three-dimensional interpretation of biofilm development. The authors clarify that three-dimensional information is primarily obtained from pressure-based measurements, with two-dimensional imaging serving as a validation tool. This approach is coherent and supported by scaling arguments and reproducibility across experiments.

https://doi.org/10.7554/eLife.98292.2.sa1

Author response:

The following is the authors' response to the original reviews.

We sincerely thank the reviewer for the thorough and constructive evaluation of our manuscript. We greatly appreciate the recognition of our work's strengths, particularly the integration of experiments and mathematical modeling, the stochastic framework for describing sloughing events, and the insights into pressure-driven detachment dynamics.

We have carefully considered each point raised and provide detailed responses below. In response to the reviewer's comments, we have revised the Methods section to better clarify our approach to three-dimensional assessment. We believe these revisions have improved the clarity of the manuscript.

Below, we address each of the specific concerns raised by the reviewer:

> ***Public Reviews:***
>
> ***Reviewer #1 (Public review):***
>
> *Weaknesses:*
>
> *The study achieves its primary goal of integrating experiments and modeling to understand the coupling between flow and biofilm growth and detachment in a microfluidic channel, but it should have highlighted the weaknesses of the methods. I list the ones that, in my opinion, are the main ones:*
>
> *The study does not consider biofilm porosity, which could significantly affect the flow and forces exerted on the biofilm. Porosity could impact the boundary conditions, such as the no-slip condition, which should be validated experimentally.*

Porosity is indeed a key component of biofilm structures, resulting from the polymeric nature of the EPS matrix, mechanical forces, and biological processes such as cell death or predation. When considering flow-biofilm interactions, this porosity may allow fluid flow through the biofilm, with reported permeability values spanning an extremely broad range from 10^{-15} to 10^{-7} m^2 (Kurz et al., 2023).

However, we argue that biofilm permeability is not the primary driver in our system:

(1) In microscopy visualization, our biofilms form dense structures where flow around the biofilm through narrow channels dominates over flow through the porous biofilm matrix.

(2) We performed microrheology experiments in these biofilms by imaging the Brownian motion of nanoparticles in the biofilm. Their trajectories indicate that, in our conditions, the viscoelastic flow of the biofilm itself largely dominates over the flow of culture medium through the biofilm matrix.

(3) We argue that the extreme variability in reported permeability values (spanning several orders of magnitude, Kurz et al., 2023) reflects not only differences in experimental systems, but also fundamental challenges in defining and measuring permeability for viscoelastoplastic biofilms (the biofilm itself is actually flowing). Given this uncertainty, incorporating permeability into our model would introduce parameters that cannot be reliably constrained from literature or independently measured in our setup. Our approach (i.e. treating the biofilm as impermeable and focusing on flow obstruction) avoids this parametrization complexity while successfully capturing the observed dynamics.

(4) Our model successfully predicts the observed scaling laws ($\phi_{max} \propto Q^{1/2}$, Fig. 7f) and hydraulic resistance dynamics (Fig. 3) without invoking permeability, suggesting that flow

obstruction rather than flow penetration is the dominant mechanism.

Reference: Kurz, D. L.; Secchi, E.; Stocker, R.; Jimenez-Martinez, J. Morphogenesis of biofilms in porous media and control on hydrodynamics. Environ. Sci. Technol. 2023, 57 (14), 5666−5677.

> *The research suggests EPS development as a stage in biofilm growth but does not probe it using lectin staining. This makes it impossible to accurately assess the role of EPS in biofilm development and detachment processes.*

We respectfully disagree that lectin staining is necessary to assess the role of EPS in our system, and we argue that our approach using genetic mutants is superior for the following reasons. Lectin staining has significant limitations. While widely used, lectin staining (e.g., concanavalin A) is non-specific (binding not only to EPS polysaccharides but also to bacterial cell surfaces) and is non-quantitative. It can confirm the presence of polysaccharides but cannot establish causal relationships between specific EPS components and mechanical properties or detachment dynamics. We performed preliminary experiments with ConA-rhodamine (data not shown), which showed widespread presence of polysaccharides. However, this provided limited insight beyond confirming EPS production, which is well-established for *P. aeruginosa* PAO1 biofilms. We employed a more rigorous genetic approach to directly assess the role of EPS composition. We used Δpel and Δpsl mutants (strains lacking key exopolysaccharides that are the primary structural components of the PAO1 matrix). Our results demonstrate that both mutants show significantly reduced maximum clogging compared to wild-type. The Δpsl mutant is particularly affected, with near-complete detachment at certain flow rates. These differences directly link EPS composition to mechanical stability and detachment dynamics. This genetic approach provides causal, quantitative evidence for the role of specific EPS components in biofilm development and detachment, information that lectin staining cannot provide. We believe this addresses the reviewer's concern more rigorously than lectin staining would.

> *While the force and flow are three-dimensional, the images are taken in two dimensions. The paper does not clearly explain how the 2D images are extrapolated to make 3D assessments, which could lead to inaccuracies.*

We thank the reviewer for this important observation. We would like to clarify our methodological approach. Our primary three-dimensional measurement is the hydraulic resistance R(t), obtained from pressure drop measurements across the biofilm-containing channel section. This pressure-based measurement inherently captures the three-dimensional flow obstruction caused by the biofilm. We then employ a geometric model (uniform biofilm layer on all channel walls) to convert R(t) into volume fraction $\phi(t)$.

The two-dimensional fluorescence imaging serves to validate this model-based approach rather than being the basis for three-dimensional extrapolation. The uniform layer assumption is supported by three independent lines of evidence: (i) the excellent quantitative agreement between predicted and measured scaling laws ($\phi_{max} \propto Q^{1/2}$, Fig. 7f), obtained without adjustable parameters; (ii) the high reproducibility of ϕ_{max} values across different flow rates and replicates; and (iii) the strong correlation between model-derived $\phi(t)$ from pressure measurements and integrated fluorescence intensity (Fig. 3b-d).

We have added clarifying text in the Methods section (subsection "Data analysis for the calculation of the hydraulic resistance and volume fraction") to better explain this approach and emphasize that pressure measurements provide the three-dimensional information, with the geometric model serving as the link to volume fraction.

> *Although the findings are tested using polysaccharide-deficient mutants, the results could have been analyzed in greater detail. A more thorough analysis would help to better understand the role of matrix composition on the stochastic model of detachment.*

We thank the reviewer for this suggestion. Our mutant analysis demonstrates that Δpsl and Δpel strains have significantly reduced ϕ_{max} and altered detachment dynamics compared to wild-type (Fig. 8), directly linking EPS composition to mechanical stability as predicted by our model. A rigorous quantitative connection between matrix composition and the stochastic parameters (interevent times, jump amplitudes) would require: (i) substantially more sloughing events for statistical power, (ii) independent mechanical characterization of each mutant, and (iii) a mechanistic model linking EPS composition to detachment parameters. We are currently developing microrheology approaches to characterize mutant mechanical properties, which could enable such refinement in future work.

However, this represents a substantial study beyond the scope of the current manuscript, which establishes the self-sustained sloughing-regrowth cycle and its stochastic nature. The mutant results serve their intended purpose: demonstrating that EPS composition affects detachment, consistent with our model's framework.

> ***Reviewer #2 (Public review):***
>
> *This manuscript develops well-controlled microfluidic experiments and mathematical modelling to resolve how the temporal development of P. aeruginosa biofilms is shaped by ambient flow. The experiment considers a simple rectangular channel on which a constant flow rate is applied and UV LEDs are used to confine the biofilm to a relatively small length of device. While there is often considerable geometrical complexity in confined environments and feedback between biofilm/flow (e.g. in porous media), these simplified conditions are much more amenable to analysis. A non-dimensional mathematical model that considers nutrient transport, biofilm growth and detachment is developed and used to interpret experimental data. Regimes with both gradual detachment and catastrophic sloughing are considered. The concentration of nutrients in the media is altered to resolve the effect of nutrient limitation. In addition, the role of a couple of major polysaccharide EPS components are explored with mutants, which leads results in line with previous studies.*
>
> *There has been a vast amount of experimental and modelling work done on biofilms, but relatively rarely are the two linked together so tightly as in this paper. Predictions on influence of the non-dimensional Damkohler number on the longitudinal distribution of biofilm and functional dependence of flow on the maximum amount of biofilm (ϕ_{max}) are demonstrated. The study reconfirms a number of previous works that showed the gradual detachment rate of biofilms scales with the square root of the shear stress. More challenging are the rapid biofilm detachment events where a large amount of biofilm is detached at once. These events occur are identified experimentally using an automated analysis pipeline and are fitted with probability distributions. The time between detachment events was fitted with a Gamma distribution and the amplitude of the detachment events was fitted with a log-normal distribution, however, it is not clear how good these fits are. Experimental data was then used as an input for a stochastic differential equation, but the output of this model is compared only qualitatively to that of the experiments. Overall, this paper does an admirable job of developing a well-constrained experiments and a tightly integrated mathematical framework through which to interpret them. However, the new insights this provides the underlying physical/biological mechanisms are relatively limited.*

We thank the reviewer for the thorough evaluation of our work and for highlighting the tight integration between experiments and modeling. We appreciate the constructive feedback

regarding the goodness-of-fit for the probability distributions.

To address the concern that "it is not clear how good these fits are," we have added quantile-quantile (Q-Q) plots for the Gamma distribution fits of inter-event times to the Supplementary Materials (Supplementary Figure S20). These plots demonstrate that the sample quantiles track the theoretical Gamma quantiles across all flow rates (0.2, 2, and 20 μL/min), indicating that the Gamma distribution provides a reasonable approximation of the overall distributional behavior. For detachment amplitudes, we selected the lognormal distribution based on the observed high skewness and kurtosis in the data, which are characteristic signatures of lognormal processes.

Formal goodness-of-fit tests (chi-square, Kolmogorov-Smirnov) yielded mixed results across datasets, passing for some while failing for others. This variability reflects inherent noise from measurements, discrete temporal sampling, automated detection thresholds, and intrinsic biological variability. Importantly, our goal is to capture essential distributional characteristics for input into the stochastic model, not to achieve perfect statistical fit across all individual datasets. The Q-Q plots confirm that these distributions provide reasonable approximations, and the qualitative agreement between model predictions and experimental observations validates this modeling approach. We have revised the Methods section to clarify this rationale.

We respectfully disagree that “new insights this provides the underlying physical/biological mechanisms are relatively limited.” Beyond confirming previous findings (e.g., scaling for gradual detachment), we believe our work provides several novel mechanistic insights. First, the Pe/Da criterion enables quantitative prediction of nutrient limitation regimes, allowing systematic decoupling of nutrient effects from other phenomena in biofilm studies. Second, we demonstrate that pressure, not shear, drives sloughing detachment events, a mechanism overlooked in previous studies where the notion of “shear-induced detachment” clearly dominates. Third, we show that sloughing-regrowth cycles occur even in single channels, establishing pressure-driven fluctuations as a signature of confined biofilm growth, independent of geometric complexity. Finally, the stochastic description of sloughing demonstrates that, while instantaneous biofilm states are irreproducible, the underlying randomness is predictable, therefore addressing a fundamental challenge in biofilm research.

> ***Recommendations For The Authors:***
>
> ***Reviewer #1 (Recommendations For The Authors):***
>
> *(1) In the abstract, I suggest clarifying the term "bacteria development." It is unclear if it refers to bacterial growth, biofilm formation, or biofilm detachment. The concept is expressed more clearly at the end of the Introduction.*

We have modified the entire abstract to make it clearer. The abstract now explicitly establishes the key processes - growth ('nutrients necessary for growth', 'growing bacteria obstruct flow paths') and detachment ('mechanical stresses that cause detachment', 'flow-induced detachment', 'sloughing') - before using 'bacterial development' as a collective term to refer to these coupled spatiotemporal dynamics. We believe the abstract is now clear as written.

> *(2) Findings from Sanfilippo et al. (2019) were slightly questioned by Padron et al. (PNAS, 2023), who discovered that H2O2 transport is responsible for fro operon upregulation.*

Thanks for the clarification, which is indeed significant. The new sentence now reads: *Pseudomonas aeruginosa* has been found to regulate the fro operon in response to flow-modulated H2O2 concentrations (Sanfilippo et al. 2019, Padron et al. 2023).

> *(3) Additionally, Kurz et al. (2022) account for pressure buildup as the mechanism controlling sloughing.*

We respectfully disagree and note that Kurz et al. (2022) identify shear stress, not pressure buildup, as the primary mechanism controlling sloughing. Besides the title, key sentences include “opening was driven by a physical process and specifically by the shear forces associated with flow through the biofilm”, “The opening of the PFPs is driven by flow-induced shear stress, which increases as a PFP becomes narrower due to microbial growth, causing biofilm compression and rupture.” While pressure differences are measured as indicators of system state and do contribute to normal compression stresses, their mechanistic explanation emphasizes that narrowing PFPs experience increased shear rates that eventually exceed the biofilm's yield stress, triggering viscoplastic deformation and detachment. The pressure buildup is a hydraulic consequence of narrowing rather than the direct cause of sloughing. In contrast, our work demonstrates that in confined geometries, pressure differences generate tangential stresses at the biofilm-solid interface that directly drive detachment.

> *(4) The flow control strategy represented in Fig. 1 is not explained and should be detailed in the Methods section.*

The methods section reads as follows. Inoculation and flow experiments BHI suspensions were adjusted at optical density at OD640nm= 0.2 (108 CFU/mL) and inoculated inside the microchannels from the outlet, up to approximately ¾ of the channel length in order to keep a clean inlet. The system was let at room temperature (25°C) for 3h under static conditions. Flow experiments were then performed at 0.02, 0.2, 2, 20 and 200 µL/min constant flow rates for 72h in the microchannels at room temperature. For the experiments at 0.2, 2, 20 and 200 µL/min, the fluidic system was based on a sterile culture medium reservoir pressurized by a pressure controller (Fluigent FlowEZ) and connected with a flow rate controller (Fluigent Flow unit). The flow rate was maintained constant by using a controller with a feedback loop adjusting the pressure in the liquid reservoir. The reservoir was connected to the chip using Tygon tubing (Saint Gobain Life Sciences Tygon™ ND 100-80) of 0.52 mm internal diameter and 1.52 mm external diameter, along with PEEK tubing (Cytiva Akta pure) with 0.25 mm inner diameter adapters for flow rate controller. The waste container was also pressurized by another independent pressure controller to reduce air bubble formation in the inlet part. For the experiments at 0.02 µL/min, we used an Harvard Phd2000 syringe pump for the flow.

> *(5) Including images of the actual biofilms formed in a portion of the channel would aid in understanding the analysis presented in Fig. 2.*

Images are introduced later on (eg Figure 5). There is also supplementary material showing videos.

> *(6) The boundary conditions used to calculate the stress in the developed model should be discussed. The authors should specify why biofilm porosity is neglected.*

We have added a detailed discussion in the supplementary (Section I.2).

> *(7) In the first section of the Results, the authors hypothesize that heterogeneity in biofilm development could be due to oxygen limitation. However, given the high oxygen permeability of PDMS, this hypothesis is later denied by their data. It would be prudent to avoid this hypothesis initially to streamline the presentation. Additionally, the authors should specify how oxygen levels at the inlet and outlet are measured.*

We appreciate this comment and agree that streamlining would simplify the presentation. However, after careful consideration, we have chosen to retain the oxygen limitation hypothesis for the following reasons: (1) oxygen limitation is a frequently invoked mechanism in biofilm systems and deserves explicit consideration, (2) it is not immediately

obvious that oxygen remains non-limiting in larger microchannels where transverse gradients could develop, and (3) systematically eliminating this plausible alternative hypothesis strengthens our mechanistic conclusion that BHI drives the observed heterogeneity. Regarding oxygen measurements: we did not directly measure dissolved oxygen concentrations. Our approach is only indirect.

> *(8) What is the standard deviation of the doubling time measured at different flows (page 9)?*

We have indicated the standard deviation in the text. Note that the graph shows the SEM.

> *(9) What is the "zone of interest" in the channel mentioned on page 9?*

We have added the following sentence to clarify: To further understand this effect, let us consider the mass balance of biofilm in the zone of interest -- the zone where biofilm grows in between the two UVC irradiation zones -- in the channel.

> *(10) Minor and major detachment events should be classified based on a defined threshold or criteria, and their frequency should be measured.*

We appreciate the reviewer's concern about quantitative rigor. However, we respectfully disagree that imposing arbitrary thresholds to classify 'minor' vs. 'major' events would improve our analysis. Detachment events in our system span a continuum of magnitudes, and any threshold would be artificial and potentially misleading. Our quantitative characterization of detachment dynamics is provided through the statistical analysis of interevent times, which we show follow a gamma distribution. This stochastic framework captures the full spectrum of detachment behavior without requiring arbitrary binning. The terms 'minor' and 'major' in our manuscript are used qualitatively to illustrate the range of observed phenomena, not as formal classifications.

> *(11) Have the authors identified a reason for the peaks in the volume fraction in the Δpsl mutants at the highest flow rate?*

The biofilm thickness following these sloughing events is below our detection limit, consistent with a residual layer of cells. However, these cells grow, leading to a time window where the fraction is measurable, before a new detachment event occurs. Our understanding is that the psl mutant forms a weaker matrix with a much lower threshold for sloughing.

> *(12) The fit of the probability density function for the relative density function does not match the data well. The authors should comment on this.*

We have added quantile-quantile (Q-Q) plots for the Gamma distribution fits of inter-event times to the Supplementary Materials (Supplementary Figure S20). These plots demonstrate that the sample quantiles track the theoretical Gamma quantiles across all flow rates (0.2, 2, and 20 μL/min), indicating that the Gamma distribution provides a reasonable approximation of the overall distributional behavior. For detachment amplitudes, we selected the lognormal distribution based on the observed high skewness and kurtosis in the data, which are characteristic signatures of lognormal processes. Formal goodness-of-fit tests (chi-square, Kolmogorov-Smirnov) yielded mixed results across datasets, passing for some while failing for others. This variability reflects inherent noise from measurements, discrete temporal sampling, automated detection thresholds, and intrinsic biological variability. Importantly, our goal is to capture essential distributional characteristics for input into the stochastic model, not to achieve perfect statistical fit across all individual datasets. The Q-Q plots confirm that these distributions provide reasonable approximations, and the qualitative agreement between model predictions and experimental observations validates this modeling approach. We have revised the Methods section to clarify this rationale.

> *(13) Additionally, the simulated fraction appears very flat, with limited detachments compared to experiments. Why?*

The model captures the essential dynamics of growth-detachment cycles, including the characteristic timescales and volume fraction ranges. Some event-to-event variability in the experimental data likely reflects biological stochasticity not captured by our current approach—for example, variations in local biofilm mechanical properties or matrix composition that affect the precise stress at which sloughing occurs. While incorporating such biological variability as a stochastic parameter would improve detailed agreement, it would require extensive additional characterization beyond the scope of this study. The current model successfully reproduces the key qualitative and semi-quantitative features of the system.

> *(14) The methods section should include a more detailed explanation of how the model was validated against experimental data.*

Model validation was performed by comparing predicted biofilm volume fraction time series and sloughing event statistics against experimental observations across multiple flow rates. The model reproduces the characteristic growth-sloughing cycles, timescales, and steady-state volume fractions without additional parameter fitting beyond the experimentally measured distributions.

> *(15) It would be useful to include information on the reproducibility of the experiments and any variations observed between replicates.*

Experiments were performed in N=3 biological replicates. Individual time series for all replicates are shown in Supplementary Figures, demonstrating consistent behavior across replicates.

> *(16) A discussion of the limitations of the study, particularly regarding the assumptions made in the modeling and their potential impact on the results, would strengthen the paper.*

We have added a discussion on why we chose to neglect the porosity of the biofilm, and strengthened parts on the uniform biofilm layer assumption.

> ***Reviewer #2 (Recommendations For The Authors):***
>
> *Page 2: "A vast" —> "The vast"*

Changed.

> *The text and line widths on many of the figures are far too small. I printed it out at normal size, but had to look at a PDF and magnify to actually see what the graphs are showing. Fig. 9c is particularly illegible.*

Changed.

> *Fig. 1 caption "photonic" —> "optical"?*

Changed

> *Can you spell out the actual mathematical definition of ϕ on page 5 when it is introduced? Currently it just says the "cross section volume fraction of the biofilm", but that seems potentially ambiguous. It is valid to say that this is "fraction of the cross section occupied by the biofilm"?*

Changed

> *Bottom of page 5: can you state the physical interpretation of the assumption that M is bounded between 0 and 1. i.e. that growth is larger than detachment?*

There is a comment on that in the paper. It reads “In assuming that M ∈]0, 1] and eliminating cases where M > 1, we have not considered situations of systematic detachment ϕequ = 0 for any value of the concentration, since this is not a situation that we encountered experimentally.” This comes just after presenting the expression on the only non-trivial steady-state, as it becomes easier to explain the consequences of the initial choice at this point.

> *Currently the choice of detachment initially used in the model is a bit confusing. You say that you are going to assume a $(1-\phi)^{-1}$ model for simplicity (bottom of page 5), but then later you find that the $(1-\phi)^{-3/4}$ model is more accurate (page 16). Since the latter has already been confirmed in numerous other studies, why not start with that one from the beginning?*

We thank the reviewer for this important question, which highlights an area where our presentation could be clearer. We did not find that the $(1-\phi)^{-3/4}$ model is "more accurate." Rather, we deliberately chose the $(1-\phi)^{-1}$ scaling because it captures pressure-induced detachment, which we hypothesized would dominate in confined flows where biofilms clog a large portion of the channel. The $(1-\phi)^{-3/4}$ scaling, widely used in previous studies, describes shear stress at the biofilm/fluid interface and was developed primarily for reactor systems where pressure effects are negligible. Our analysis on page 16 validates this choice by demonstrating that pressure stress indeed exceeds shear stress when volume fraction is large, which corresponds to late Stage I and all of Stage II precisely where our model is applied. The excellent quantitative agreement between predicted and measured ϕ_{max} values across flow rates (Fig. 7f, Table 1) further supports the $(1-\phi)^{-1}$ scaling. We recognize that our initial presentation may have suggested the $(1-\phi)^{-1}$ choice was merely for "simplicity." We have revised this section to emphasize that this scaling was chosen specifically to capture pressure-driven detachment in confined geometries, with the physical justification provided by the stress analysis that follows. We have also clarified our ideas on page 16 to express clearly that $(1-\phi)^{-3/4}$ is never used. We could alternatively use a multi-modal detachment function combining both scalings, but the data do not require this additional complexity.

> *In general, the models you derived in this study could be better contrasted with that from previous works. e.g. can you compare your Eqn (4) with the steady-state solutions obtained by other previous studies? Is this consistent with previous works or different? (aside from framing the biofilm thickness in terms of ϕ)*

We are currently working on a paper dedicated to modeling biofilm development in confined flows, which will do a better job at comparing approaches.

> *Top of page 6 - you assume K* = 0.1 - Does this assume that cells grow at half the rate in 0.1X BHI as they do in 1X BHI? Has this been confirmed experimentally or is this just a guess?*

This was estimated rather than measured directly. Model predictions were a lot more sensitive to the Damköhler number, than to the value of K.

> *"radial" is used widely in this paper, but you are using a square geometry. Is "transverse" a better choice?*

Yes it clearly is. It’s been changed.

> *Fig 3. Are panels (a) and (b) showing different bioreps of the same condition? If so, please spell that out in the caption.*

There was an error here in the caption of fig a. This has been changed. The correspondence is between a and c, and these are exactly the same, not bioreps.

> *In multiple places it noted that the change in hydraulic resistance is correlated with the "change in biofilm colonization." Why not demonstrate this directly using a cross correlation analysis? How is the latter connected to the ϕ parameter? (e.g. is this $d(\phi)/dt$?)*

We thank the reviewer for this suggestion. To clarify: $\phi(t)$ represents the volume fraction of biofilm in the channel. We measure this in two independent ways: (1) $\phi(t)$ from hydraulic resistance (black line in Fig. 3) i.e. calculated from pressure measurements using $\phi = 1 - \sqrt{(R_0/R(t))}$, assuming uniform layer growth (see Methods section "Data analysis for the calculation of hydraulic resistance and volume fraction") and (2) $\phi(t)$ from fluorescence (green squares in Fig. 3) i.e. estimated from integrated GFP intensity or image segmentation of the glass/liquid interface. The reviewer is correct that we should quantify this relationship directly. We have now added correlation analysis between these two independent measurements of ϕ (new Supplementary Figure S21). The analysis shows strong positive correlation, with r-values ranged from 0.68 to 0.77 across all flow rates. This validates two key aspects of our approach: (1) the uniform layer assumption used to convert R(t) to $\phi(t)$ is reasonable, and (2) the pressure-based measurements accurately capture the dynamics visible in fluorescence imaging, including both growth phases and sloughing events. The strong agreement is particularly notable given that these measurements probe different aspects of the biofilm: hydraulic resistance is sensitive to the three-dimensional obstruction of flow, while fluorescence captures primarily the biofilm attached to the glass surface within our focal plane. Their correlation supports the model assumptions. We have revised the manuscript to clarify this relationship and present the correlation analysis.

> *Top of page 9 - a doubling time of 110 mins is reported in liquid culture - is this in shaken or static conditions? Can you provide some data on how this was calculated? (e.g. on a plate reader?) Do you think your measurements in the microfluidics could be affected by attachment/detachment of cells, rather than being solely driven by division. It is curious that your apparent growth rate varies by a factor of two across the different flow rates and there is not a monotonic dependency. Both attachment and detachment would depend on the flow rate (with some non-trivial dependencies).e.g. https://www.pnas.org/doi/10.1073/pnas.2307718120 https://doi.org/10.1016/j.bpj.2010.11.078*
>
> *Given that your doubling time in the microfluidics is sole based on changes in cell number (rather than directly tracking cell divisions) it seems possible your results here are measuring the combined effect of growth, attachment and detachment, rather than just growth.*

We agree with those comments regarding the doubling time measurement. We have added a description of how we performed the doubling time measurement in the Methods section.

> *Page 9 - you discuss the role of EPS here, but the effect of EPS is not demonstrated here and this is muddled with a discussion about the non-linearity of the putative dependency. Maybe this would be on a firmer footing if you save the discussion of EPS for the section on the Psl and Pel mutants?*

Changed.

> *Middle of page 9: Please define what "smooth detachment" means and contrast it with catastrophic sloughing. Also, please define what you mean by "flow, seeding, and erosion" detachment are and how these three things differ from one another.*

We have clearly defined each term in the revised version.

> *The results from wavelet scalograms seem to be underutilised and not well described. Can you clearly say what time series this analyses has been calculated on the caption? e.g. hydraulic resistance? Other than simply pointing out the "blue stripes", what can be gained from this analyses that could not be obtained with another method? It would be great if the basic features of this plot could more fully discussed (e.g. is the curved envelope at the bottom caused by edge effects?)*

We have improved the text, captions and method section following the reviewer's comment.

> *Fig. 5 a and b - please list the time at which each of these images were taken. Do these have the same dt between the two sets of images?*

Yes the dt is the same (30 minutes). It's been indicated in the caption.

> *Fig. 6: you have significant 2D variation in the biofilm width along the length of the channel. The relative contribution of pressure and shear based detachment will be different at different positions along the length. However, this variation is ignored in your model. Can you please comment on this in our manuscript and how it might affect the interpretation of your results? e.g. would the longitudinally averaged description yield the same result as one that takes the geometry into account (on average)?*

Our model indeed assumes longitudinally averaged properties. A more detailed spatially resolved model would be valuable for capturing heterogeneities and will be explored in future work.

> *Bottom of page 11: you say standard deviations are in the range of 10^{-3}. How does this jibe with the error bars on the middle flow rate in Fig. 7e?*

This extremely low standard deviation only applies to the maximum value of ϕ and is a completely different measurement from the whisker boxes presented in fig7e.

> *Fig. 7: You are calculating the "Fraction" here. Is this "ϕ"? If so, can you put that on the y-axis instead? You calculate the volume fraction two different ways e.g. with hydraulic resistance and with imaging. Is only one of these shown in (e)? Is the same powerlaw dependence shown in (f) conserved when the other measurement of the "fraction" is used? Can you include both in Fig. 7e?*

We have modified the axis and indicated ϕ.

(e) is calculated only from hydraulic resistance. This is the most precise measurement to evaluate ϕ quantitatively.

> *Related to the previous comment: Some of the estimates of ϕ_{max} in Table 1 are obtained by fitting the model to integrated fluorescence data (Fig. 2b), while others are estimated from measurements of the hydraulic resistance. The former yields non-unique sets of parameters. Can the biofilm fraction instead actually be estimated directly from fluorescent imaging by segmenting biofilm and directly calculating how much of the cross section is occupied by cells on average across the length? This seems like a more direct measure of this quantity. Given there are multiple ways of estimating the same parameter, it would be better consistency checking to make sure that different methods actually yield the same result.*

We have now added in Fig S21 a direct comparison of these two measurement methods. These are strongly correlated. Microscopy is more direct but only provides 2D pictures. Hydraulic resistance provides a 3D measurement, but relies on a model of biofilm

distribution. Both are imperfect, but correlate well. In particular, we see that the 2D measurement does capture sloughing.

> *You cite a large number of supplemental figures (e.g. Fig. S21 on page 12), but the figures in your SI only go up to 11.*

We have revised references to supplementary figures.

> *Bottom of page 11: Your data from liquid culture suggests that your psl mutant grows at half the rate of WT cells. Is that consistent with your microfluidic data (e.g. Fig. 8)? If not, might this be a sign that your growth rate analyses from the microfluidics might be affected by attachment/detachment? (see comment above) Psl cells should detach much more easily.*

The approach taken to measure doubling times in the microfluidic system does not rely on the macroscopic measurements presented in figure 8, but rather on the approach presented in fig 4. These measurements require specific imaging (different magnification and time stepping) and we did not perform such experiments for the mutants.

> *In analyses of sloughing, you fit the times between the jumps and the relative amplitude. Are these two random variables correlated with one another? Might that influence your results? Your methods say that "jumps were identified through through the selection of local maxima" of the derivative. Do you to say "minima" here? Did you keep all local maxima/minima or did you have a threshold?*

These are two random variables, not correlated with another. This is an assumption, and it would be interesting to analyze whether these are correlated. To perform this analysis, we believe that we would first need to acquire even more data and more replications to improve the statistical analysis.

Yes, it was minima (in the code we make everything positive, hence the confusion).

Yes, there is a threshold on the value of the jump itself. This value is extremely low and essentially filters out noise.

> *Fig. 9 - can you make it clearer in the caption what timeseries you are analysing here? I understand from the methods this that is the "volume fraction." The data/fits are difficult to see in Fig. 9 b and impossible to see in Fig. 9c because the green bars get in the way of the other two data sets. Can this visualisation be improved? It is not clear to me how good of a job the Gamma and log-normal fits are actually doing.*

We have clarified that histograms are calculated from all experiments/replicates.

We have slightly modified the graph to make it clearer. This comparison is intrinsically hard, partly because it compares discrete data with continuous PDFs.

> *Aside from noting the results from the stochastic sloughing model are 'strikingly similar to experimental data', which seems to be based on a qualitative analysis of the lines in Fig. 7 d, e, and f. However, experimental data is not plotted in the same graph nor is the experimental data that we should be comparing this to cited in the text/caption.*

We have added a note in the caption to indicate which figure it can be compared to.

https://doi.org/10.7554/eLife.98292.2.sa0